CPHASE analysis in the eigenmode approach in presence of ZZ crosstalk

Master Thesis Applied Physics

Olivia Hefti

Student number: 4916506

Project duration: September 1, 2019 – April 30, 2020

Thesis Supervisors:	Prof. Barbara Terhal,	TU Delft, Qutech
	Post-doctoral Alessandro Ciani,	TU Delft, Qutech

Thesis committee:	Prof. Barbara Terhal,	TU Delft, Qutech
	Prof. Leonardo DiCarlo,	TU Delft, Qutech
	Prof. Michael Wimmer,	TU Delft, Qutech

TU Delft Delft University of Technology

QUTech

Contents

Acknowledgements

I would like to thank Professor Barbara Terhal and my daily supervisor, Alessandro Ciani, for their mentoring and for being inspiring researchers. Furthermore, they gave me the opportunity and some keys to explore the fascinating topic of superconducting qubits. Special thanks goes to Alessandro Ciani for the precious guidance, disponibility and consideration about my work. Finally I would like to thank my parents, my sister, Hélène, and Bastien for the invaluable support and encouragement during my studies, for visiting me and for being a source of joy in my life.

Chapter 1

Introduction

1.1 Research background

Quantum computers open the door to quantum simulation with potential applications in the field of condensed-matter physics, high-energy physics, atomic physics, quantum chemistry and cosmology [1]. Moreover, some problems like factoring very large numbers into their primes using Shor's algorithm and searching large, unstructured data sets with Grover's search algorithm, can be solved in a reasonable amount of time using a quantum computer contrary to a conventional, classical computer [2]. This large panel of applications and the potential impacts on society explain why building a quantum computer is a major focus for the scientific community. Then comes the question of how can a quantum computer be implemented. First and foremost, quantum information is encoded in qubit states. A qubit is a mathematical object whose general state is a linear combinations of $|0\rangle$ and $|1\rangle$, i.e $|\psi\rangle = \alpha|0\rangle + \beta|1\rangle$ with the complex numbers α and β satisfying $|\alpha|^2 + |\beta|^2 = 1$ [2]. The following five DiVincenzo criteria are necessary conditions for constructing a quantum computer [3] :

1. A scalable physical system with well characterized qubit
2. Long relevant decoherence times
3. A "universal" set of quantum gates [1]
4. The ability to initialize the state of the qubits to a simple fiducial state

[1] An arbitrary quantum computation on any number of qubits can be generated by a finite set of gates that is said to be universal for quantum computation [2].

5. A qubit-specific measurement capability

The way the first three criteria are satisfied in the context of circuit quantum electrodynamics (circuit QED) [4], which is a possible hardware for a quantum computer, is of interest for this master thesis. More precisely, we focus on the implementation of surface code fabric developed at Qutech whose purpose is given at point 2 [5]. :

1. Qubits are realized by flux-tunable transmons interconnected by bus resonators [6]. They are presented in details in Sec. 2.1 and are laid out on a two-dimensional square lattice to form the surface code [7]. The latter consists of data-carrying qubits and X (Z) type ancilla qubits. The numbers in Surface-7, Surface-17 and Surface-49 indicate the amount of qubits on the chip, as shown in Fig. 1.1.1 for the specific example of Surface-17 [5].

2. The surface code protects data qubits from decoherence caused by the interaction between the qubit and the noisy environment. As the surface code itself is not the main focus of this work, we only mention its purpose, give a general idea on how it works and recommend the reader to turn to Refs. [8] and [9] for more details. In order to detect whether errors occurred on the data qubits and to correct them afterwards, ancilla qubits are used to perform X type and Z type quantum parity checks of their nearest-neighbor data qubits [5]. In other words, each ancilla qubit interacts with its four neighouring data qubits in a specific order and the states of the ancillas are then measured. From the output formed by the set of parity checks on the whole fabric, errors on data qubits can be extracted and then (hopefully) corrected.

3. A universal set of quantum gates for computation with unencoded qubits, i.e. the state of one qubit is encoded in a single physical qubit, is formed by the unencoded CPHASE gate and with some single qubit rotation gates[2]. However, in the context of the Surface code, the state of a qubit is encoded redundantly in a so-called logical qubit formed by a higher number of qubits [8]. Then, an encoded universal set of gates, i.e. gates which are effective on the logical qubit, is required

[2]Single qubit and CNOT gates are universal [2]. CNOT and CPHASE can be built from each other via the relation $\mathrm{CNOT} = (\mathrm{I} \otimes \mathrm{H})\mathrm{CPHASE}(\mathrm{I} \otimes \mathrm{H})$, where the hadamard gate is $\mathrm{H} = \frac{1}{\sqrt{2}} \begin{pmatrix} 1 & 1 \\ 1 & -1 \end{pmatrix}$, see Fig. 8 in [10]. Hence CPHASE gate together with the set of single-qubit rotations also form a universal set of quantum gates.

for computation. This thesis discusses unencoded CPHASE gates. In the Surface code, they are used in order to do error correction.

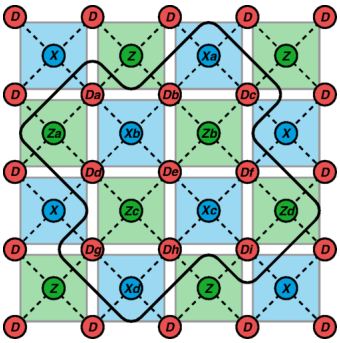

Figure 1.1.1: Layout of the so-called Surface-17 code fabric (enclosed in the black line) where data qubits are represented by red circles with D labels, while blue (green) circles with X (Z) labels represent ancillas performing X type (Z type) quantum parity checks of their nearest-neighbor data qubits [5]. (The figure is taken from [5], page 2.)

1.2 Problem description

In superconducting qubit architectures achieving high fidelity two-qubit gates is challenging. Considering the CPHASE two-qubit gate, the interaction that allows its implementation is the so-called cross-Kerr interaction, which is characterized by the cross-Kerr coefficient defined as

$$\chi = E_{11} - E_{10} - E_{01}. \tag{1.1}$$

Here E_{11}, E_{10} and E_{01} are the instantaneous eigenenergies associated with the states $|11\rangle$, $|01\rangle$ and $|10\rangle$ and the lowest energy level E_{00}, associated with the state $|00\rangle$, is set to zero[3]. When we want to perform a CPHASE gate, the system is generally taken to a point where the cross-Kerr coefficient χ between the two qubits involved in the CPHASE gate is high, leading to a fast gate [11]. On the other hand, the ability to reach high cross-Kerr at the interaction point generally entails also non-negligible residual cross-Kerr between neighbouring qubits, when they are not supposed to interact. This unwanted residual cross-Kerr interaction is referred to as ZZ crosstalk [12]. The latter causes a shift of the frequency of a qubit depending on the state of each of its neighbours. The value of the shift is also given by the cross-Kerr coefficient in Eq. (1.1). The

[3]We emphasize that the states $|00\rangle$, $|01\rangle$, $|10\rangle$ and $|11\rangle$ are the instantaneous eigenstates and not the computational ones. These bases are not equivalent when an external flux is applied to the circuit.

effect of crosstalk on the fidelity of the CPHASE gate, as yet not well known, is currently being studied [13]. Additionally, the method that we use in order to simulate the CPHASE gate in this thesis, the eigenmode approach, involves different approximations that can be applied. To the best of our knowledge, the problem of determining which approximation can be used to simulate the CPHASE gate has never been studied.

1.3 Scope of this work

In this thesis, a method referred to as the 'eigenmode approach', is introduced in Sec. 2.2. Given a certain circuit composed of capacitances, inductances and Josephson junctions, it identifies the eigenmodes of the linear part of the circuit as qubit-like or resonator-like modes and adds the non-linearity of the Josephson junctions as a coupling between the modes. Approximations can be applied to the potential of the Josephson junctions. Firstly, a Taylor expansion up to a certain order is performed on it. Then, the rotating-wave approximation (RWA) or what we will call the full rotating wave approximation (full RWA) can be applied on top of that to the non-linearity. These approximations are presented in Subsec. 2.2.2. This method was initially presented in Ref. [14] and a Quantum Circuit Analyzer Tool, called QuCAT, based on this method is presented in [15]. ***As the ultimate goal is to provide an accurate CPHASE analysis in presence of ZZ crosstalk***, the first step is to validate the accuracy of the different approximations. The (in-)validation of the approximations is carried out in Subsec. 3.1.3 using two capacitively coupled transmon qubits. This circuit is chosen because it can be easily numerically diagonalized in the Cooper-pair basis. As a result, a comparison between the exact solution in the Cooper-pair basis and the results obtained with the different approximations, provides a way to check their validity. The energy levels and the avoided crossing positions (point where a CPHASE gate can be implemented [11]), are compared between each approximation and the exact solution in Subsec. 3.1.3. Once the approximation with desired accuracy is determined, it is used for CPHASE simulation. In order to tackle the problem described in Sec. 1.2, this work provides a CPHASE analysis without crosstalk and then with crosstalk from a neighbouring qubit. Firstly, in Subsec. 3.2.1 CPHASE simulations are performed using a system of two capacitively coupled transmons. Then, in Subsec. 4.2 a third transmon, the spectator, is added in order to perform CPHASE simulations in presence of crosstalk using a system of three capacitively coupled transmons. We analyze how crosstalk from the spectator impacts the CPHASE fidelity. We point out out that no noise is implemented as we aim to verify

whether simulations using the eigenmode approach can be used to accurately model the CPHASE gate. Another reason we do not implement random noise is that we need to compare simulations in Subsec. 4.2, in order to determine the effect of the crosstalk on the gate itself.

1.4 Research questions

This thesis addresses mainly the following questions. Firstly, we would like to ***determine if the eigenmode approach can be used to accurately model the CPHASE gate. And which approximation can be used for describing the two-qubit interaction in the CPHASE gate simulation.*** Secondly, we consider the question of *whether other approximations could be used to accurately describe crosstalk* effects from neighbouring qubits on Q_H and Q_M, i.e. the two qubits involved in the CPHASE gate. And if this is the case, which approximation could be used for that purpose.

The choice of the two capacitively coupled transmons for CPHASE simulation raises another question because in superconducting qubit architectures, the coupling is often mediated via resonators. Indeed, one could ask *whether the simulations, when using a resonator would remain the same or, on the contrary, invalidate the conclusions drawn from CPHASE simulations with a capacitive coupler.* As the behaviour of a system is characterized by its Hamiltonian, we are seeking to prove that the energy levels of interest, obtained on one side with the resonator and in the other side removing the resonator, are in good agreement. This analysis is carried out in Sec. 3.3. Finally, the questions ***"What are the CPHASE fidelity when we apply diabatic pulses and use the method of the eigenmode approach ?"*** and ***"How much does crosstalk affect the fidelity of the CPHASE gate?"*** are addressed in Subsec. 3.2.1 and Sec. 4.2, respectively.

1.5 Plan

This thesis is organized as follows :

Chapter 2 introduces some **theory** underlying circuit QED : its building blocks and the eigenmode approach, to mathematically analyze its circuits. Finally, the CPHASE gate is presented.

Chapter 3 gathers the eigenmode analysis and CPHASE simulation without crosstalk of a system composed of **two** capacitively coupled **transmon qubits**.

Chapter 4 is dedicated to the eigenmode analysis and CPHASE simulation with crosstalk of a system involving **three** capacitively coupled **transmons qubits**.

In **Appendix A**, a clarification about what terms drives effectively the CPHASE gate in the eigenmode approach is presented. Then, a proof on which the derivations of the eigenmode method is based is given in **Appendix B**. Finally, in **Appendix C**, a connection between a N-port network and its equivalent Foster circuit is drawn.

Chapter 2

Theory

This chapter starts with an introduction of the circuit QED building blocks in Subsec. 2.1. Then, the eigenmode approach is described in Subsec. 2.2. Finally, the theory underlying the CPHASE gate is presented in Subsec. 2.3.

2.1 Circuit building blocks

In this section, we introduce the building blocks of circuit QED quantum processors. These circuits generally consist of capacitances, inductances, Josephson junctions and transmission line resonators [4]. From these elements, different types of Josephson junction based qubit circuits can be build up such as the Cooper-pair box, the transmon qubit, the flux qubit, the phase qubit and the fluxonium (see [16] and [17]). In this thesis we focus on the transmon qubit, which is a Cooper-pair box shunted by a large capacitance [16], because currently most of superconducting chips are based on transmons [18]. Both are extensively presented in Subsec. 2.1.2. The resonators are superconducting coplanar waveguides and the ones we consider are used either to read-out the qubit state or to mediate the interaction between them, in order to perform two-qubit gates. In effect, the state of a qubit capacitively coupled to a readout resonator can be inferred by measuring the state-dependent shift of the resonance peak in the transmission spectrum of the latter [4]. This procedure is called dispersive readout. Instead, bus resonators are capacitively coupled to two transmons and mediate the coupling between them. Although transmission line resonators have many resonant modes, they are generally modelled by single quantum harmonic oscillators, focusing on the fundamental mode [19].

Unlike resonators, transmons are anharmonic oscillators. The anharmonicity is required in quantum computation in order to isolate the computational basis spanned by the two lowest states $|0\rangle$ and $|1\rangle$ from the higher energy levels. In fact, a harmonic oscillator cannot be used as a two-level system because a linear drive at the resonant frequency would induce transition with higher energy levels and populate them. The element that brings anharmonicity to the transmon spectrum is the Josephson junction (JJ), which can be seen as a non-linear inductor. Josephson junctions are superconducting circuit elements formed by two pieces of superconductors separated by a thin insulating barrier. Cooper-pairs can tunnel through the barrier resulting in a flow of superconducting current across the junction [16]. The quantum treatment of harmonic and anharmonic oscillators is presented in Subsecs. 2.1.1 and 2.1.2, respectively.

2.1.1 Quantum LC oscillator

An LC oscillator, whose circuit is shown in Fig. 2.1.1, is formed by a capacitance and an inductor, denoted by C and L respectively, connected in parallel and across which we define the flux difference

$$\Phi(t) = \int_{-\infty}^{t} dt' V(t'), \tag{2.1}$$

where $V(t)$ is the voltage across C and L.

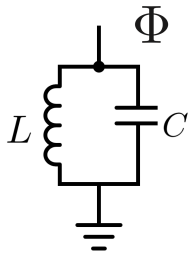

Figure 2.1.1: LC oscillator circuit.

The resonant frequency of the oscillator is $\omega_{LC} = 1/\sqrt{LC}$ and its Lagrangian is given by the capacitive energy ("kinetic energy") minus the inductive energy ("potential energy"):

$$\mathcal{L}(\Phi, \dot{\Phi}) = \frac{C\dot{\Phi}^2}{2} - \frac{\Phi^2}{2L}. \tag{2.2}$$

The charge Q is the canonical conjugate variable of Φ and is obtained with the rela-

tion :

$$Q = \frac{\partial \mathcal{L}}{\partial \dot{\Phi}}. \tag{2.3}$$

The Legendre transform of the Lagrangian in Eq. (2.2) with respect to Φ leads to the Hamiltonian [19] :

$$H(\Phi, Q) = \dot{\Phi}Q - \mathcal{L}(\Phi, \dot{\Phi}) = \frac{Q^2}{2C} + \frac{\Phi^2}{2L}. \tag{2.4}$$

In order to obtain a quantum description of the problem, canonical quantization is performed by promoting Φ and Q to operators (denoted by hat) and imposing the commutation relation $[\hat{\Phi}, \hat{Q}] = i\hbar$. This commutation relation implies that the spectrum of the Hamiltonian is discrete, with each energy levels separated by the constant quanta given by : $\Delta E = E_{n+1} - E_n = \hbar\omega_{LC}$ with $n \in \mathbb{N}_0$. Thus, the Hamiltonian in Eq. (2.4) describes an harmonic oscillator.

2.1.2 Anharmonic oscillator: the Cooper-pair Box and the Transmon

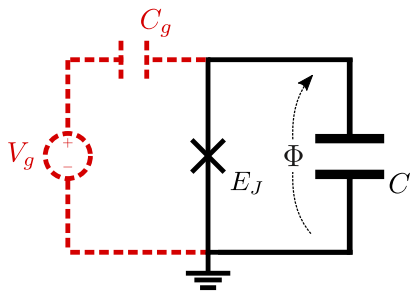

Figure 2.1.2: Circuit of the Cooper-pair box. The red dashed part of the circuit is used as a model for charge noise. The superconducting phase, φ, associated with the flux Φ is given by $\varphi = \frac{2\pi\Phi}{\Phi_0}$, where $\Phi_0 = \frac{h}{2e}$ is the superconducting flux quantum.

A Cooper-pair box (CPB) is a circuit formed by a Josephson junction and an additional capacitance, as depicted in Fig. 2.1.2. It is characterized by the following Hamiltonian:

$$\hat{H} = 4E_c(\hat{n} - n_g)^2 - E_J \cos(\hat{\varphi}), \quad [\hat{\varphi}, \hat{n}] = i \tag{2.5}$$

with charging energy $E_c = e^2/(2C_\Sigma)$, $C_\Sigma = C + C_g$, and $n_g = C_g V_g/(2e)$ the reduced gate charge, i.e., the parameter that characterizes charge noise. E_c is the energy cost of adding or removing a Cooper-pair on the capacitor plate. The Josephson energy E_J is the energy involved when a Cooper-pair tunnels through the insulating barrier in order to reach the island at the other side [20]. Here $\hat{n}$ and $\hat{\varphi}$, which are canonical

conjugate variables as they satisfy the commutation relation in Eq. 2.5, are respectively the operator for the number of Cooper-pairs transferred between the islands and the phase difference across the superconducting electrodes of the Josephson junction. $\hat{n}$ is related to the charge operator by $\hat{Q} = 2e\hat{n}$.

Diagonalization in the Cooper-pair basis

We introduce the Cooper-pair basis formed by the set $\{|n\rangle\}$ where the integer n corresponds to the number of pairs in state $|n\rangle$. $\hat{n}$ and $\hat{\varphi}$ satisfy the relation $[\hat{n}, e^{\pm i\hat{\varphi}}] = \pm e^{\pm i\hat{\varphi}}$, see [21], which implies:

$$e^{i\hat{\varphi}} |n\rangle = |n+1\rangle . \tag{2.6}$$

We express the potential in Eq. (2.5),

$$\hat{V} = -E_J \cos(\hat{\varphi}) = -E_J \frac{e^{i\hat{\varphi}} + e^{-i\hat{\varphi}}}{2}, \tag{2.7}$$

in the Cooper-pair basis using Eq. (2.6) as

$$\hat{V} = \sum_{n=-\infty}^{\infty} -\frac{E_J}{2} \big(|n\rangle \langle n+1| + |n+1\rangle \langle n| \big). \tag{2.8}$$

Notice that the operator $\hat{n}$ has a discrete spectrum given by $\mathbb{Z}$, the set of integers. This implies that its conjugate variable $\hat{\varphi}$ is a compact variable whose eigenvalues are defined in $\varphi \in (-\pi, \pi]$, i.e. the states $|\varphi - \pi\rangle$ and $|\varphi + \pi\rangle$ are identical. Using the discrete relation of completeness $I = \sum_{m=-\infty}^{\infty} |m\rangle \langle m|$ and the fact that $\langle m|\varphi\rangle = e^{-im\varphi}$, we obtain the relation $|\varphi\rangle = \sum_{m=-\infty}^{\infty} e^{-im\varphi} |m\rangle$ from which we can check that $|\varphi - \pi\rangle = |\varphi + \pi\rangle$. The eigenvalue problem associated with Eq. (2.5) has an analytical solution in terms of Mathieu functions [22]. However, Eq. (2.5) can also be diagonalized numerically in the Cooper-pair basis by cutting the Hilbert space to a sufficient number of charge states, taken to be symmetric around zero ($n_g \in [0, 1)$), and by checking that the eigenenergies we are interested in do not change if we include more charge states in the diagonalization. We use this approach since it is easy to code also when we consider more capacitively coupled Cooper-pair boxes as in [23]. Explicitly, in the Cooper-pair basis we are making the following approximations :

$$(\hat{n} - n_g)^2 = \sum_{n=-\infty}^{\infty} (n - n_g)^2 |n\rangle \langle n| \approx \sum_{n=-m}^{m} (n - n_g)^2 |n\rangle \langle n| \tag{2.9}$$

and

$$\begin{aligned}\cos(\hat{\varphi}) = \frac{1}{2}(e^{i\hat{\varphi}} + e^{-i\hat{\varphi}}) &= \sum_{n=-\infty}^{\infty} \frac{1}{2}(|n\rangle\langle n+1| + |n+1\rangle\langle n|) \\ &\approx \sum_{n=-m}^{m-1} \frac{1}{2}(|n\rangle\langle n+1| + |n+1\rangle\langle n|).\end{aligned} \tag{2.10}$$

We perform these approximations on the Hamiltonian in Eq. (2.5) and we obtain a finite matrix to be diagonalized numerically. We refer to this method as **exact** diagonalization.

Transmon regime

The transmon qubit is essentially a CPB operated in the regime of $E_J/E_c \in [40, 200]$ [17]. In many designs, transmons are flux tunable so the single Josepshon junction shown in Fig. 2.1.2 is replaced by a SQUID loop. In other words, a flux-tunable transmon consists of two superconducting islands coupled through two Josephson junctions [6]. The use of the SQUID loop is discussed in Subsec. 2.1.3.

In the so-called transmon regime, $E_J/E_c \gg 1$, the phase variable remains close to the minima of the cosine potential. Indeed, the low-energy wavefunctions are confined near $\varphi = 0$, the only minimum for $\varphi \in (-\pi, \pi]$ [20]. The confinement of the wavefunctions in phase representation allows us to take the Taylor expansion of the cosine [24]:

$$\hat{V} \approx -E_J\big(1 - \frac{1}{2!}\hat{\varphi}^2 + \frac{1}{4!}\hat{\varphi}^4 - \frac{1}{6!}\hat{\varphi}^6 + \dots\big). \tag{2.11}$$

This approximation however is only valid if we are interested in the low lying energy levels of the system, it completely neglects the periodic boundary conditions and consequently it cannot see the dependency of the spectrum on the parameter n_g. This is because we are substituting solutions normalized in $\varphi \in (-\pi, \pi]$ with solutions normalized in $\mathbb{R}$. As a consequence the charge operator has no longer a discrete spectrum in this approximation [24]. We now derive the linear and non-linear Hamiltonian of a transmon in terms of its creation and annihilation operators. We expand the cosine in Eq. (2.5) up to 4th order and neglect n_g, which is valid in the regime $E_J/E_c \gg 1$ [19] and [24], and we get

$$\hat{H} \approx \hat{H}^{(4)} = 4E_c\hat{n}^2 - E_J\big(1 - \frac{1}{2!}\hat{\varphi}^2 + \frac{1}{4!}\hat{\varphi}^4\big). \tag{2.12}$$

In general if we perform a Taylor expansion up to order k we will denote the associated Hamiltonian $\hat{H}^{(k)}$. The strategy now is to diagonalize the quadratic part by introducing

the annihilation and creation operators, $\hat{a}$ and $\hat{a}^\dagger$, as :

$$\begin{cases} \hat{\varphi} = \left(\frac{2E_c}{E_J}\right)^{\frac{1}{4}} (\hat{a}^\dagger + \hat{a}), \\ \hat{n} = \frac{i}{2}\left(\frac{E_J}{2E_c}\right)^{\frac{1}{4}} (\hat{a}^\dagger - \hat{a}). \end{cases} \tag{2.13}$$

They satisfy the commutation rule $\left[\hat{a}, \hat{a}^\dagger\right] = 1$. The transmon Hamiltonian in Eq. (2.12) omitting the constant term, is split into a linear, $\hat{H}_{\text{lin}}$, and a non-linear, $\hat{H}_{\text{nonlin}}$, part as follows :

$$\begin{cases} \hat{H}_{\text{lin}} = 4E_c\hat{n}^2 + \frac{1}{2}E_J\hat{\varphi}^2, \\ \hat{H}_{\text{nonlin}} = -\frac{1}{24}E_J\hat{\varphi}^4. \end{cases} \tag{2.14}$$

Substituting the expressions in Eq. 2.13, this becomes :

$$\begin{cases} \hat{H}_{\text{lin}} = -4E_c\frac{1}{4}\left(\frac{E_J}{2E_c}\right)^{\frac{1}{2}} (\hat{a}^\dagger - \hat{a})^2 + \frac{1}{2}E_J\left(\frac{2E_c}{E_J}\right)^{\frac{1}{2}} (\hat{a}^\dagger + \hat{a})^2, \\ \hat{H}_{\text{nonlin}} = -\frac{1}{24}E_J\left(\frac{2E_c}{E_J}\right) (\hat{a}^\dagger + \hat{a})^4. \end{cases} \tag{2.15}$$

A quantum harmonic oscillator with frequency $\omega_t = \sqrt{8E_cE_J}/\hbar$ is recovered for the linear part of the Hamiltonian :

$$\hat{H}_{\text{lin}} = \hbar\omega_t\left(\hat{a}^\dagger\hat{a} + \frac{1}{2}\right), \tag{2.16}$$

while the full expression for the 4th order Hamiltonian is given by:

$$\hat{H}^{(4)} = \hbar\omega_t\left(\hat{a}^\dagger\hat{a} + \frac{1}{2}\right) - \frac{1}{24}E_J\left(\frac{2E_c}{E_J}\right)(\hat{a}^\dagger + \hat{a})^4. \tag{2.17}$$

Eq. (2.17) can be diagonalized for instance in the Fock basis, by considering a finite number of Fock states, to provide an approximation of the eigenenergies of the transmon Hamiltonian. Notice that since the 4th order potential goes unphysically to -∞ for $\hat{\varphi} \to \pm\infty$, we have to be careful, since including too many Fock states in the diagonalization might give unphysical solutions that are an artifact of the approximation.

2.1.3 SQUID

A SQUID is a device where two Josephson junctions of energy E_{J1} and E_{J2}, respectively, form a loop. We will show that the effective Josephson energy of a SQUID, and thus its resonant frequency, can be tuned by changing the external flux, Φ^{ext}, through the loop. The circuit of a flux-tunable transmon, depicted in Fig. 2.1.3, is obtained by shunting a

SQUID with a capacitance. It realizes a flux-tunable qubit platform. We use the relation between the flux and the phase

$$\hat{\varphi} = \frac{2\pi\hat{\Phi}}{\Phi_0}, \tag{2.18}$$

where Φ_0 is the magnetic flux quantum. Then, the potential of a SQUID reads:

$$\hat{V}_{\text{SQUID}} = -E_{J1}\cos(\hat{\varphi}_1) - E_{J2}\cos(\hat{\varphi}_2). \tag{2.19}$$

We associate to the external flux applied through the loop, Φ^{ext}, an external phase given by:

$$\varphi^{\text{ext}} = \frac{2\pi\Phi^{\text{ext}}}{\Phi_0}. \tag{2.20}$$

Due to flux quantization within the closed superconducting loop [16], the phase difference between the two junctions is fixed by the condition

$$\hat{\varphi}_1 - \hat{\varphi}_2 = 2\pi n + \varphi^{\text{ext}}. \tag{2.21}$$

Here n is an integer. We assume the symmetry of the two Josephson junctions, i.e. $E_{J1} = E_{J2} = E_J$, and we use a trigonometric relation. Then we get:

$$\hat{V}_{\text{SQUID}} = -2E_J\cos(\frac{\hat{\varphi}_1 - \hat{\varphi}_2}{2})\cos(\frac{\hat{\varphi}_1 + \hat{\varphi}_1}{2}). \tag{2.22}$$

We introduce

$$\hat{\varphi} = \frac{\hat{\varphi}_1 + \hat{\varphi}_2}{2} \tag{2.23}$$

and we use Eq. (2.21) to obtain the potential

$$\hat{V}_{\text{SQUID}} = -2E_J\cos(\frac{\varphi^{\text{ext}}}{2})\cos(\hat{\varphi}). \tag{2.24}$$

We define $E_J(\Phi^{\text{ext}}) = 2E_J\cos\left(\pi\Phi^{\text{ext}}/\Phi_0\right)$ as the effective Josephson energy of the circuit when an external flux pulse is applied. An effective Josephson energy can also be derived in the case of non-symmetric Josephson junctions, see Eq. (2.18) in [6].

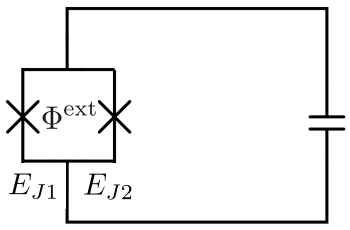

Figure 2.1.3: Transmon circuit with a SQUID loop. The resonant frequency of the transmon can be tuned by changing the external flux Φ^{ext} applied through the loop.

2.2 Eigenmode approach

The method we denote by the eigenmode approach was presented for the first time in Ref. [14] and recently a Quantum Circuit Analyzer Tool in Python implementing the method has been developed [15]. Before providing a detailed derivation of the eigenmode approach in the subsequent sections, let us give its main steps.

1. Superconducting circuits consist generally of connections of capacitances, inductances and Josephson junctions. We will focus on circuits involving transmons capacitively coupled to bus resonators. An example for the specific case of the Surface-7 layout is depicted in Fig. 2.2.1a and schematically in Fig. 2.2.1b. The associated Lagrangian is obtained by performing circuit quantization. By expansion of the cosine potential, the Josephson junctions of the transmons are split into a linear (linear inductor) and a non-linear (spider) part as represented on Fig. 2.2.2.

2. The non-linearities of the Josephson junctions are taken out of the linear network, characterized by its impedance matrix $\boldsymbol{Z}(s)$ [25]. The basics about N-port network are presented in Appendix C.

3. In a first step, the eigenmode approach consists in focusing on the linear network in order to obtain its normal modes and the associated frequencies. This is done by diagonalization at the Lagrangian level as presented in Sec. 2.2.1. We emphasize that only the linear Lagrangian is treated in this step. The eigenmodes obtained are identified as either qubit-like or resonator-like modes.

4. In a second step, the non-linearity is expressed in terms of the eigenmodes. Then, applying the second quantization, the Lagrangian and the Hamiltonian are expressed in terms of the annihilation and creation operators associated with the normal modes. On top of the non-linear Hamiltonian, different approximation can be taken. These are introduced in Sec. 2.2.2.

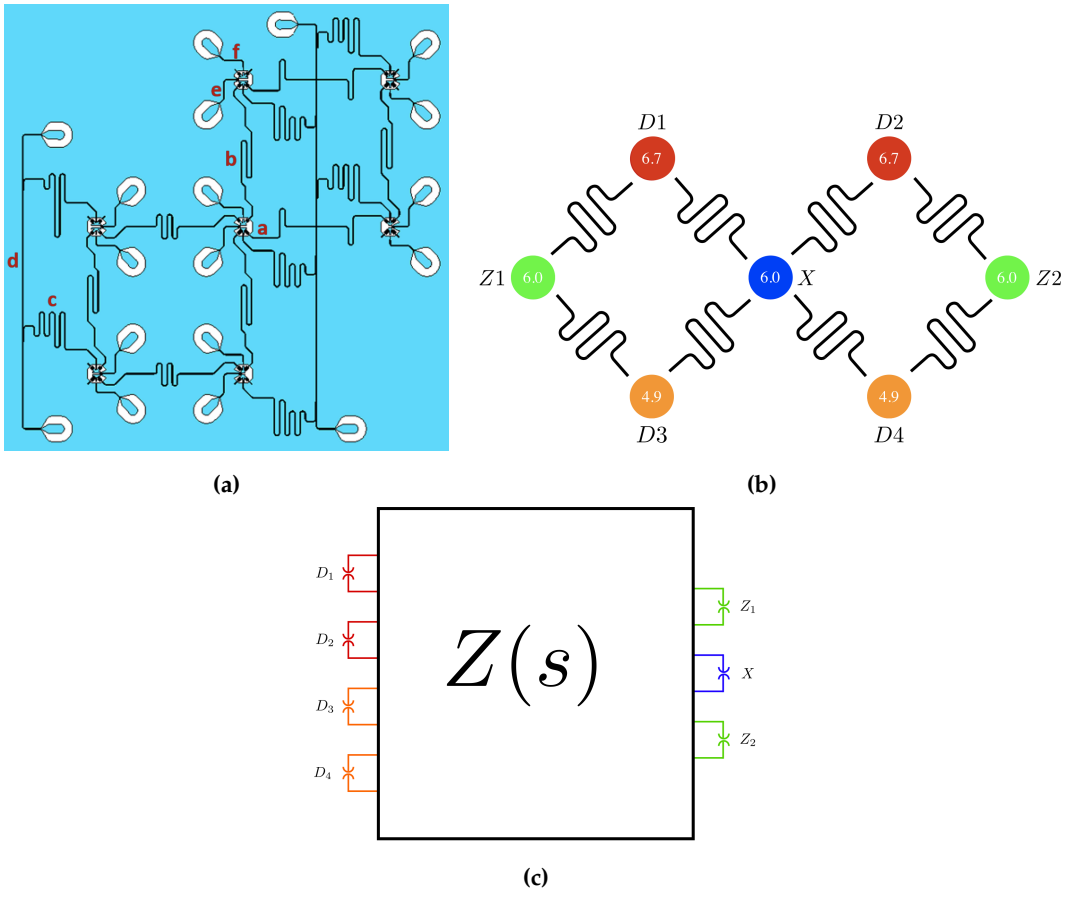

Figure 2.2.1: Surface-7 layout developed at Qutech in the DiCarlo lab. It is used in order to implement Quantum Error Correction. Fig. **a)** shows the Surface-7 layout as drawn in the context of FEM simulation in [26]. Here a is one of the qubits, b and c are one of the bus and readout resonators, respectively. d is one of the feedlines that is part of the qubit measurement circuitry and e is one of the flux drive line used to apply an external flux in the loop of a SQUID. Finally, f is one of the microwave drive line. (The figure is taken from [26], page 3). Fig. **b)** represents schematically Surface-7. It shows the bus resonator connecting the coloured transmons, whose associated target frequencies are indicated. The names D_i, Z_i and X refers to the role the qubits play in Quantum Error Correction protocol : data-carrying vs Z (X) type ancilla qubits. Fig. **c)** illustrates how the Surface-7 is seen from a network point of view, in which the linear network, within the black box, is fully characterized by the impedance matrix, $\boldsymbol{Z}(s)$, while the coloured spiders stand for the non-linearities of the Josephson junction associated with the transmons in Fig. **b)**.

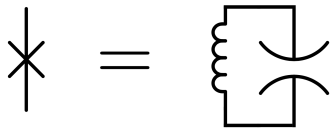

Figure 2.2.2: By expansion of its cosine potential, a Josephson junction, symbolized on the left, can be split into a linear inductor in parallel with a "spider" symbol standing for the non-linearity as drawn on the right. This representation allows excluding the non-linearity of the Josephson junctions from the linear part of network.

2.2.1 Diagonalizing classical linear systems at the Lagrangian level

The following derivation is adapted from an unpublished work by Ciani [27]. We consider a N-port linear network consisting only of capacitances, inductances, mutual inductances and ideal transformer. We use the method of nodes, described in the subsections 2.1.6 to 2.1.8 in Ref. [16], in order to determine the degrees of freedom of the circuit. We gather the resulting independent flux variables and define the vector

$$\widetilde{\mathbf{\Phi}}_{\mathbf{PI}} = \begin{pmatrix} \Phi_{P1} \\ \vdots \\ \Phi_{PN} \\ \Phi_{I1} \\ \vdots \\ \Phi_{IN_I} \end{pmatrix}. \tag{2.25}$$

Here Φ_{Pn} with $n = 1, \ldots, N$, denote the fluxes across the ports of the network (where the spiders of the Josephson junctions are attached). They are formally defined as

$$\Phi_{Pn}(t) = \int_{-\infty}^{t} dt' V_{Pn}(t'), \tag{2.26}$$

where $V_{Pn}(t)$ is the voltage across the nth port. The fluxes Φ_{Ik} with $k = 1, \ldots, N_I$ in Eq. (2.25) denote generically internal flux degrees of freedom. In the circuits analyzed in this work, the latter are associated with the bus resonator modes. From now on, we denote the total number of degrees of freedom by $M = N + N_I$. We introduce the capacitance matrix $\boldsymbol{C}$ and the inductance matrix $\boldsymbol{L}$ which are, in general, positive semidefinite, symmetric matrices. In essence, they are positive semidefinite because the capacitive energies and the inductive energies are sums of non-negative quantities [28]. For simplicity, we will assume from now on that $\boldsymbol{C}$ and $\boldsymbol{L}$ are positive definite matrices

and they are thus both invertible. The Lagrangian of the N-port linear networks that we consider can always be expressed as

$$\mathcal{L}(\widetilde{\mathbf{\Phi}}_{\mathbf{PI}}, \dot{\widetilde{\mathbf{\Phi}}}_{\mathbf{PI}}) = \frac{1}{2}\dot{\widetilde{\mathbf{\Phi}}}_{\mathbf{PI}}^{T}\boldsymbol{C}\dot{\widetilde{\mathbf{\Phi}}}_{\mathbf{PI}} - \frac{1}{2}\widetilde{\mathbf{\Phi}}_{\mathbf{PI}}^{T}\boldsymbol{L}^{-\mathbf{1}}\widetilde{\mathbf{\Phi}}_{\mathbf{PI}}. \tag{2.27}$$

We take the Euler-Lagrange equations associated with each independent flux variables and obtain

$$\frac{d}{dt}\frac{\partial \mathcal{L}}{\partial \dot{\widetilde{\Phi}}_{\mathrm{PI}_k}} - \frac{\partial \mathcal{L}}{\partial \widetilde{\Phi}_{\mathrm{PI}_k}} = 0, \quad \text{for } k = 1, 2, .., M. \tag{2.28}$$

This system of equations can be compactly rewritten as

$$\boldsymbol{C}\frac{d^2\widetilde{\mathbf{\Phi}}_{\mathbf{PI}}}{dt^2} = -\boldsymbol{L}^{-\mathbf{1}}\widetilde{\mathbf{\Phi}}_{\mathbf{PI}}. \tag{2.29}$$

As $\boldsymbol{C}$ is symmetric and positive definite, it is invertible and it is thus possible to multiply on the left by $\boldsymbol{C}^{-\mathbf{1}}$:

$$\frac{d^2\widetilde{\mathbf{\Phi}}_{\mathbf{PI}}}{dt^2} = -\boldsymbol{C}^{-\mathbf{1}}\boldsymbol{L}^{-\mathbf{1}}\widetilde{\mathbf{\Phi}}_{\mathbf{PI}}. \tag{2.30}$$

The solution of the problem thus coincides with the diagonalization of the matrix $\boldsymbol{C}^{-\mathbf{1}}\boldsymbol{L}^{-\mathbf{1}}$. As we assumed that $\boldsymbol{C}^{-\mathbf{1}}$ and $\boldsymbol{L}^{-\mathbf{1}}$ are both separately invertible, this reduces to diagonalizing the matrix $(\boldsymbol{LC})^{-\mathbf{1}}$, leading to:

$$\frac{d^2\widetilde{\mathbf{\Phi}}_{\mathbf{PI}}}{dt^2} = -(\boldsymbol{LC})^{-\mathbf{1}}\widetilde{\mathbf{\Phi}}_{\mathbf{PI}}. \tag{2.31}$$

We demonstrate in Appendix B that the matrix $(\boldsymbol{LC})^{-\mathbf{1}}$ is diagonalizable and has positive and real eigenvalues. It stems from the symmetry and positive definiteness of the matrices $\boldsymbol{C}$ and $\boldsymbol{L}$. As matrix multiplication do not preserve the property of symmetry, the matrix $\boldsymbol{P}$ diagonalizing $(\boldsymbol{LC})^{-\mathbf{1}}$ is not necessarily orthogonal (nor unitary). We thus introduce the matrix $\boldsymbol{P}$ such that

$$\boldsymbol{P}(\boldsymbol{LC})^{-\mathbf{1}}\boldsymbol{P}^{-\mathbf{1}} = \begin{bmatrix} \omega_1^2 & 0 & 0 & .. & .. \\ 0 & \omega_2^2 & 0 & .. & .. \\ 0 & .. & .. & .. & .. \\ 0 & .. & .. & 0 & \omega_M^2 \end{bmatrix} = \boldsymbol{\omega}^{\mathbf{2}}. \tag{2.32}$$

The fluxes are related to the eigenmodes $\mathbf{\Phi}$ via

$$\widetilde{\mathbf{\Phi}}_{\mathbf{PI}} = \boldsymbol{P}^{-\mathbf{1}}\mathbf{\Phi}, \tag{2.33}$$

and it holds that

$$\frac{d^2\Phi_k}{dt^2} = -\omega_k^2\Phi_k \quad \text{for } k = 1, 2, .., M. \tag{2.34}$$

These equations describe a set of uncoupled harmonic oscillators and therefore the solutions for the eigenmodes are of the form $\Phi_k(t) = A_k e^{i\omega_k t} + B_k e^{-i\omega_k t}$. Starting from the Lagrangian in Eq. (2.27) and using Eq. (2.33), let us now demonstrate that in the eigenmode basis we obtain a sum of uncoupled harmonic oscillators. The Lagrangian in terms of normal modes reads

$$\mathcal{L}(\mathbf{\Phi}, \dot{\mathbf{\Phi}}) = \frac{1}{2}\dot{\mathbf{\Phi}}^T (\boldsymbol{P}^{-1})^T \boldsymbol{C}\boldsymbol{P}^{-1}\dot{\mathbf{\Phi}} - \frac{1}{2}\mathbf{\Phi}^T (\boldsymbol{P}^{-1})^T \boldsymbol{L}^{-1}\boldsymbol{P}^{-1}\mathbf{\Phi}. \tag{2.35}$$

As $\boldsymbol{C}$ is invertible, the identity $\boldsymbol{I} = \boldsymbol{C}\boldsymbol{C}^{-1}$ can be introduced on the right term

$$L(\mathbf{\Phi}, \dot{\mathbf{\Phi}}) = \frac{1}{2}\dot{\mathbf{\Phi}}^T (\boldsymbol{P}^{-1})^T \boldsymbol{C}\boldsymbol{P}^{-1}\dot{\mathbf{\Phi}} - \frac{1}{2}\mathbf{\Phi}^T (\boldsymbol{P}^{-1})^T \boldsymbol{C}\boldsymbol{C}^{-1}\boldsymbol{L}^{-1}\boldsymbol{P}^{-1}\mathbf{\Phi}. \tag{2.36}$$

Similarly, the identity $\boldsymbol{I} = \boldsymbol{P}^{-1}\boldsymbol{P}$ is introduced on the right term

$$L(\mathbf{\Phi}, \dot{\mathbf{\Phi}}) = \frac{1}{2}\dot{\mathbf{\Phi}}^T (\boldsymbol{P}^{-1})^T \boldsymbol{C}\boldsymbol{P}^{-1}\dot{\mathbf{\Phi}} - \frac{1}{2}\mathbf{\Phi}^T (\boldsymbol{P}^{-1})^T \boldsymbol{C}\boldsymbol{P}^{-1}\boldsymbol{P}\boldsymbol{C}^{-1}\boldsymbol{L}^{-1}\boldsymbol{P}^{-1}\mathbf{\Phi}, \tag{2.37}$$

in order to replace $\boldsymbol{P}\boldsymbol{C}^{-1}\boldsymbol{L}^{-1}\boldsymbol{P}^{-1}$ by the diagonal matrix $\boldsymbol{\omega^2}$. This gives

$$L(\mathbf{\Phi}, \dot{\mathbf{\Phi}}) = \frac{1}{2}\dot{\mathbf{\Phi}}^T (\boldsymbol{P}^{-1})^T \boldsymbol{C}\boldsymbol{P}^{-1}\dot{\mathbf{\Phi}} - \frac{1}{2}\mathbf{\Phi}^T (\boldsymbol{P}^{-1})^T \boldsymbol{C}\boldsymbol{P}^{-1}\boldsymbol{\omega^2}\mathbf{\Phi}. \tag{2.38}$$

Crucially, the matrix

$$\boldsymbol{C}_{\text{eff}} = (\boldsymbol{P}^{-1})^T \boldsymbol{C}\boldsymbol{P}^{-1} \tag{2.39}$$

is always diagonal with real and positive eigenvalues as we show in detail in Appendix B. $\boldsymbol{C}_{\text{eff}}$ is called the effective capacitance matrix and its diagonal elements are denoted by $C_{k,\text{eff}}$. Thus, as expected, we are able to write the Lagrangian as a collection of uncoupled harmonic oscillators:

$$\mathcal{L}(\dot{\mathbf{\Phi}}, \mathbf{\Phi}) = \sum_{k=1}^{M} \frac{C_{k,\text{eff}}}{2}\dot{\Phi}_k^2 - \frac{C_{k,\text{eff}}\omega_k^2}{2}\Phi_k^2. \tag{2.40}$$

Before passing to the Hamiltonian we perform a useful rescaling. This will provide a better connection to the impedance representation of the problem. The impedance representation and its connection with the eigenmode approach are introduced in Appendix C. We consider an arbitrary capacitance C and we rescale the variables as

$$\Phi_k \to \sqrt{\frac{C}{C_{k,\text{eff}}}}\Phi_k. \tag{2.41}$$

After this rescaling the Lagrangian reads

$$\mathcal{L}(\dot{\mathbf{\Phi}}, \mathbf{\Phi}) = \sum_{k=1}^{M} \frac{C}{2}\dot{\Phi}_k^2 - \frac{C\omega_k^2}{2}\Phi_k^2. \tag{2.42}$$

We see that now each harmonic oscillator has the same arbitrary capacitance. In this eigenmode basis, getting the canonical conjugate variable associated with Φ_k is straightforward as there is no more coupling between the variables. Defining the vector of conjugate variables as

$$\boldsymbol{Q} = \frac{\partial \mathcal{L}}{\partial \dot{\boldsymbol{\Phi}}} = C\dot{\boldsymbol{\Phi}}, \tag{2.43}$$

we can obtain the Hamiltonian

$$H(\boldsymbol{\Phi}, \boldsymbol{Q}) = \sum_{k=1}^{M} \frac{Q_k^2}{2C} + \frac{C\omega_k^2}{2}\Phi_k^2 = \sum_{k=1}^{M} \frac{Q_k^2}{2C} + \frac{\Phi_k^2}{2L_k}, \tag{2.44}$$

with the effective inductances $L_k = 1/(C\omega_k^2)$. In order to obtain the quantum Hamiltonian, the first quantization is performed by imposing canonical commutation relations between the flux and charge variables, which are promoted to operators :

$$[\hat{\Phi}_k, \hat{Q}_l] = i\hbar\delta_{kl}. \tag{2.45}$$

We now express the fluxes and charges in terms of the associated creation and annihilation operators :

$$\hat{\Phi}_k = \sqrt{\frac{\hbar Z_k}{2}}\left(\hat{a}_k^\dagger + \hat{a}_k\right), \tag{2.46a}$$

$$\hat{Q}_k = i\sqrt{\frac{\hbar}{2Z_k}}\left(\hat{a}_k^\dagger - \hat{a}_k\right). \tag{2.46b}$$

Here the characteristic impedance of mode $k = 1, \ldots, M$ are defined as

$$Z_k = \sqrt{\frac{L_k}{C}}. \tag{2.47}$$

The annihilation and creation operators obey the commutation relations

$$[\hat{a}_k, \hat{a}_l] = 0, \quad [\hat{a}_k, \hat{a}_l^\dagger] = \delta_{kl}. \tag{2.48}$$

Thus, in the eigenmode basis, the linear part of the Hamiltonian is a sum of quantum harmonic oscillators:

$$\hat{H}_{\text{lin}} = \sum_{k=1}^{M} \hbar\omega_k \left(\hat{a}_k^\dagger \hat{a}_k + \frac{1}{2}\right). \tag{2.49}$$

The flux at the ports can be expressed as a linear combination of the elements of $\boldsymbol{\Phi}$ as

$$\hat{\Phi}_{\boldsymbol{P}n} = \sum_{k=1}^{M} (\boldsymbol{P}^{-1})_{nk} \sqrt{\frac{C}{C_{k,\text{eff}}}} \hat{\Phi}_k. \tag{2.50}$$

Finally, and importantly, substituting Eq. (2.46a) in Eq. (2.50) provides an expression for the flux at the ports in terms of the normal mode creation and annihilation operators, $\hat{a}_k^\dagger$ and $\hat{a}_k$:

$$\hat{\Phi}_{\boldsymbol{P}n} = \sum_{k=1}^{M} (\boldsymbol{P}^{-1})_{nk} \sqrt{\frac{C}{C_{k,\text{eff}}}} \sqrt{\frac{\hbar Z_k}{2}} \left(\hat{a}_k^\dagger + \hat{a}_k\right), \quad n = 1, \ldots, N. \tag{2.51}$$

This allows us to generalize the approach of Refs. [14] and [29] to the multi-port case treating the non-linearity as an additional coupling between the normal modes of the linear part of the circuit, which is exactly diagonalized.

In the previous derivations, the Lagrangian is expressed in terms of the flux variables and using the inductance and capacitance matrices. Alternatively, it can be expressed in terms of the phases variables

$$\boldsymbol{\varphi} = \frac{2\pi \boldsymbol{\Phi}}{\Phi_0}. \tag{2.52}$$

Then, we use the charging and the Josephson energy matrices $\boldsymbol{E_c}$ and $\boldsymbol{E_L}$, respectively. We introduce the inverse of the charging energy as

$$\boldsymbol{E_c}^{-1} = \frac{2}{e^2} \boldsymbol{C} \tag{2.53}$$

and the Josephsons energy matrix as

$$\boldsymbol{E_L} = \frac{h^2}{16 e^2 \pi^2} \boldsymbol{L^{-1}}. \tag{2.54}$$

The advantage of working with phase variables is that they have no units. The eigenvalue problem is essentially the same as it consists in diagonalizing $\boldsymbol{E_c E_L}$ instead of $(\boldsymbol{LC})^{-\mathbf{1}}$, which are related by a proportionality constant. For convenience, we will use this second approach when we study the circuit of two capacitively coupled transmons in Sec. 3.1.2.

2.2.2 Discussion of the approximations

Let us consider again the non-linear part of the Josephson potential which have been kept out of the linear network previously analyzed. In the normal mode basis, the non-linear Hamiltonian reads

$$\hat{H}_{\text{nonlin}} = \sum_{u=2}^{\infty} \sum_{n=1}^{N} E_{J_n} \left[(-1)^{u+1} \frac{1}{(2u)!} \left(\frac{2\pi}{\Phi_0}\right)^{2u} \left(\sum_k (\boldsymbol{P^{-1}})_{nk} \sqrt{\frac{C}{C_{k,\text{eff}}}} \hat{\Phi}_k \right)^{2u} \right] \tag{2.55}$$

and inserting Eq. (2.51) it becomes

$$\hat{H}_{\text{nonlin}} = \sum_{u=2}^{\infty} \sum_{n=1}^{N} E_{J_n} \left[(-1)^{u+1} \frac{1}{(2u)!} \left(\frac{2\pi}{\Phi_0} \right)^{2u} \left(\sum_k (\boldsymbol{P^{-1}})_{nk} \sqrt{\frac{C}{C_{k,\text{eff}}}} \sqrt{\frac{\hbar Z_k}{2}} (\hat{a}_k^\dagger + \hat{a}_k) \right)^{2u} \right]. \tag{2.56}$$

In what follows, we present the different approximations which can be applied to $\hat{H}_{\text{nonlin}}$.

1. Taylor expansion highest order approximation

   The first approximation is the choice of the order $2u$ of the Taylor expansion. The Hamiltonian resulting from the lth order Taylor expansion will be denoted as $\hat{H}^{(l)}$. For example choosing the 8th order, we get :

$$\hat{H}^{(8)}_{\text{nonlin}} = \sum_{n=1}^{N} E_{J_n} \left[-\frac{1}{4!} \left(\frac{2\pi}{\Phi_0} \right)^4 \Phi^4_{\boldsymbol{P}n} + \frac{1}{6!} \left(\frac{2\pi}{\Phi_0} \right)^6 \Phi^6_{\boldsymbol{P}n} - \frac{1}{8!} \left(\frac{2\pi}{\Phi_0} \right)^8 \Phi^8_{\boldsymbol{P}n} \right]. \tag{2.57}$$

2. Rotating-wave approximation

   The Hamiltonian resulting from the lth order expansion with a rotating-wave approximation applied on top is denoted by $\hat{H}^{(l)}_{\text{RWA}}$. Applying the rotating wave approximation results in keeping only terms with equal overall number of annihilation as creation operators. For example, in 4th order, terms like $\hat{a}_1\hat{a}_2\hat{a}_2^\dagger\hat{a}_3^\dagger$ are kept, while terms like $\hat{a}_1\hat{a}_2\hat{a}_2\hat{a}_3^\dagger$ are dropped.

3. Full rotating-wave approximation

   We introduce a further approximation referred to as full RWA and denoted by $\hat{H}^{(l)}_{\text{fullRWA}}$. This approximation is even more selective as it keeps only terms which have the same number of annihilation as creation operators for each eigenmodes. From our last example, $\hat{a}_1\hat{a}_2\hat{a}_2^\dagger\hat{a}_3^\dagger$ would be dropped because there is neither a creation operator for mode 1, nor an annihilation operator for mode 3. On the contrary, terms like $\hat{a}_1\hat{a}_2\hat{a}_2^\dagger\hat{a}_1^\dagger$ are kept.

   The 4th full RWA approximation provides two analytical types of corrections on the linear Hamiltonian : self-Kerr and cross-Kerr terms. For example, at 4th order, each mode k has a self-Kerr term of the form $\delta_k\hat{a}_k^\dagger\hat{a}_k\hat{a}_k^\dagger\hat{a}_k$, while the cross-Kerr interaction between each pair of modes i and j is described by $\chi_{ij}\hat{a}_i^\dagger\hat{a}_i\hat{a}_j^\dagger\hat{a}_j$, where

δ_k and χ_{ij} denote, respectively, the self-Kerr and cross-Kerr coefficients. We define $\chi_{ij} = E_{11} - E_{10} - E_{01}$, assuming $E_{00} = 0$, as the coefficient that multiplies $\hat{a}_i^\dagger \hat{a}_i \hat{a}_j^\dagger \hat{a}_j$ in the 4th full RWA approximation. We point out that in the previous definition in Eq. (1.1), χ_{ij} is denoted with χ as we considered only two modes. We emphasize that the self-Kerr and cross-Kerr coefficients, as well as the Hamiltonian, are obtained only from the solution of the classical problem. In other words, solving a system with M degrees of freedom only requires the diagonalization of the $(\boldsymbol{LC})^{-1}$ matrix of size $M \times M$, at the Lagrangian level. Thereby, as no further diagonalization is needed in the Hilbert space, this suggests that the full RWA approximation could be a scalable way of estimating crosstalk from neighbouring qubits via the analytical expression of the cross-Kerr coefficients.

Explicit analytical formulas for the 4th order RWA are provided in what follows. At 4th order, the non-linear term reads:

$$\hat{H}^{(4)}_{\text{nonlin}} = -\sum_{n=1}^{N} \frac{E_{J_n}}{24} \left(\frac{2\pi}{\Phi_0}\right)^4 \left(\sum_{k=1}^{M} (\boldsymbol{P}^{-1})_{nk} \sqrt{\frac{C}{C_{k,\text{eff}}}} \hat{\Phi}_k\right)^4. \tag{2.58}$$

For each Josephson junction there are two kinds of terms that possess equal number of annihilation as creation operators for the same normal mode. The associated Hamiltonians are given in what follows.

- Firstly, the self-Kerr Hamiltonian of mode k associated with Josephson junction n, $\hat{H}^{(nk)}_{\text{selfKerr}}$, is derived from

$$\begin{aligned} \hat{H}^{(nk)} &= -\frac{E_{J_n}}{24} \left(\frac{2\pi}{\Phi_0}\right)^4 (\boldsymbol{P}^{-1})^4_{nk} \left(\frac{C}{C_{k,\text{eff}}}\right)^2 \hat{\Phi}_k^4 \\ &= -\frac{E_{J_n}}{24} \left(\frac{2\pi}{\Phi_0}\right)^4 (\boldsymbol{P}^{-1})^4_{nk} \left(\frac{C}{C_{k,\text{eff}}}\right)^2 \frac{\hbar^2 Z_k^2}{4} \left(\hat{a}_k^\dagger + \hat{a}_k\right)^4. \end{aligned} \tag{2.59}$$

  The self-Kerr of mode k involves terms having the same number of $\hat{a}_k^\dagger$ as $\hat{a}_k$. The commutation relation defined in Eq. (2.48) are used in order to simplify the expression

$$(\hat{a}_k + \hat{a}_k^\dagger)^4 \overset{\text{RWA}}{=} 3 + 12\hat{a}_k^\dagger \hat{a}_k + 6\hat{a}_k^\dagger \hat{a}_k^\dagger \hat{a}_k \hat{a}_k, \tag{2.60}$$

  and neglecting the constant term we get

$$\hat{H}^{(nk)}_{\text{selfKerr}} \overset{\text{RWA}}{=} \frac{\delta_{nk}}{2} \hat{a}_k^\dagger \hat{a}_k^\dagger \hat{a}_k \hat{a}_k + \delta_{nk} \hat{a}_k^\dagger \hat{a}_k. \tag{2.61}$$

Here the anharmonicity of mode k due to junction n is defined as

$$\delta_{nk} = -\frac{E_{J_n}}{8}\left(\frac{2\pi}{\Phi_0}\right)^4 (\boldsymbol{P}^{-1})^4_{nk}\Big(\frac{C}{C_{k,\text{eff}}}\Big)^2 \hbar^2 Z_k^2. \tag{2.62}$$

In terms of energy levels, the anharmonicity of mode k is defined as $\delta_k = (E_2 - E_1) - (E_1 - E_0)$ [19], where we denote E_m as the energy corresponding to the state with m excitations in mode k and no excitation in the other modes. The total self-Kerr coefficient of mode k, that is its anharmonicity, is obtained in the RWA approximation by summing over the ports:

$$\delta_k = \sum_{n=1}^{N} \delta_{nk}. \tag{2.63}$$

- Secondly, we denote the cross-Kerr Hamiltonian between each pair of modes i and j due to junction n, where i and j run from 1 to M and $i \neq j$, with $\hat{H}^{(n)}_{\text{crossKerr i,j}}$. For such a pair, the 4th full RWA approximation keeps terms with a single operator $\hat{a}_i^\dagger$, $\hat{a}_j^\dagger$, $\hat{a}_i$ and $\hat{a}_j$. This is why in Eq. (2.58), the cross-Kerr between mode i and j only involves terms with the product between Φ_i^2 and Φ_j^2. In order to derive $\hat{H}^{(n)}_{\text{crossKerr i,j}}$, we start from

$$\begin{aligned}\hat{H}^{(n)}_{ij} = -\frac{E_{J_n}}{24}\left(\frac{2\pi}{\Phi_0}\right)^4 (\boldsymbol{P}^{-1})^2_{ni}(\boldsymbol{P}^{-1})^2_{nj} 6 \frac{C^2}{C_{i,\text{eff}} \cdot C_{j,\text{eff}}} \Phi_i^2 \Phi_j^2 = \\ -\frac{E_{J_n}}{24}\left(\frac{2\pi}{\Phi_0}\right)^4 (\boldsymbol{P}^{-1})^2_{ni}(\boldsymbol{P}^{-1})^2_{nj} 6 \frac{C^2}{C_{i,\text{eff}} \cdot C_{j,\text{eff}}} \frac{\hbar^2 Z_i Z_j}{4} \big(\hat{a}_i^\dagger + \hat{a}_i\big)^2 \big(\hat{a}_j^\dagger + \hat{a}_j\big)^2.\end{aligned} \tag{2.64}$$

We use the fact that in the full RWA

$$\big(\hat{a}_i^\dagger + \hat{a}_i\big)^2 \big(\hat{a}_j^\dagger + \hat{a}_j\big)^2 \overset{\text{fullRWA}}{=} 1 + 2\hat{a}_i^\dagger \hat{a}_i + 2\hat{a}_j^\dagger \hat{a}_j + 4\hat{a}_i^\dagger \hat{a}_i \hat{a}_j^\dagger \hat{a}_j. \tag{2.65}$$

Thus, neglecting constant terms and summing over each port n as well as on each pair of modes, i and j, the total cross-Kerr Hamiltonian reads :

$$\hat{H}_{\text{crossKerr}} \overset{\text{fullRWA}}{=} \sum_{n=1}^{N} \sum_{i=1}^{M} \sum_{\substack{j=1 \\ i \neq j}}^{M} \frac{\chi^{(n)}_{ij}}{2} \hat{a}_i^\dagger \hat{a}_i + \frac{\chi^{(n)}_{ij}}{2} \hat{a}_j^\dagger \hat{a}_j + \chi^{(n)}_{ij} \hat{a}_i^\dagger \hat{a}_i \hat{a}_j^\dagger \hat{a}_j, \tag{2.66}$$

where the cross-Kerr coupling between mode i and j due to junction n are

$$\chi_{ij}^{n} = -\frac{E_{J_n}}{4}\left(\frac{2\pi}{\Phi_0}\right)^4 (\boldsymbol{P^{-1}})_{ni}^2 (\boldsymbol{P^{-1}})_{nj}^2 \frac{C^2}{C_{i,\text{eff}} \cdot C_{j,\text{eff}}} Z_i Z_j \hbar^2. \tag{2.67}$$

Then, the total cross-Kerr coefficient between the 2 modes is obtained by summing over the ports:

$$\chi_{ij} = \sum_{n=1}^{N} \chi_{ij}^{n}. \tag{2.68}$$

We have obtained an analytical expression for χ_{ij}, which is the crosstalk between the two qubits associated with mode i and j discussed in Sec. 1.2. In the 4th order full RWA approximation, the diagonal Hamiltonian is given by :

$$\hat{H}_{\text{fullRWA}}^{(4)} = \sum_{k=1}^{M} \left[\Omega_k \hat{a}_k^\dagger \hat{a}_k + \frac{\delta_k}{2} \hat{a}_k^\dagger \hat{a}_k^\dagger \hat{a}_k \hat{a}_k + \sum_{\substack{j=1 \\ j\neq k}}^{M} \chi_{kj} \hat{a}_k^\dagger \hat{a}_k \hat{a}_j^\dagger \hat{a}_j\right], \tag{2.69}$$

where Ω_k is the renormalized frequency of mode k given by:

$$\Omega_k = \omega_k + \delta_k + \frac{1}{2} \sum_{\substack{j=1 \\ j\neq k}}^{M} \chi_{kj}. \tag{2.70}$$

2.3 Theory of the CPHASE

A two-qubit gate that is commonly used to form the universal set of gates is the conditional-phase gate, also known as a CPHASE or CZ gate. It applies a $Z = \begin{pmatrix} 1 & 0 \\ 0 & -1 \end{pmatrix}$ gate on the target qubit if the control qubit is in state $|1\rangle$ [18]. A CPHASE gate is described by the unitary operator

$$U_{CPHASE} = \begin{pmatrix} 1 & 0 & 0 & 0 \\ 0 & 1 & 0 & 0 \\ 0 & 0 & 1 & 0 \\ 0 & 0 & 0 & -1 \end{pmatrix}. \tag{2.71}$$

For concreteness, we consider a high frequency and a medium frequency transmon qubit, denoted by Q_H and Q_M respectively, in the DiCarlo architecture [5]. As these transmons are capacitively shunted SQUID loops, introduced in Subsec. 2.1.3, their frequency can be controlled by means of an external flux pulse, $\Phi_H^{ext}(t)$. A CPHASE gate between these qubits is implemented by tuning in and out of resonance an interaction in the second-excitation manifold between the states $|0_M 2_H\rangle$ and $|1_M 1_H\rangle$ [30]. In other words, an external flux pulse, $\Phi_H^{ext}(t)$, is applied to the high frequency qubit in order to lower its Josephson energy, and thus also its frequency ω_H, until the point where an avoided crossing between the states $|0_M 2_H\rangle$ and $|1_M 1_H\rangle$ occurs [11]. An example of the CPHASE operating point is shown in Figs. 2.3.1a and 2.3.1b, considering a system of two capacitively coupled transmons. As the $|0_M 2_H\rangle$ state is not part of the computational subspace, we want to avoid any energy transfer to this state at the end of the gate. This is typically done using a special pulse-shape known as a fast-adiabatic pulse that minimizes the leakage as presented in [31]. We would like to point out that from now on, the basis notation without subscript, $|ij\rangle$, denotes the basis $|i_M j_H\rangle$ and that when we use phase instead of flux variables, the external pulse applied to Q_H is denoted by $\varphi_H^{ext}(t) = (2\pi \cdot \Phi_H^{ext}(t))/\Phi_0$ where Φ_0 is the superconducting flux quantum, instead of $\Phi_H^{ext}(t)$. The parking frequency is chosen at a flux sweet spot, i.e. at a point where the first derivative of the Josephson junctions with respect to the external flux is zero:

$$\frac{\partial E_J(\Phi_H^{ext})}{\partial \Phi_H^{ext}} = 0. \tag{2.72}$$

We make the assumption that the sweet spot is located at $\Phi_H^{ext} = 0$, though experimentally there might be an offset [11]. This is equivalent to assuming that the Josephson energies of the two junctions in the SQUID loop, discussed in Subsec. 2.1.3, are equal.

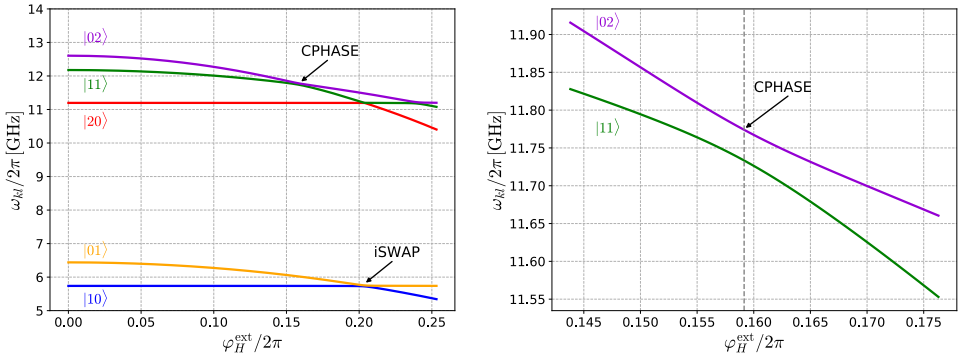

Figure 2.3.1: **a)** Energy levels of a two-capacitively coupled transmons as a function of $\varphi_H^{\text{ext}}(t)/2\pi$. The arrows indicate the points where the avoided crossing associate with CPHASE and iSWAP take place. The iSWAP is a two-qubit gate implemented by tuning the qubits in resonance in order to use the $|01\rangle$-$|10\rangle$ avoided crossing [32]. **b)** Zoom on the avoided crossing region for the CPHASE gate.

The CPHASE gate is realized in two steps for a total duration of $T = T_{2Q} + T_{1Q}$.

1. During the first step, $\Phi_H^{\text{ext}}(t)$ is applied to Q_H for a duration of T_{2Q}. It brings $|11\rangle$ to the avoided crossing with $|02\rangle$, at Φ_{AC}^{ext}, and back to acquire a conditional phase. The corresponding unitary evolution is denoted by $\mathrm{U_{2Q}}$. We take out the global phase and define

$$\mathrm{U_{2Q}} = \begin{pmatrix} 1 & 0 & 0 & 0 \\ 0 & e^{i\beta_{10}} & 0 & 0 \\ 0 & 0 & e^{i\beta_{01}} & 0 \\ 0 & 0 & 0 & e^{i\beta_{11}} \end{pmatrix}, \tag{2.73}$$

   where β_{ij} denote the phases acquired by the states $|ij\rangle$ during T_{2Q}. The conditional phase is given by $\phi_{2Q} = \beta_{11} - \beta_{10} - \beta_{01}$.

2. The phases β_{ij} are used in the second step in order to define the single-qubit rotation corrections $\mathrm{R_z}(-\beta_{01}) \otimes \mathrm{I}$ and $\mathrm{I} \otimes \mathrm{R_z}(-\beta_{10})$, where I is the identity on the other qubit [30]. We recover the CPHASE gate from Eq. (2.71) if the conditional phase ϕ_{2Q} is an odd multiple of π.

The total simulation implements the operator $\mathrm{U_{sim}}$, defined as the product:

$$\mathrm{U_{sim}} = (\mathrm{R_z}(-\beta_{01}) \otimes \mathrm{I})(\mathrm{I} \otimes \mathrm{R_z}(-\beta_{10}))\mathrm{U_{2Q}}. \tag{2.74}$$

We introduce the adiabatic conditional phase as

$$\phi_{2Q}^{\text{ad}} = \int_0^T 2\pi(E_{11}(t) - E_{01}(t) - E_{10}(t))dt, \tag{2.75}$$

assuming the lowest energy level to satisfy $E_{00}(t) = 0$. The 2π comes from the fact that the energy levels are expressed in units of h. In the case of adiabatic evolution, it holds that $\phi_{2Q}^{\text{ad}} = \beta_{11} - \beta_{10} - \beta_{01}$. We further give the cross-Kerr coefficient in terms of the energy level as

$$\chi(\Phi_H^{\text{ext}}(t)) = E_{11}(\Phi_H^{\text{ext}}(t)) - E_{01}(\Phi_H^{\text{ext}}(t)) - E_{10}(\Phi_H^{\text{ext}}(t)). \tag{2.76}$$

In the case of adiabatic evolution it turns out that

$$\phi_{2Q}^{\text{ad}} = \int_0^T 2\pi \cdot \chi(\Phi_H^{\text{ext}}(t)) \quad dt. \tag{2.77}$$

This means that the cross-Kerr as defined in Eq. (2.76) causes the conditional phase to be acquired in the adiabatic case.

2.3.1 Adiabatic vs Diabatic pulsing

Let us introduce two basis involved while pulsing from zero to the avoided crossing. Firstly there is the eigenmode basis at zero flux, $\{ |ij\rangle_0\}$, which results from diagonalizing the linear part of the Hamiltonian when $\Phi_H^{\text{ext}}(t) = 0$, see Subsec. 2.2.1. This is the computational basis in which the states are initialized in the simulations. Secondly, diagonalization of the full Hamiltonian while the external flux, $\Phi_H^{\text{ext}}(t)$, is changed leads for each time t to the instantaneous eigenstates basis, $\{ \widetilde{|ij\rangle}(t)\}$ associated with the energy levels.

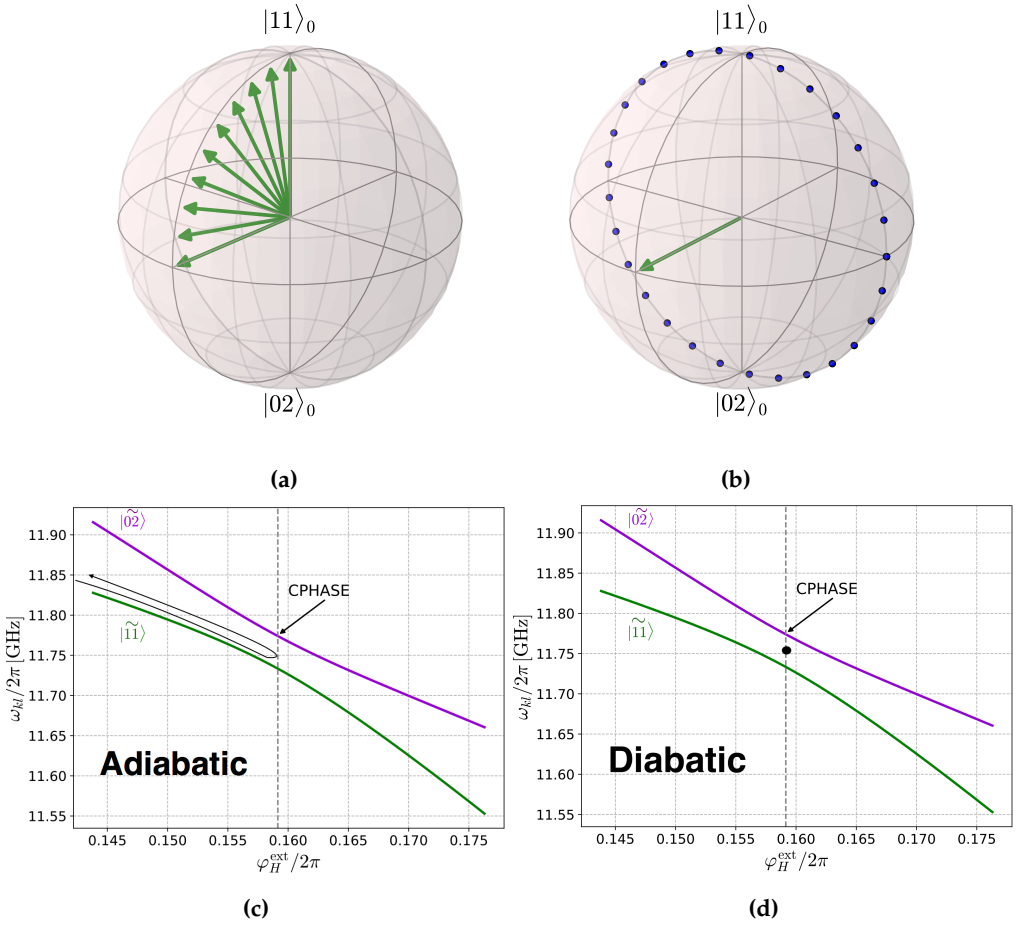

Figure 2.3.2: Two ways of driving a CPHASE: Adiabatically or Diabatically. Figs. **a)** and **b)** show, respectively, the adiabatic and diabatic evolution of a state initialized in $|11\rangle_0$ in a two-level Bloch sphere representation. The green arrows represent the axis parallel to the instantaneous eigenstates. In Fig. **a)**, the state gradually evolves from the pole, in $|11\rangle_0$, to the equatorial plane and back to the pole, following the green arrow. On the trajectory, the state also makes some small rotations around the green arrow cancelled by time-averaging (not shown) [33]. Fig. **b)** depicts the diabatic evolution of $|11\rangle_0$, which rotates (blue dots) around the green arrow in the equatorial plan. It rotates at the Rabi frequency given by ΔE (in units of h) [33]. Fig. **c)** shows the adiabatic evolution of $|11\rangle_0$ remaining on the instantaneous $|\widetilde{11}\rangle(t)$, while the diabatic evolution in Fig. **d)** involves a quick change (a 'jump') of the instantaneous eigenstates. In this basis, a state initialized in $|11\rangle_0$ reads $\alpha_{\widetilde{11}}(t_j)|\widetilde{11}\rangle(t_j) + \alpha_{\widetilde{02}}(t_j)|\widetilde{02}\rangle(t_j)$ just after the jump of the eigenstates. The state indicated with the black dot corresponds to the ideal for which it holds that $\alpha_{\widetilde{11}}(t_j) = \alpha_{\widetilde{02}}(t_j) = 1/\sqrt{2}$.

Adiabatic and diabatic regime in a CPHASE context are easily understood by con-

sidering the evolution of a state intitialized in $|\psi(t=0)\rangle = |11\rangle_0$. In an approximate two-state picture, the state $|\psi(t)\rangle$ can be projected and expanded on the subspace spanned by $\{ |\widetilde{11}\rangle(t), |\widetilde{02}\rangle(t)\}$, for each time t, as:

$$|\psi(t)\rangle = \alpha_{\widetilde{11}}(t)|\widetilde{11}\rangle(t) + \alpha_{\widetilde{02}}(t)|\widetilde{02}\rangle(t) \tag{2.78}$$

Then the instantaneous probability of leakage to $|\widetilde{02}\rangle(t)$ is given by

$$p_{\widetilde{02}}(t) = |\alpha_{\widetilde{02}}(t)|^2 \tag{2.79}$$

Now, depending on the pulse shape the evolution will be completely different as it ranges between adiabatic and diabatic regimes. In an adiabatic scenario, the pulse is varied so slowly [1] that it enables the initial state $|\psi(t=0)\rangle = |11\rangle_0$ to follow the instantaneous eigenstate $|\widetilde{11}\rangle(t)$ without overlapping with $|\widetilde{02}\rangle(t)$. Therefore, perfect adiabaticity is realized if and only if $p_{\widetilde{02}}(t) = 0$ for the whole duration of the pulse. Such evolution is depicted in Fig. 2.3.2c by the black arrow. The green arrows on Fig. 2.3.2a and 2.3.2b represent the axis parallel to the instantaneous eigenstates. Varying the pulse amplitude changes the axis location. The diabatic regime is obtained in the opposite limit, i.e., by strongly and quickly pulsing to the avoided crossing point. The instantaneous eigenstates are brutally modified jumping from the poles into the equatorial plane. Now, the intial $|11\rangle_0$ just after the 'jump', at t_j, is expressed as a linear superposition in the basis of the new instantaneous eigenstates and reads as follows:

$$|\psi(t_j)\rangle = \alpha_{\widetilde{11}}(t_j)|\widetilde{11}\rangle(t_j) + \alpha_{\widetilde{02}}(t_j)|\widetilde{02}\rangle(t_j). \tag{2.80}$$

The values of the coefficients depend on the pulse shape. The point in between the energy levels in Fig. 2.3.2d corresponds to the ideal case when $\alpha_{\widetilde{11}}(t_j) = \alpha_{\widetilde{02}}(t_j) = 1/\sqrt{2}$. The arrow in Fig. 2.3.2b lies on the equatorial plane, therefore the instantaneous eigenstates at the avoided-crossing are the symmetric and anti-symmetric equal superposition :

$$\begin{aligned} |\widetilde{11}\rangle &= \frac{|11\rangle_0 + |02\rangle_0}{\sqrt{2}} \\ |\widetilde{02}\rangle &= \frac{|11\rangle_0 - |02\rangle_0}{\sqrt{2}}, \end{aligned} \tag{2.81}$$

[1] The slow variation of the pulse should ensure that the commonly used approximate adiabatic criterion: $\sum_{m\neq n} \frac{|\hbar\langle m|\dot{\boldsymbol{H}}|n\rangle|}{|E_n - E_m|^2} \ll 1$ is satisfied [34].

In this Bloch sphere representation, a state under a diabatic evolution rotates around the instantaneous eigenstates (direction pointed by the green arrow) at frequency ΔE [33]. Consequently, if the arrow of a diabatic pulse is a bit above/below the equatorial plane, the Rabi oscillation (from a state initialized in $|11\rangle_0$ for example) will not perform a full 2π rotation between the states $|11\rangle_0$ and $|02\rangle_0$. The duration required for the state $|11\rangle_0$ in order to perform a complete Rabi oscillation between $|11\rangle_0$ and $|02\rangle_0$ is given by [30]:

$$T_{\text{Rabi}} = \frac{1}{\Delta E_{AC}}. \tag{2.82}$$

Here we give the size of the gap at the avoided crossing, $\Delta E_{AC} = E_{02}(\Phi_{AC}^{\text{ext}}) - E_{11}(\Phi_{AC}^{\text{ext}})$, in units of h. If we choose $T_{2Q} = T_{\text{Rabi}}$, then the leakage out of the computational basis is minimized and the overall controlled phase picked up by $|11\rangle_0$ is $\phi_{2Q} \approx \pi$ [30], [35]. For a diabatic pulse, the fidelity relies on the matching between T_{Rabi} and the duration resulting in $\phi_{2Q} = \pi$. In conclusion, the speed of the CPHASE gate is set by the size of the gap at the avoided crossing in the case of diabatic pulse. The same limit is also true for adiabatic pulse. However, we argue that with a diabatic pulse the external flux is slowly applied to Q_H, in other words the system is slowly placed at the avoided crossing, so that it spends less time sitting at this point. Then, the size of the gap at the avoided crossing matters less than with a diabatic pulse. We stress that a CPHASE gate can be operated at any point where the cross-kerr interaction is non-zero. Nevertheless, the speed performance of the gate is higher if the external flux is placed at the avoided crossing point.

2.3.2 CPHASE simulation

The simulations are done in the eigenmode basis at zero flux which results from diagonalizing the linear part of the Hamiltonian when $\Phi_H^{\text{ext}}(t) = 0$, see Subsec. 2.2.1. This means that the computational basis is formed by the first four eigenstates of the linear part of the Hamiltonian at zero flux, denoted by $\{ |00\rangle_0, |10\rangle_0, |01\rangle_0, |11\rangle_0 \}$ [2]. The Hamiltonian implemented is derived with the eigenmode approach keeping the nonlinearity up to 6th order, $\hat{H}^{(6)}$, without applying the RWA approximation, see Sec. 2.2.2. We work in the Schrödinger picture with a time-dependant Hamiltonian. The approach followed in the simulations and a clarification about what terms drive effectively the CPHASE gate in the eigenmode approach are presented in Appendix A. We point out

[2]Notice that this is also the eigenbasis at zero flux within the full RWA approximation.

that the circuit used in the simulations is presented in Subsec. 3.1, where we also derive the Hamiltonian of the circuit with the eigenmode approach.

CPHASE fidelity and code implementation

Following the definition in [36] and [35], the fidelity of a simulation implementing U_{sim}, see Eq. (2.74), which aims at reproducing the ideal unitary operator U_{CPHASE}, see Eq. (2.71), is defined as follows :

$$\mathcal{F} = \frac{1}{n^2}\left|\mathrm{Tr}(U_{CPHASE}^{\dagger} U_{sim})\right|^2 \tag{2.83}$$

where n denotes the dimension of the Hilbert space, which is equal to four in the context of two-qubit gate. The simulations are run in a larger Hilbert space and only when we compute the fidelity, the evolution operator is projected onto the computational subspace. It is denoted by U_{sim}. If leakage out of the computational basis occurs, U_{sim} is not perfectly unitary, and leakage is detected as missing probability [35]. The matrix elements of U_{2Q} from Eq. (2.74) in the zero flux basis are :

$$\langle ij|_0 U_{2Q} |kl\rangle_0 \,. \tag{2.84}$$

Here $|ij\rangle_0$ and $|kl\rangle_0$ both run on the four computational basis states $\{|00\rangle_0, |10\rangle_0, |01\rangle_0, |11\rangle_0\}$. Therefore, in order to assemble U_{2Q}, the four computational basis states are sequentially simulated. Each time, the overlap between the final state, $U_{2Q}|kl\rangle_0$, and the four computational states are computed. Additionally, we use the phases of the final states to define single-qubit rotations. After these steps, we obtain the fidelity of U_{sim}. We denote the probability of the state that evolves ,$|\psi(t)\rangle$, to be found in the state $|ij\rangle_0$ at time t as :

$$P_{ij}(t) = |\alpha_{ij}(t)|^2. \tag{2.85}$$

These probabilities evaluated at the end of the CPHASE gate quantify the leakage out of the computational basis. Note that no noise is implemented as we aim to verify whether simulations using the eigenmode approach can be used to accurately model the CPHASE gate. We also keep track over time of the instantaneous probability of leakage on the states $|\widetilde{ij}\rangle(t)$, which are out of the computational basis, and denote these probabilities by $p_{\widetilde{ij}}(t)$. We are especially interested in $p_{\widetilde{02}}(t)$ as it is provides information about the regime we are working in, see Subsec. 2.3.1. Roughly it is a measure of "how much adiabatic or diabatic" the evolution under a given pulse is. Finally, the fidelity in Eq. (2.83) is optimized by varying the pulse parameters τ_I and mainly τ_R, see Fig. 2.3.3.

Pulse

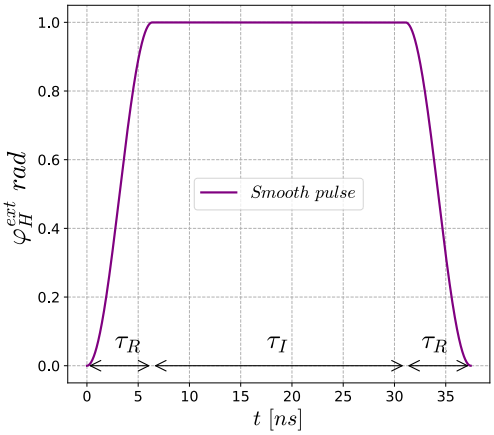

Figure 2.3.3: External pulse applied to Q_H in order to induce $|11\rangle_0$-$|02\rangle_0$ avoided crossing.

The function associated with the external phase applied to Q_H is :

$$\varphi_H^{\text{ext}}(t) = \begin{cases} \varphi_{AC}^{\text{ext}}/2 \cdot (1 - \cos(\frac{\pi t}{\tau_R})) & \text{if } 0 \leq t < \tau_R \\ \varphi_{AC}^{\text{ext}} & \text{if } \tau_R \leq t < \tau_R + \tau_I \\ \varphi_{AC}^{\text{ext}}/2 \cdot (1 + \cos(\frac{\pi(t-\tau_R-\tau_I)}{\tau_R})) & \text{if } \tau_R + \tau_I \leq t < 2\tau_R + \tau_I \end{cases} \tag{2.86}$$

Here τ_R is the time during which the pulse moves from the parking frequency to the operating point of the CPHASE gate, $\varphi_{AC}^{\text{ext}}$. It corresponds to the avoided crossing point between $|11\rangle_0$ and $|02\rangle_0$. The pulse stays at $\varphi_{AC}^{\text{ext}}$ during τ_I and then moves back to the parking frequency during τ_R.

Chapter 3

Two transmon qubits

In this chapter we start by analyzing a system of two transmons capacitively coupled in Subsec. 3.1. More specifically, we compare the exact solution, in the Cooper-pair basis, with the different approximations from the eigenmode approach, presented in Subsec. 2.2.2. This analysis allows us to validate which approximations are accurate as well as to propose a model for CPHASE simulation in presence of ZZ crosstalk in Subsecs. 3.1.3 and 3.1.4, respectively. Subsequently, CPHASE simulations without crosstalk are carried out in Subsec. 3.2 and finally, we question in Subsec. 3.3 whether the CPHASE simulations with the two capacitively coupled transmons considered in Subsec. 3.2 would be significantly modified for a system of two transmons coupled via a resonator.

3.1 Two capacitively coupled transmons analysis

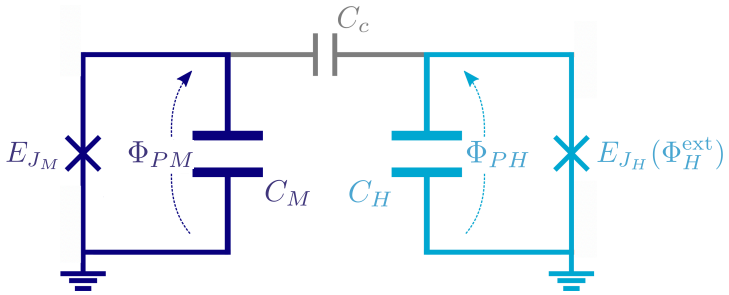

Figure 3.1.1: Circuit of two capacitively coupled transmons. The fluxes across the transmons are denoted with Φ_{PM} and Φ_{PH}. The transmon on the left (right) is associated with the medium (high) frequency qubit Q_M (Q_H) in the CPHASE gate. The Josephson junction of the high frequency qubit is tunable by means of an external flux and is indicated by $E_{J_H}(\Phi_H^{\text{ext}})$.

We would like to apply the eigenmode approach, derived in Subsec. 2.2.1, on the circuit of two capacitively coupled transmons depicted in Fig. 3.1.1. The latter is characterized by the capacitance matrix

$$\boldsymbol{C} = \begin{pmatrix} C_M + C_c & -C_c \\ -C_c & C_H + C_c \end{pmatrix}, \tag{3.1}$$

where C_i with $i = M, H$ are the capacitances of the shunting transmons and C_c is the coupling capacitance. The inverse of the charging energy matrix is given by

$$\boldsymbol{E}_c^{-1} = \frac{2}{e^2}\boldsymbol{C}. \tag{3.2}$$

We assume that the qubit with the highest frequency, Q_H, is tunable by means of an external flux, $\Phi_H^{\text{ext}}(t)$. The subscript H is used here in order to have the same notation as in the CPHASE analysis. The Josephson junction in Fig. 3.1.1 is replaced by a SQUID loop as explained in Subsec. 2.1.3. The inductances of the transmons are given by L_M and $L_H(\Phi_H^{\text{ext}})$, respectively. We define the inverse of the inductance matrix as

$$\boldsymbol{L^{-1}} = \begin{pmatrix} L_M^{-1} & 0 \\ 0 & L_H^{-1}(\Phi_H^{\text{ext}}) \end{pmatrix} \tag{3.3}$$

and the inductance energy matrix as

$$\boldsymbol{E_L} = \frac{h^2}{16e^2\pi^2}\boldsymbol{L^{-1}} = \begin{pmatrix} E_{J_M} & 0 \\ 0 & E_{J_H}(\Phi_H^{\text{ext}}) \end{pmatrix}. \tag{3.4}$$

The fluxes across the Josephson junctions at the ports are independent flux variables and we gather them into the vector $\widetilde{\boldsymbol{\Phi}}_{\mathbf{PI}} = \{\Phi_{\boldsymbol{P}M}, \Phi_{\boldsymbol{P}H}\}^T$. Then the Lagrangian of the circuit in Fig. 3.1.1 is

$$\mathcal{L} = \frac{1}{2}\dot{\widetilde{\boldsymbol{\Phi}}}_{\text{PI}}^T \boldsymbol{C}\dot{\widetilde{\boldsymbol{\Phi}}}_{\text{PI}} + E_{J_M}\cos\left(\frac{2\pi}{\Phi_0}\Phi_{\boldsymbol{P}M}\right) + E_{J_H}(\Phi_H^{\text{ext}})\cos\left(\frac{2\pi}{\Phi_0}\Phi_{\boldsymbol{P}H}\right). \tag{3.5}$$

In terms of phase variables the Lagrangian can be rewritten as

$$\begin{aligned} \mathcal{L} &= \frac{1}{2}\frac{e^2}{2}\frac{\Phi_0^2}{(2\pi)^2}\dot{\widetilde{\boldsymbol{\varphi}}}_{\mathbf{PI}}^T \boldsymbol{E_c^{-1}}\dot{\widetilde{\boldsymbol{\varphi}}}_{\mathbf{PI}} + \sum_{n=M}^{H} E_{Jn}\cos(\varphi_{\boldsymbol{P}n}) \\ &= \frac{\hbar^2}{16}\dot{\widetilde{\boldsymbol{\varphi}}}_{\mathbf{PI}}^T \boldsymbol{E_c^{-1}}\dot{\widetilde{\boldsymbol{\varphi}}}_{\mathbf{PI}} + \sum_{n=M}^{H} E_{Jn}\cos(\varphi_{\boldsymbol{P}n}). \end{aligned} \tag{3.6}$$

In order to derive the Hamiltonian, we introduce the vector of canonical conjugate variables and directly divide it by $\hbar$ as follows:

$$\widetilde{\boldsymbol{n}}_{\mathbf{PI}} = \frac{1}{\hbar}\frac{d\mathcal{L}}{d\dot{\widetilde{\boldsymbol{\varphi}}}_{\mathrm{PI}}} = \frac{\hbar}{8}\boldsymbol{E}_{\boldsymbol{c}}^{-\mathbf{1}}\dot{\widetilde{\boldsymbol{\varphi}}}_{\mathrm{PI}}. \tag{3.7}$$

These variables are the number of Cooper-pairs. We perform the Legendre transformation and obtain the Hamiltonian

$$\hat{H} = \left(\frac{d\mathcal{L}}{d\dot{\widetilde{\boldsymbol{\varphi}}}_{\mathrm{PI}}}\right)^{T}\dot{\widetilde{\boldsymbol{\varphi}}}_{\mathrm{PI}} - \mathcal{L} = 8\widetilde{\boldsymbol{n}}_{\mathbf{PI}}^{T}\boldsymbol{E}_{\boldsymbol{c}}\widetilde{\boldsymbol{n}}_{\mathbf{PI}} - 4\widetilde{\boldsymbol{n}}_{\mathbf{PI}}^{T}(\boldsymbol{E}_{\boldsymbol{c}})^{\boldsymbol{T}}\boldsymbol{E}_{\boldsymbol{c}}^{-\mathbf{1}}\boldsymbol{E}_{\boldsymbol{c}}\widetilde{\boldsymbol{n}}_{\mathbf{PI}} - \sum_{n=M}^{H} E_{Jn}\cos(\varphi_{\boldsymbol{P}n}). \tag{3.8}$$

The energy capacitance matrix is symmetric and thus

$$\hat{H} = 4\widetilde{\boldsymbol{n}}_{\mathbf{PI}}^{T}\boldsymbol{E}_{\boldsymbol{c}}\widetilde{\boldsymbol{n}}_{\mathbf{PI}} - \sum_{n=M}^{H} E_{Jn}\cos(\varphi_{\boldsymbol{P}n}). \tag{3.9}$$

The variables are promoted to quantum operators by imposing the canonical quantization. If we express the capacitance energy matrix, defined as the inverse of the matrix in Eq. (3.2), as

$$\boldsymbol{E}_{\boldsymbol{c}} = \begin{pmatrix} E_{c_M} & \frac{E_I}{2} \\ \frac{E_I}{2} & E_{c_H} \end{pmatrix}, \tag{3.10}$$

then the Hamiltonian is

$$\hat{H} = 4E_{c_M}\hat{n}_{\boldsymbol{P}M}^2 + 4E_{c_H}\hat{n}_{\boldsymbol{P}H}^2 + 4E_I\hat{n}_{\boldsymbol{P}M}\hat{n}_{\boldsymbol{P}H} - E_{J_M}\cos(\hat{\varphi}_{\boldsymbol{P}M}) - E_{J_H}(\Phi_H^{\mathrm{ext}})\cos(\hat{\varphi}_{\boldsymbol{P}H}). \tag{3.11}$$

3.1.1 Exact solution

The Hamiltonian in Eq. 3.11, can be directly diagonalized in the Cooper-pair basis denoted with $\{|n_{\mathrm{PM}}\rangle \otimes |n_{\mathrm{PH}}\rangle\} = \{|n_{\mathrm{PM}} n_{\mathrm{PH}}\rangle\}$. Indeed, proceeding similarly to what was done for the Cooper-Pair Box system in Sec. 2.1.2, the Hamiltonian of the two capacitively coupled transmons reads:

$$\begin{aligned}\hat{H} = \sum_{n_{\mathrm{PM}}=-\infty}^{\infty}\sum_{n_{\mathrm{PH}}=-\infty}^{\infty}\Big(4E_{c_M}n_{\mathrm{PM}}^2 + 4E_{c_H}n_{\mathrm{PH}}^2 + 4E_I n_{\mathrm{PM}}n_{\mathrm{PH}}\Big)\,|n_{\mathrm{PM}}n_{\mathrm{PH}}\rangle\langle n_{\mathrm{PM}}n_{\mathrm{PH}}| \\ -\frac{E_{J_M}}{2}\Big(|n_{\mathrm{PM}}\rangle\langle n_{\mathrm{PM}}+1| + |n_{\mathrm{PM}}+1\rangle\langle n_{\mathrm{PM}}|\Big)\otimes\Big(|n_{\mathrm{PH}}\rangle\langle n_{\mathrm{PH}}|\Big) \\ -\frac{E_{J_H}(\Phi_H^{\mathrm{ext}})}{2}\Big(|n_{\mathrm{PM}}\rangle\langle n_{\mathrm{PM}}|\Big)\otimes\Big(|n_{\mathrm{PH}}\rangle\langle n_{\mathrm{PH}}+1| + |n_{\mathrm{PH}}+1\rangle\langle n_{\mathrm{PH}}|\Big).\end{aligned} \tag{3.12}$$

3.1.2 Eigenmode approach applied

We now apply the eigenmode approach at the Lagrangian level. The Lagrangian in Eq. (3.6) is split into a linear and a non-linear part by expansion of the Josephson cosine potential as follows :

$$\begin{aligned}\mathcal{L} = \frac{\hbar^2}{16}\dot{\widetilde{\boldsymbol{\varphi}}}_{\mathbf{PI}}^{T}\boldsymbol{E}_c^{-1}\dot{\widetilde{\boldsymbol{\varphi}}}_{\mathbf{PI}} - \frac{1}{2}\widetilde{\boldsymbol{\varphi}}_{\mathbf{PI}}^{T}\boldsymbol{E}_L\widetilde{\boldsymbol{\varphi}}_{\mathbf{PI}} + \left[\sum_{n=M}^{H} E_{Jn}\cos(\varphi_{Pn}) + \frac{1}{2}\widetilde{\boldsymbol{\varphi}}_{\mathbf{PI}}^{T}\boldsymbol{E}_L\widetilde{\boldsymbol{\varphi}}_{\mathbf{PI}}\right] \\ = \mathcal{L}_{\text{lin}} + \mathcal{L}_{\text{nonlin}}\end{aligned} \tag{3.13}$$

Taking the Euler-Lagrange equations on the linear Lagrangian in Eq. (3.13), we end up with the eigenvalue problem consisting in diagonalizing the matrix $(\boldsymbol{E_L^{-1}E_c^{-1}})^{-1} = \boldsymbol{E_cE_L}$. This problem is equivalent to diagonalizing the $(\boldsymbol{LC})^{-1}$ matrix presented in Subsec. 2.2.1. Thus, proceeding similarly, an effective inverse charging energy matrix, which is diagonal, is obtained :

$$\boldsymbol{E_{c,\text{eff}}^{-1}} = (\boldsymbol{P^{-1}})^{T}\boldsymbol{E_c^{-1}P^{-1}} = \begin{pmatrix} {E_{\text{c1,eff}}}^{-1} & 0 \\ 0 & {E_{\text{c2,eff}}}^{-1} \end{pmatrix}. \tag{3.14}$$

The linear Lagrangian in terms of the eigenmodes is

$$\mathcal{L}_{\text{lin}} = \sum_{k=1}^{2} \frac{\hbar^2}{16E_{ck,\text{eff}}}\dot{\varphi}_k^2 - \frac{1}{2E_{ck,\text{eff}}}\lambda_k^2\varphi_k^2. \tag{3.15}$$

Here the λ_k^2 with $k = 1, 2$ are the eigenvalues of the $\boldsymbol{E_cE_L}$ matrix. We apply canonical quantization by promoting the variables to operators. As expected, the resulting Hamiltonian is the sum of two uncoupled harmonic oscillators:

$$\hat{H}_{\text{lin}} = \sum_{k=1}^{2} 4E_{ck,\text{eff}}\hat{n}_k^2 + \frac{1}{2E_{ck,\text{eff}}}\lambda_k^2\hat{\varphi}_k^2 \tag{3.16}$$

Finally, the operators can be expressed in terms of their annihilation and creation operators as

$$\begin{cases} \hat{\varphi}_k = \left(\frac{2E_{ck,\text{eff}}^2}{\lambda_k^2}\right)^{\frac{1}{4}}\left(\hat{a}_k^{\dagger} + \hat{a}_k\right) = \varphi_{ZPFk}\left(\hat{a}_k^{\dagger} + \hat{a}_k\right) \\ \hat{n}_k = \frac{i}{2}\left(\frac{\lambda_k^2}{2E_{ck,\text{eff}}^2}\right)^{\frac{1}{4}}\left(\hat{a}_k^{\dagger} - \hat{a}_k\right) = i \cdot n_{ZPFk}\left(\hat{a}_k^{\dagger} - \hat{a}_k\right). \end{cases} \tag{3.17}$$

Here φ_{ZPFk} and n_{ZPFk} denote the zero-point fluctuations of the phase and of the number of Cooper-pairs (of mode k), respectively [24]. When a quantum oscillator is in the ground state, its energy cannot be zero due to the uncertainty principle. The quantum ground uncertainties of the phase and of the Cooper-pair number are given by

$\varphi_{ZPF} = \langle 0| \hat{\varphi}^2 |0\rangle$ and $n_{ZPF} = \langle 0| \hat{n}^2 |0\rangle$ [24]. We point out that if $\Phi_H^{\text{ext}}(t)$ is modified the eigenmode approach can be applied at each value of $\Phi_H^{\text{ext}}(t)$. Then, at the classical level, the matrix $\boldsymbol{P}(\Phi_H^{\text{ext}})$ and the frequencies of the normal modes, $\lambda_k(\Phi_H^{\text{ext}})$, become flux-dependant. So are the operators at the quantum level, i.e. $\hat{\varphi}_k(\Phi_H^{\text{ext}})$, $\hat{n}_k(\Phi_H^{\text{ext}})$ and $\hat{a}_k(\Phi_H^{\text{ext}})$ for $k = 1, 2$. In this case, the linear Hamiltonian in Eq. (3.16) reads:

$$\hat{H}_{\text{lin}} = \sum_{k=1}^{2} \sqrt{8\lambda_k^2(\Phi_H^{\text{ext}})} \left(\hat{a}_k^\dagger(\Phi_H^{\text{ext}}) \hat{a}_k(\Phi_H^{\text{ext}}) + \frac{1}{2} \right) \tag{3.18}$$

We remark that instead of applying the eigenmode at each value of $\Phi_H^{\text{ext}}(t)$, we can look at the coupling induced by the tuning of $\Phi_H^{\text{ext}}(t)$ from the perspective of the normal modes at zero flux, i.e. the modes associated with $\hat{a}_k(\Phi_H^{\text{ext}} = 0)$. In this case, there is a linear coupling induced between the normal modes as presented in Appendix A (see Eq. (A.6)).

The eigenmode approach approximations introduced in Subsec. 2.2.2 are applicable to the circuit of two capacitively coupled transmons. Therefore, in what follows, we only provide the 4th order full RWA explicit analytical formulas for:

- The anharmonicity of mode k due to junction n, with $n = M, H$,

$$\delta_{nk}(\Phi_H^{\text{ext}}) = -\frac{E_{J_n}(\Phi_H^{\text{ext}})}{8} \varphi_{ZPF_k}^4(\Phi_H^{\text{ext}}) (\boldsymbol{P}^{-1})_{nk}^4(\Phi_H^{\text{ext}}). \tag{3.19}$$

- The cross-Kerr coupling between the two modes due to junction n defined as

$$\chi^n(\Phi_H^{\text{ext}}) = -\frac{E_{J_n}(\Phi_H^{\text{ext}})}{4} (\boldsymbol{P}^{-1})_{n1}^2(\Phi_H^{\text{ext}}) (\boldsymbol{P}^{-1})_{n2}^2(\Phi_H^{\text{ext}}) \varphi_{ZPF_1}^2(\Phi_H^{\text{ext}}) \varphi_{ZPF_2}^2(\Phi_H^{\text{ext}}). \tag{3.20}$$

- Finally, omitting the dependency on Φ_H^{ext}, the diagonal Hamiltonian is

$$\hat{H}_{\text{fullRWA}}^{(4)} = \sum_{k=1}^{2} \Omega_k \hat{a}_k^\dagger \hat{a}_k + \frac{\delta_k}{2} \hat{a}_k^\dagger \hat{a}_k^\dagger \hat{a}_k \hat{a}_k + \chi \hat{a}_1^\dagger \hat{a}_1 \hat{a}_2^\dagger \hat{a}_2. \tag{3.21}$$

  The total anharmonicities and cross-Kerr coupling are obtained by summing over the two Josephson junctions n as follows:

$$\delta_k(\Phi_H^{\text{ext}}) = \sum_{n=M}^{H} \delta_{nk}(\Phi_H^{\text{ext}}), \tag{3.22a}$$

$$\chi(\Phi_H^{\text{ext}}) = \sum_{n=M}^{H} \chi^n(\Phi_H^{\text{ext}}). \tag{3.22b}$$

The qubit frequencies are

$$\Omega_k(\Phi_H^{\text{ext}}) = \omega_k(\Phi_H^{\text{ext}}) + \delta_k(\Phi_H^{\text{ext}}) + \frac{1}{2}\chi(\Phi_H^{\text{ext}}). \tag{3.22c}$$

Again, it holds that, with the 4th full RWA approximation, the front coefficient in

$$\chi(\Phi_H^{\text{ext}}(t))\hat{a}_1^\dagger(\Phi_H^{\text{ext}})\hat{a}_1(\Phi_H^{\text{ext}})\hat{a}_2^\dagger(\Phi_H^{\text{ext}})\hat{a}_2(\Phi_H^{\text{ext}}), \tag{3.23}$$

is given by

$$\chi(\Phi_H^{\text{ext}}(t)) = E_{11}(\Phi_H^{\text{ext}}(t)) - E_{01}(\Phi_H^{\text{ext}}(t)) - E_{10}(\Phi_H^{\text{ext}}(t)). \tag{3.24}$$

3.1.3 Validation of the approximations

In this section we evaluate the accuracy of the previous approximations, in particular in the context of a CPHASE simulation. To validate the approximations we focus on the circuit of two capacitively coupled transmons by comparing the results with the exact solution in the Cooper-pair basis. We stress that in the 'exact solution' we cut the number of Cooper-pair states (approximations in Eqs. (2.9) and (2.10)). On the contrary, in the eigenmode approach we work in the basis of harmonic oscillators. Thus, we cut the number of Fock states of the Hilbert space that we consider. As presented in Sec. 2.3, a CPHASE gate is realized by applying an external flux on the qubit with the highest frequency in order to bring the system at the operating point, i.e., at the avoided crossing between the states $|11\rangle$ and $|02\rangle$. For CPHASE simulations there are mainly three quantities which needs to be accurate :

1. The position of the avoided crossing $\varphi_{AC}^{\text{ext}} = (2\pi\Phi_{AC}^{\text{ext}})/\Phi_0$,
2. The size of the gap at the avoided crossing, $\Delta E_{AC} = E_{02}(\varphi_{AC}^{\text{ext}}) - E_{11}(\varphi_{AC}^{\text{ext}})$,
3. And the cross-Kerr coefficient as a function of the external phase $\chi(\varphi_H^{\text{ext}}(t)) = E_{11}(\varphi_H^{\text{ext}}(t)) - E_{01}(\varphi_H^{\text{ext}}(t)) - E_{10}(\varphi_H^{\text{ext}}(t))$.

For concreteness let us take back the high and medium frequency transmon in the surface code architecture [5], whose associated eigenmodes are denoted by Q_H and Q_M respectively. The transmons are chosen to have frequencies $\omega_H/2\pi = 6.7\,\text{GHz}$, $\omega_M/2\pi = 6.0\,\text{GHz}$. In addition, we choose equal shunting capacitances $C_H = C_M = 77.10\,\text{fF}$ and coupling capacitance $C_c = 0.39\,\text{fF}$. From now on, we give the energy levels, the charging energy and the Josephson energy in units of h, i.e. they are expressed in

Hz. Then, this choice gives $E_{c_H} = E_{c_M} = 250\,\text{MHz}$ and $E_I = 2.5\,\text{MHz}$. The Josephson energies (at zero external flux) are $E_{J_H} = 22.45\,\text{GHz}$ and $E_{J_M} = 18.00\,\text{GHz}$.

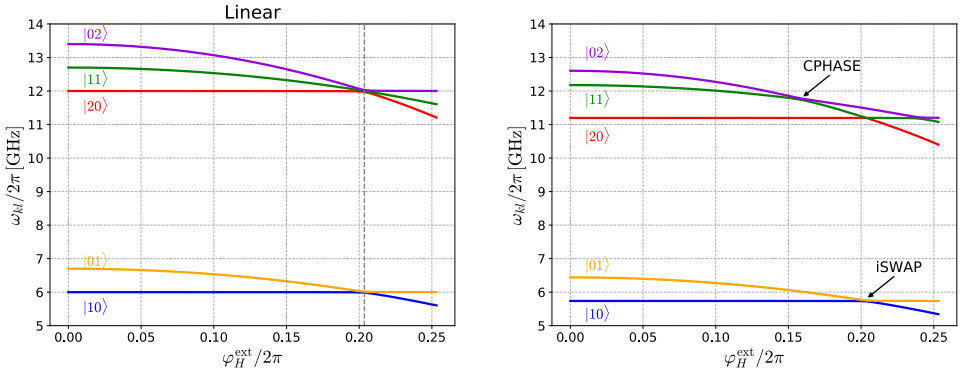

Figure 3.1.2: Energy levels of two transmons capacitively coupled as a function of the external pulse applied to the high frequency qubit Q_H: $\varphi_H^{\text{ext}}/2\pi$. Fig. **a)** corresponds to the energy levels of the linear circuit. There is only one point (grey dashed vertical line) where the avoided crossing happens. On the contrary, the energy levels obtained with the exact solution in Fig. **b)** show a splitting of the avoided crossing into three points. The arrows indicate the points where the avoided crossings associated with the CPHASE and iSWAP gates take place.

The energy levels in Fig. 3.1.2b are obtained from diagonalization of the 'exact solution' in the Cooper-pair basis. In addition to showing the CPHASE avoided crossing, it also indicates the point where the iSWAP gate works, i.e., at the avoided crossing between $|01\rangle$ and $|10\rangle$ [18]. We will now study how the different approximations affect the energy levels, and in particular in which way they influence the optimal implementation of the CPHASE gate.

We begin our analysis by considering the linear Hamiltonian $\hat{H}_{\text{lin}}$ in Eq. (3.18), thus neglecting the non-linearity. The study of the spectrum of $\hat{H}_{\text{lin}}$, although not interesting from a quantum mechanical point of view, allows to understand, by comparison, in which way the addition of the non-linearity to the Hamiltonian modifies the spectrum, allowing for the possible implementation of CPHASE and iSWAP. The energy levels of $\hat{H}_{\text{lin}}$ as a function of the external phase applied to the high frequency qubit is shown in Fig. 3.1.2a. Comparing with Fig. 3.1.2b we make the following observations.

- In the linear case there is only one point (grey dashed vertical line) where the avoided crossing happens, see Fig. 3.1.2a. This point corresponds to the point

where the classical frequencies of the coupled modes are equal. We refer to this point as the classical avoided crossing.

- Considering the first six energy levels the addition of the non-linearity splits the classical avoided crossing into three different avoided crossings as depicted in Fig. 3.1.2b:
  1. the avoided crossing associated with the iSWAP;
  2. the avoided crossing associated with the CPHASE;
  3. a third avoided crossing at higher external fluxes;
- The iSWAP avoided crossing is the one associated with the classical one, and, apart from small corrections, it takes place at the same point.

We do not plot the whole spectrum for each approximation, as the only range where there is a significant change between them is at the CPHASE avoided crossing point. In Fig. 3.1.4 we show how the different approximations recover the energy levels close to the avoided crossing and what position of the avoided crossing they predict. We see that the 6th order approximation perfectly recovers the levels and the position of the avoided crossing, while the one that performs the worst is the 6th order RWA.

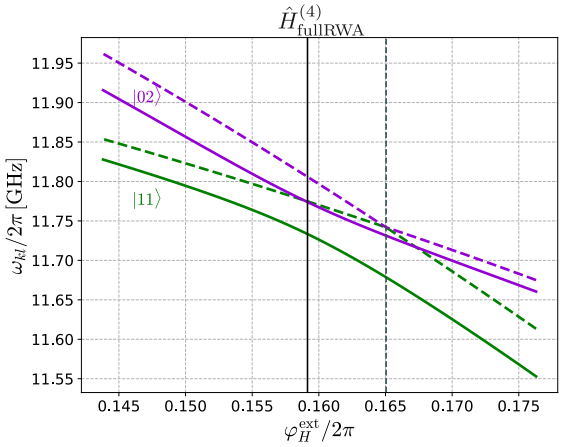

Figure 3.1.3: Comparison of the energy levels of the exact diagonalization (solid lines) with the 4th order full RWA (dashed lines).

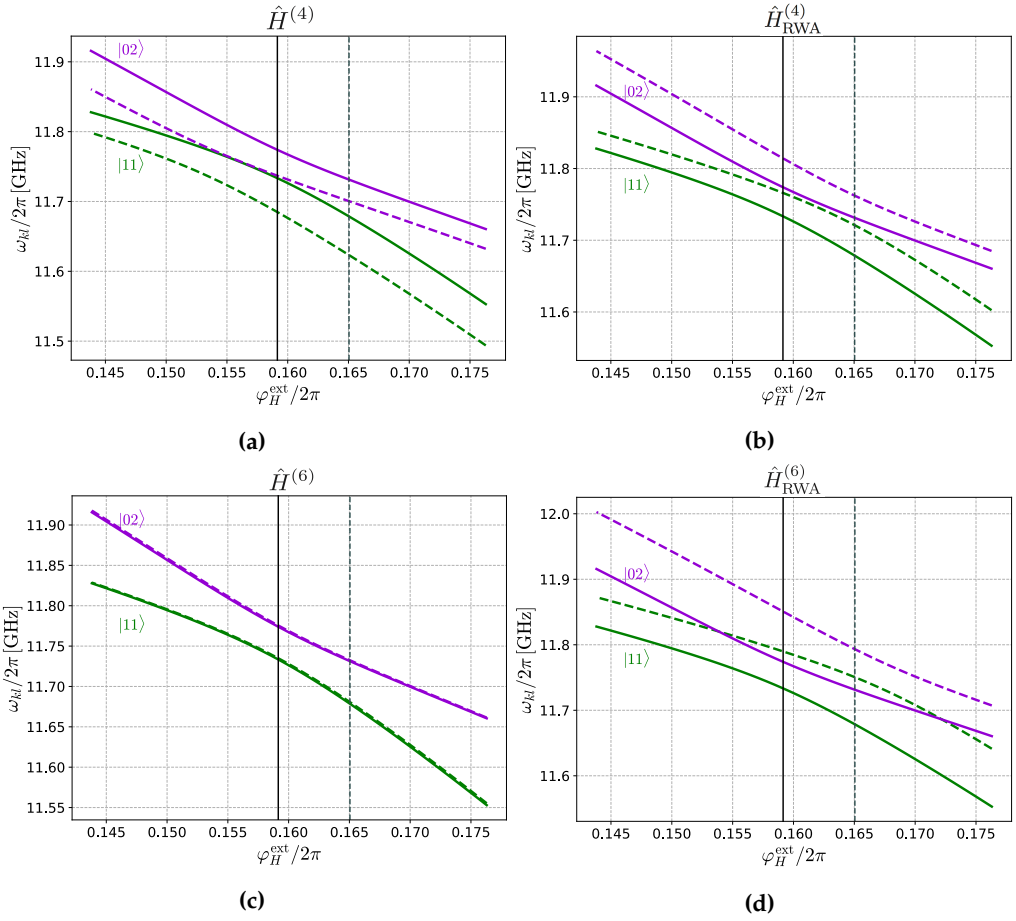

Figure 3.1.4: Comparison of the energy levels of the exact diagonalization (solid lines) with the 4th and 6th order approximations, and their respective RWA (dashed lines). The solid vertical line indicates the position of the exact avoided crossing, while the dashed gray line denotes the position of the avoided crossing predicted by the respective approximation.

In Fig. 3.1.3 we also show the comparison of the exact energy levels with 4th order full RWA approximation. We see that while the position of the avoided crossing is recovered with decent accuracy, there is a striking difference of this approximation in comparison with all those in Fig. 3.1.4. The size of the avoided crossing is completely underestimated. This tells us that the terms neglected in the full RWA approximation, but not in the RWA, play a fundamental role in determining the size of the avoided crossing. An example of a term neglected by the full RWA but not by the RWA approximation is $\hat{a}_1^\dagger(\Phi_H^{\mathrm{ext}})\hat{a}_1(\Phi_H^{\mathrm{ext}})\hat{a}_1(\Phi_H^{\mathrm{ext}})^\dagger\hat{a}_2(\Phi_H^{\mathrm{ext}})$ as it preserves the total number of excitations but not for each mode. We conclude that these terms must be taken into account

when modelling the CPHASE gate if we want an accurate prediction of the size of the avoided crossing. An interesting question is to understand how using the predictions of a certain approximation influences the performances of the CPHASE gate in terms of fidelity.

As discussed in Subsec. 2.3.1, the speed of the CPHASE gate is set by the size of the gap, ΔE_{AC}. Thus, we need to accurately predict the energy gap. We insert in $T_{\text{Rabi}} = 1/\Delta E_{AC}$ the values of ΔE_{AC} in Table 3.1.1, obtained from the spectrum of the different approximations, and estimate the duration of the gate. With each approximation, except with $\hat{H}^{(4)}_{\text{fullRWA}}$, the duration is around $T_{\text{Rabi}} \approx 25$ ns. We conclude that it is possible to simulate a CPHASE gate lasting around 25 ns (with our diabatic pulse), with any of the following approximations : $H^{(6)}$, $\hat{H}^{(6)}_{\text{RWA}}$, $\hat{H}^{(4)}$ and $\hat{H}^{(4)}_{\text{RWA}}$. Only $\hat{H}^{(4)}_{\text{fullRWA}}$ can not be used for realistic simulations of the CPHASE gate as it underestimates the size of the gap at the avoided crossing. By realistic we mean that it should reproduce a gate time of the same magnitude as we would obtain with the exact solution. This result means that, in the eigenmode approach, the coupling which drives the CPHASE gate is captured by the RWA approximations. The difference between the approximations is that the CPHASE gate should be placed at the avoided crossing point predicted by the specific approximation and given in Table 3.1.1. For example, $\hat{H}^{(4)}$ should not perform significantly worse (in terms of fidelity and total duration) if placed at $\varphi^{ext}_{AC}/(2\pi)$= 0.153 rad as $H^{(6)}$ when the latter is placed at $\varphi^{ext}_{AC}/(2\pi) = 0.159$ rad. It would take longer as ΔE_{AC} obtained with the 4th order approximation is lower than the one obtained with the 6th approximation and the leakage might be slightly different, but it would still be possible to simulate a CPHASE gate with this approximation. This is especially true in the case of a diabatic pulse. The exact solution predicts $\varphi^{\text{ext}}_{\text{AC}}/2\pi$ = 0.159 rad. We see in Table 3.1.1 that if an accurate prediction of the position of the avoided crossing is needed then at least the full 6th order is needed. Fig. 3.1.6 provides a comparison between the points at which the CPHASE avoided crossing is predicted by the different approximation.

The 6th order approximation predicts that, at the avoided crossing, the cross-Kerr is worth $|\chi_{AC}|$ = 19.4 MHz and that $\Delta E_{AC}/2$= 20.3 MHz. The exact solution gives $|\chi_{AC}|$ = 20.16 MHz and $\Delta E_{AC}/2$= 20.25 MHz. Thus we observe that the relation

$$\frac{\Delta E_{AC}}{2} \approx |\chi_{AC}| = |E_{11}(\varphi^{\text{ext}}_{AC}) - E_{01}(\varphi^{\text{ext}}_{AC}) - E_{10}(\varphi^{\text{ext}}_{AC})| \tag{3.25}$$

holds up to 4% with the approximation at 6th order and up to 0.4% with the exact solution. We conclude from the relation in Eq. (3.25) that the speed of the CPHASE gate

	Exact	$\hat{H}^{(4)}$	$\hat{H}^{(4)}_{\text{RWA}}$	$\hat{H}^{(4)}_{\text{fullRWA}}$	$\hat{H}^{(6)}$	$\hat{H}^{(6)}_{\text{RWA}}$
$\varphi^{\text{ext}}_{\text{AC}}/2\pi$	0.159	0.153	0.164	0.165	0.159	0.168
ΔE_{AC} [MHz]	40.5	40.5	40.7	1.6	40.6	40.7
$\lvert\chi_{AC}\rvert$ [MHz]	20.16	19.6	19.2	3.0	19.4	20.2
$\lvert\chi_0\rvert$ [MHz]	0.6	0.7	0.5	0.5	0.6	0.5

Table 3.1.1: Predictions of the position and of the magnitude of the CPHASE avoided crossing for the exact diagonalization and the different approximations. The cross-Kerr coefficient at the avoided crossing and at the parking frequency are also reported. They are denoted with χ_{AC} and χ_0, respectively.

realized with a diabatic pulse, is limited by the cross-Kerr at the avoided crossing. We emphasize the definition of χ_{AC} in terms of the energy levels in Eq. (3.25).

At this point it is important to understand in which regime the 4th order full RWA approximation can be used and which parameters it can accurately predict. In architectures such as the ones used for the Surface-7 or Surface-17 [5] we are also interested in determining the value of the ZZ, i.e., cross-Kerr couplings when the qubits are at their parking frequency. In this case nearest-neighbour qubits as Q_H and Q_M would be sufficiently detuned from each other, and so we expect the full RWA to work in this case. This is confirmed in Fig. 3.1.5 which compares the full RWA with exact cross-Kerr between the 2 qubit modes, χ_0, and in the Table 3.1.1. Indeed, at zero flux (qubits far-detuned), the values agree with an accuracy of 10%. While the full RWA approximation fails when the qubits approach resonance, which is visible on the right in Fig. 3.1.5.

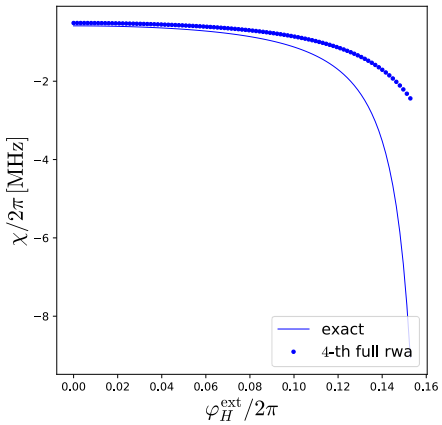

Figure 3.1.5: Comparison of the cross-Kerr for the exact solution and the 4th order full RWA. We observe that the 4th full RWA is a good approximation at parking frequencies, that is when $\varphi_H^{\text{ext}} = 0$. While the 4th full RWA approximation fails when Q_H and Q_M are in resonance, that is at $\varphi_{AC}^{\text{ext}}$.

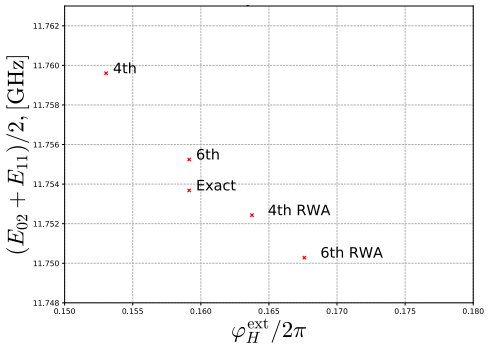

Figure 3.1.6: Comparison between the exact and the different eigenmodes approximations at the CPHASE avoided crossing. The figure plots the values $(E_{02} + E_{11})/2$ at this point.

In summary, the prediction about how long and at which point the CPHASE gate takes place is modified in two ways by the choice of a specific approximation. Indeed, the estimations of the Rabi frequency, ΔE_{AC}, and of the point at which the avoided crossing is predicted, $\varphi_{AC}^{\text{ext}}$, depend on the approximation. We have shown that $\hat{H}^{(6)}$ predicts accurately $\varphi_{AC}^{\text{ext}}$ and the energy level differences, while $\hat{H}^{(4)}_{\text{fullRWA}}$ gives a good estimation of the cross-Kerr (error of 10%), when the qubits are detuned. The latter could thus be used to characterize crosstalk between neighbouring qubits when they are at their parking frequency.

3.1.4 CPHASE model proposal

The ultimate goal is to provide an accurate CPHASE analysis, in presence of ZZ crosstalk in a 'scalable way'. Now, based on the conclusions drawn in the previous section, we make a proposal for a CPHASE model in which the interactions between :

1. The two-interacting qubits is described using the 6th order approximation, $\hat{H}^{(6)}$, or a higher order approximation.

2. The crosstalk from neighbouring qubits would be described in the 4th full RWA approximation, that is with $\hat{H}^{(4)}_{\text{fullRWA}}$. This approximation can be used because the neighbouring qubits are off-resonant with the two qubits involved in the CPHASE gate.

For example, a CPHASE gate between the qubits D_2 and X on the Surface-7 layout could be simulated modeling the crosstalk from neighbouring qubits D_1, D_3, D_4, Z_1 and Z_2 on X and D_2 with $\hat{H}^{(4)}_{\text{fullRWA}}$, as is depicted in Fig. 3.1.7.

The advantage of this approximation is that we have an analytical expression for the diagonal Hamiltonian $\hat{H}^{(4)}_{\text{fullRWA}}$. Thus, no further diagonalization in the Hilbert space is involved. It is in that sense that this approach can be seen as a scalable implementation of ZZ crosstalk.

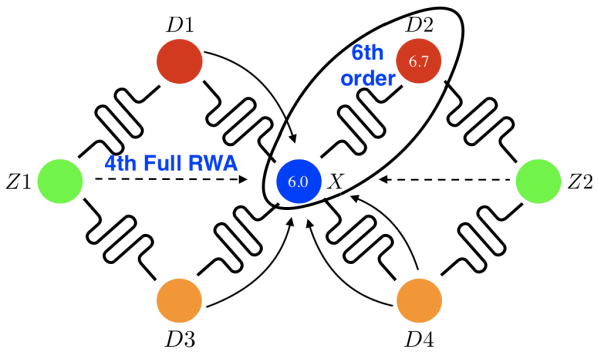

Figure 3.1.7: Example of CPHASE model with crosstalk for Qubit D_2 and X : the interaction between qubits D_2 and X, involved in the CPHASE gate, is simulated using $\hat{H}^{(6)}$. In contrast, the crosstalk from neighbouring qubits D_1, D_3, D_4, Z_1 and Z_2 on X and D_2 which is included using the $\hat{H}^{(4)}_{\text{fullRWA}}$.

3.2 CPHASE simulation without crosstalk

In this subsection, CPHASE gate simulations without crosstalk are carried out using the two capacitively coupled transmons and the eigenmode approach. We compute the fidelities of the CPHASE gate under a diabatic pulse. The theory about the CPHASE gate and the implementation used in these simulations are presented in Sec. 2.3. The Hamiltonian we consider is the 6th order Taylor expansion approximation, $\hat{H}^{(6)}$, introduced in Subsec. 2.2.2. The computational basis is the eigenmode basis at zero flux, $\{ |ij\rangle_0\}$, which results from diagonalizing the linear part of the Hamiltonian when $\Phi_H^{\text{ext}}(t) = 0$, see Subsec. 2.2.1. We also simulate the CPHASE gate using the Hamiltonian of the two capacitively coupled transmons expressed in the Cooper-pair basis in Eq. (3.12). This allows us to compare the performances of the CPHASE gate in terms of fidelity obtained with the eigenmode method and in the Cooper-pair basis.

3.2.1 Simulations

The external pulse that we use is given in Eq. (2.86) and it has three parameters. $\varphi_{AC}^{\text{ext}}$ is the operating point of the CPHASE gate. In what follows, the parameter $\varphi_{AC}^{\text{ext}}$ is fixed at $0.15945 \times 2\pi$ rad. It corresponds to the avoided crossing point between $|11\rangle_0$ and $|02\rangle_0$. τ_R is the time during which the pulse moves from the parking frequency to the operating point $\varphi_{AC}^{\text{ext}}$ (and then backwards), while τ_I is the time during which the pulse stays at $\varphi_{AC}^{\text{ext}}$. In what follows, we focus on the simpler diabatic case since it should capture the main effects of crosstalk. We fix τ_R to 0.6 ns and then maximize the fidelity by varying τ_I. We optimize the pulse with the simulations of the CPHASE gate done with the 6th order approximation in the eigenmode approach, $\hat{H}^{(6)}$. We obtain the optimal parameter $\tau_I = 25.15$ ns. Then, we simulate the CPHASE gate with the Hamiltonian in Eq. (3.12), expressed in the Cooper-pair basis, and we use the pulse with the same parameters as done with $\hat{H}^{(6)}$. The computational basis, in this case, is spanned by the four states with lowest energy obtained by diagonalizing the Hamiltonian in Eq. (3.12). For simplicity, we denote the computational states associated with the 'exact solution' in the Cooper-pair basis with $\{ |ij\rangle\}$ where i and j run from 0 to 1. Finally, we compare the fidelities and conditional phases obtained with the simulations done in the different basis. We point out that optimization was not the main target of this thesis. We include 9 Fock states per qubit in the simulations with $\hat{H}^{(6)}$ and 31 Cooper-pair states in the simulations with the exact solution. The computational states can interact with

these levels during the simulations and are then projected in the computational basis as explained in Subsec. 2.3.2. The simulations in this subsection are diabatic and it is confirmed by plotting $p_{\widetilde{02}}(t)$, i.e. the probability of a state to overlap with the instantaneous eigenstate $|\widetilde{02}\rangle(t)$. As discussed in Subsec. 2.3.1, $p_{\widetilde{02}}(t)$ is an indicator about how much adiabatic or diabatic the evolution is. Diabatic evolutions of the CPHASE gate involve Rabi oscillation in the computational basis between the states $|11\rangle_0$ and $|02\rangle_0$ ($|11\rangle$ and $|02\rangle$ with the exact solution). Figs. 3.2.1 show these Rabi oscillations. In Fig. 3.2.1a we initialize a state in $|11\rangle_0$ and we use $\hat{H}^{(6)}$, while in Fig. 3.2.1b we initialize a state in $|11\rangle$ and we use the Hamiltonian of the exact solution. Fig. 3.2.2 shows the probability $p_{\widetilde{02}}(t)$ corresponding to the evolution in Fig. 3.2.1a. In Table 3.2.1 we compare the fidelities and conditional phases obtained with the 6th order approximation and with the exact solution. In the simulations with the 6th order approximation, we initialize a state sequentially in the four computational states, i.e. $|ij\rangle_0\,(t=0)$, and look at the final probability of leakage out of the computational basis at the end of the gate, i.e. at $T = T_{2Q} + T_{1Q}$. These values are given in Table 3.2.2.

	Fidelity $\mathcal{F}$	ϕ_{2Q} [rad]
$\hat{H}^{(6)}$	0.994	3.12
Exact solution	0.997	3.03

Table 3.2.1: Fidelity and associated conditional phase ϕ_{2Q} obtained with the optimized pulse characterized by the parameters (τ_R, τ_I)=(0.6, 25.15) [ns]. We compare simulations done using the approximate Hamiltonian $\hat{H}^{(6)}$ in the eigenmode approach with simulations done using the Hamiltonian of the 'exact solution' in Eq. (3.12), i.e. done in the Cooper-pair basis. The fidelity in the simulations done with the Cooper-pair basis is 0.3% higher than with $\hat{H}^{(6)}$, though the pulse is optimized with $\hat{H}^{(6)}$. ϕ_{2Q} is closer to π with $\hat{H}^{(6)}$ and is worth 3.12 rad.

In the simulations using the 6th order approximation, the fidelity $\mathcal{F}$ is worth 0.994. The fidelity in the simulations done with the Cooper-pair basis is 0.3% higher and is worth 0.997. The definition of fidelity in Eq. (2.83) takes into account both leakage out of the computational basis at the end of the gate and the phases of the states. Maximizing the fidelity is thus a trade-off between minimizing the leakage, and having ϕ_{2Q} close to π. This explains why the conditional ϕ_{2Q} are not perfectly π. They are worth 3.12 in the simulations using the 6th order approximation and 3.03 in the simulations in the Cooper-pair basis, see Table 3.2.1. The difficulty is to match the parameters of the pulse such that the duration of the Rabi oscillation of the state $|11\rangle_0$ to the level $|02\rangle_0$

and back on $|11\rangle_0$ coincides with the duration it takes to acquire $\phi_{2Q} = \pi$. Otherwise leakage of this state is large. We see in Table 3.2.2 that the probability of leakage of a state initialized in $|11\rangle_0$ is worth 0.006. The probability of leakage for the state $|00\rangle_0$ is of the order of 10^{-4} and for $|10\rangle_0$ and $|01\rangle_0$ they are worth 0.002. The state $|11\rangle_0$ leaks the most out of the computational basis mainly because it is not perfectly back after the Rabi oscillation with $|02\rangle_0$. It may also interact with higher excited states. The important message is that, though further pulse-shape optimization could result in higher fidelity, we have verified that it is possible to accurately model the CPHASE gate using the eigenmode approach. Indeed, the fidelity obtained with the approximate Hamiltonian $\hat{H}^{(6)}$ is up to 0.3% in agreement with the simulations done with the exact solution in the Cooper-pair basis.

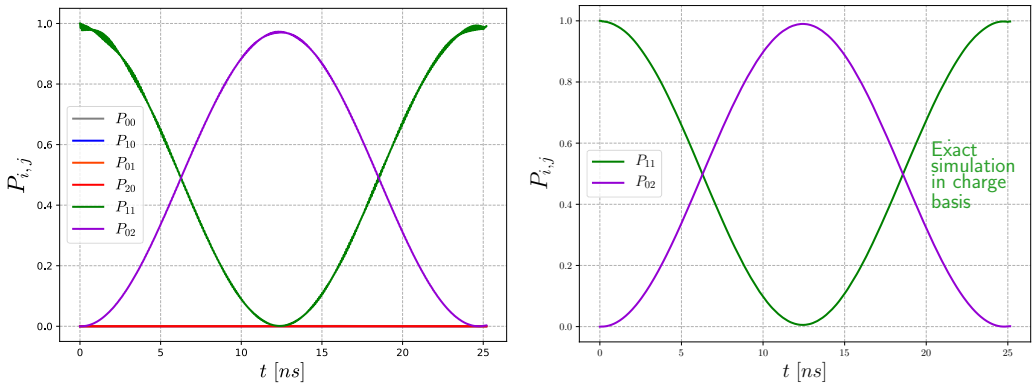

(a) **(b)**

Figure 3.2.1: Fig. **a)** shows the evolution of a state initialized in $|11\rangle_0$ and corresponds to a simulation done with the 6th order approximation from the eigenmode approach. $P_{i,j}(t)$ are the probabilities to be found in the state $|ij\rangle_0$ at time t, defined in Eq. (2.85). Fig. **b)** corresponds to a simulation in the Cooper-pair basis and shows the evolution of the state $|11\rangle$. The states perform Rabi oscillations as we use a diabatic pulse, whose parameters are (τ_r, τ_l)= (0.6, 25.15) ns.

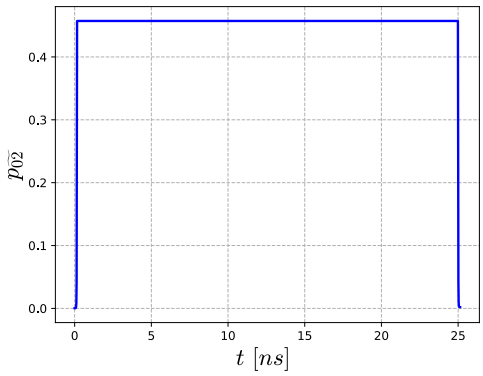

Figure 3.2.2: Probability of a state initialized in $|11\rangle_0$ to overlap with the instantaneous eigenstate $|\widetilde{02}\rangle(t)$. The simulation is done with the Hamiltonian $\hat{H}^{(6)}$. As $p_{\widetilde{02}}(t) \neq 0$ for all t, this means that the simulation is diabatic. This simulation corresponds to the evolution of the state $|11\rangle_0$ in Fig. 3.2.1a.

$p(T)$	$\|00\rangle_0$	$\|10\rangle_0$	$\|01\rangle_0$	$\|11\rangle_0$
(0.6, 25.15) [ns]	5×10^{-4}	0.002	0.002	0.006

Table 3.2.2: Final probabilities of leakage at the end of the gate, i.e. at $T = T_{2Q} + T_{1Q}$, of the four computational states, $|ij\rangle_0\,(t = 0)$. The simulations are done using $\hat{H}^{(6)}$. The state $|11\rangle_0$ leaks the most mainly because it is not perfectly back after the Rabi oscillation with $|02\rangle_0$.

3.3 Analysis of two transmon coupled via a resonator

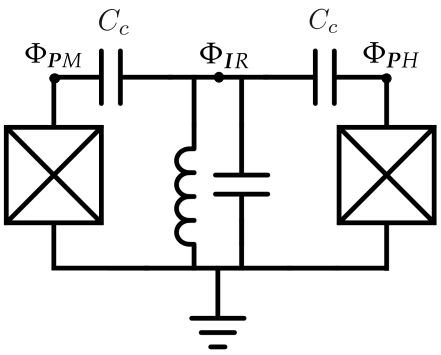

Figure 3.3.1: Two transmons coupled via a far-detuned resonator of bare frequency $\omega_R/(2\pi)$ = 22 GHz. The two fluxes defined across the Josephson junctions of the transmons at the ports are denoted with Φ_{PM} and Φ_{PH}, and the flux across the resonator is denoted with Φ_{IR}. The equal coupling capacitance C_c are worth 3.3 fF.

In this thesis, CPHASE simulations are performed using two transmons which are capacitively coupled, while generally transmons are coupled via bus resonators as in Fig. 3.3.1. Therefore, we want to determine whether the CPHASE simulations with the two capacitively coupled transmons considered in Subsec. 3.2 would be significantly modified for a system of two transmons coupled via a resonator. More precisely, we want to investigate whether we need to take into account the resonator mode in the simulations or not. We do not expect this to be the case, when the resonator frequency is far detuned from those of the qubit modes. In order to confirm this intuition, we perform a test consisting in applying the eigenmode approach to the circuit depicted in Fig. 3.3.1. This circuit has three independent flux variables: the two fluxes defined across the Josephson junctions of the transmons at the ports, Φ_{PM} and Φ_{PH}, and the flux across the resonator, Φ_{IR}. Notice that the flux across the resonator is an internal flux degree of freedom. We apply the eigenmode approach presented in Subsec. 2.2.1, get the matrix $\boldsymbol{P^{-1}}$ of size 3×3 and the three eigenmodes Φ_k with $k = 1, 2, 3$. Then, we build two Hamiltonians using the 6th order approximation, $\hat{H}^{(6)}$, introduced in Subsec. 2.2.2. In the first Hamiltonian we keep the resonator mode Φ_3 after applying the eigenmode approach to the circuit in Fig. 3.3.1. This means that the linear Hamiltonian consists of the two qubit modes and of the resonator mode and that the non-linearities of the transmons are expressed as a linear combination of the three normal modes, i.e. Φ_1, Φ_2 and

Φ_3. In contrast, in the second Hamiltonian the resonator mode Φ_3 is disregarded, i.e., the linear Hamiltonian has two modes and the non-linearities are expressed as a linear combination of the normal modes associated with the two qubit only, i.e. Φ_1 and Φ_2. Subsequently, we compare the lowest energy levels obtained with these two Hamiltonians and analyze whether removing the resonator mode affects significantly the energy levels. More precisely, we compare the energy levels of the following Hamiltonians:

1. The Hamiltonian including the resonator mode, Φ_3:

$$\hat{H}^{(6)}_{\text{with}} = \sum_{k=1}^{3} \omega_k \hat{a}_k^\dagger \hat{a}_k + \sum_{n=M}^{H} E_{Jn} \left(-\frac{\Phi_{Pn}^4}{4!} + \frac{\Phi_{Pn}^6}{6!} \right). \tag{3.26}$$

   Here

$$\Phi_{PM} = (\boldsymbol{P}^{-1})_{00}\Phi_1 + (\boldsymbol{P}^{-1})_{01}\Phi_2 + (\boldsymbol{P}^{-1})_{02}\Phi_3 \tag{3.27}$$

   and

$$\Phi_{PH} = (\boldsymbol{P}^{-1})_{10}\Phi_1 + (\boldsymbol{P}^{-1})_{11}\Phi_2 + (\boldsymbol{P}^{-1})_{12}\Phi_3. \tag{3.28}$$

2. The Hamiltonian without the resonator mode (eigenmode Φ_3 is disregarded):

$$\hat{H}^{(6)}_{\text{without}} = \sum_{k=1}^{2} \omega_k \hat{a}_k^\dagger \hat{a}_k + \sum_{n=M}^{H} E_{J_n} \left(-\frac{\Phi_{Pn}^4}{4!} + \frac{\Phi_{Pn}^6}{6!} \right). \tag{3.29}$$

   Here

$$\Phi_{PM} = (\boldsymbol{P}^{-1})_{00}\Phi_1 + (\boldsymbol{P}^{-1})_{01}\Phi_2 \tag{3.30}$$

   and

$$\Phi_{PH} = (\boldsymbol{P}^{-1})_{10}\Phi_1 + (\boldsymbol{P}^{-1})_{11}\Phi_2. \tag{3.31}$$

We emphasize that in both cases $\boldsymbol{P^{-1}}$ is a 3×3 matrix as it corresponds to the circuit in Fig. 3.3.1, where there are three independent flux variables. For this analysis, the bare frequencies are set to $\omega_M/(2\pi)$ = 5.875 GHz, $\omega_H/(2\pi)$ = 6.253 GHz and $\omega_R/(2\pi)$ = 22 GHz, respectively. The coupling capacitances, indicated in Fig. 3.3.1, are $C_c = 3.3$ fF. The capacitance of the resonator is set to 100 fF and the capacitances of the transmons are worth 77.5 fF. The latter correspond to the charging energy E_{c_t}= -250 MHz. Thus, in a first approximation the anharmonicities are $\delta \approx E_{c_t}$= -250 MHz. Moreover we choose the inductance of the resonator in order that the resonator has an impedance of 50 Ω and a bare frequency of $\omega_R/(2\pi)$ = 22 GHz. We apply the eigenmode approach, and the frequencies of the normal modes associated with the qubits and with the resonator

modes are worth $\omega_1/(2\pi) = 5.75$ GHz, $\omega_2/(2\pi) = 6.12$ GHz and $\omega_3/(2\pi) = 21.34$ GHz, respectively.

	ΔE_{10}	ΔE_{01}	ΔE_{20}	ΔE_{11}	ΔE_{02}	ΔE_{02}	ΔE_{30}
[MHz]	0.11	0.12	0.24	0.23	0.26	0.36	0.36

Table 3.3.1: The 6 lowest energy level differences, $\Delta E_{ij} = E_{ij}^{\text{without}} - E_{ij}^{\text{with}}$, are obtained by taking the difference between the energy levels of the qubits after excluding the resonator mode and the ones obtained keeping the three modes.

We compute the eigenvalues of $\hat{H}^{(6)}_{\text{with}}$ and $\hat{H}^{(6)}_{\text{without}}$ and take the difference between the lowest energy levels, $\Delta E_{ij} = E_{ij}^{\text{without}} - E_{ij}^{\text{with}}$. They are listed in table 3.3.1 and range from 0.11 to 0.36 MHz, thus proving that the energy levels obtained with and without the resonator mode, are in good agreement. This implies that, if the system is excited in a regime involving only the lowest energy levels (applying a signal with frequency in the qubit range for example), the resonator mode is not essential for CPHASE simulations and can be removed. We point out that, more generally, the test suggests that after the applying the classical eigenmode approach on the full system, we can get rid of the resonator modes even before performing canonical quantization, and still recover similar behaviour.

We point out that the elimination of some modes in the normal mode approach does not require any Schrieffer Wolff transformation as the elimination is done at the classical level. If we consider multi-qubit and multi-resonator systems, the elimination done with the eigenmode approach is greatly simplified compared to a Schrieffer-Wolff transformation.

Chapter 4

Three transmon qubits

In this chapter, we start with CPHASE simulations including crosstalk from a spectator qubit with a simplified model in Sec. 4.1. In order to go beyond the limits of this model, CPHASE simulations in presence of crosstalk from a spectator qubit are carried out more realistically in Sec. 4.2 using a system of three capacitively coupled transmons.

4.1 CPHASE simulation with a simplified model

In this section, a simplified model is used to quantify crosstalk effects on the CPHASE gate fidelity. Imagine that a third transmon is capacitively connected to one (or both) of the two capacitively coupled transmons of the circuit introduced in Sec. 3.1. Its main effect is to shift the frequency of its neighbouring qubit depending on its state. We insist on the fact that we simulate the circuit of the two transmons capacitively coupled in Fig. 3.1.1 and artificially add a shift from a potential 'spectator' qubit, Q_S. In order to keep things simple, we assume that Q_S only brings diagonal terms to the linear part of the Hamiltonian. We further asssume that the cross-Kerr from Q_S on Q_M and/or on Q_H, denoted by χ, is independent of the external phase applied to Q_H. In what follows the parameter for χ is kept constant and set to 2.6 MHz.

If Q_S is in the state $|0\rangle$, the linear Hamiltonian in the basis at zero flux is simply:

$$\hat{H}_{s0} = \omega_M \hat{a}_M^\dagger \hat{a}_M + \omega_H \hat{a}_H^\dagger \hat{a}_H. \tag{4.1}$$

When Q_S is in state $|1\rangle$, the frequency of the neighbouring qubit(s), to which it is connected, is shifted by the cross-Kerr value between the modes, χ. Different cases are analyzed. In case a), the spectator qubit is connected to Q_M, leading to the Hamiltonian:

$$\hat{H}_{s1} = (\omega_M - \chi)\hat{a}_M^\dagger \hat{a}_M + \omega_H \hat{a}_H^\dagger \hat{a}_H. \tag{4.2}$$

In case b), it is Q_H which undergoes a spectator-state dependent shift of its frequency. Finally, in case c), both Q_M and Q_H undergo crosstalk from the spectator Q_S. We use the pulse with the same parameters as in the simulations in Sec. 3.2.

The conditional phase ϕ_{2Q} and the fidelity $\mathcal{F}$ associated with these scenarios are compared to case d), in which the spectator induces no crosstalk on the qubits. They can be found in Table 4.1.1. The highest fidelity is obtained when there is crosstalk only on Q_M as ϕ_{2Q} is closer to π than in the other scenarios. We should not conclude that this comes from a physical effect. Most likely this is caused by the fact that $\varphi_{AC}^{\text{ext}}$, obtained by optimization and used in order to define the pulse shape, is slightly shifted compared to the theoretical avoided crossing point. Shifting Q_M could move $\varphi_{AC}^{\text{ext}}$ closer to the theoretical point by chance. At any rate, the results in Table 4.1.1 demonstrate that there is significant CPHASE fidelity variation when crosstalk is present, given a fixed protocol, i.e the choice of the pulse shape. The protocol has to be fixed and $\varphi_{AC}^{\text{ext}}$ or the total pulse duration, for example, can not be adapted to the state of the spectator of course. This suggests to find a way to average the effect of crosstalk. But the right way to take this average remains an open question. We also remark that the reliability of this simplified model of crosstalk should be supported by accurate modelling. For this reason simulations including Q_S in the Hamiltonian $\hat{H}^{(6)}$ are carried out in Sec. 4.2.

ZZ crosstalk on	Fidelity $\mathcal{F}$	ϕ_{2Q} [rad]
Q_M	0.995	3.06
Q_H	0.970	2.96
Q_M and Q_H	0.990	3.01
None	0.994	3.03

Table 4.1.1: Impact on $\mathcal{F}$ and ϕ_{2Q} from a simple model of crosstalk in which a spectator qubit in state $|1\rangle$ affects Q_M and/or Q_H frequency, respectively.

4.2 CPHASE simulation with crosstalk from the spectator

In this section, the impact of crosstalk from the spectator on CPHASE fidelity is analyzed simulating a three transmons capacitively coupled circuit depicted in Fig. 4.2.1a.

A similar analysis is carried out in [13]. The fluxes across the spectator, the high and the medium frequency transmons are denoted with $\{\Phi_{PS}, \Phi_{PH}, \Phi_{PM}\}$ and we work in this basis. The transmons are coupled with an equal capacitance of $C_c = 0.39$ fF. The shunting capacitances of the transmons are equally worth $C_i = 77.1$ fF, with $i = S, H, M$. It corresponds to the charging energy $E_{c_i} = 0.25$ GHz, with $i = S, H, M$. The CPHASE gate is performed between the modes Q_H and Q_M associated with the high and medium transmons, while Q_S, which is associated with the spectator transmon, induces crosstalk. The target frequencies of the transmons are $\omega_S/(2\pi)$= 5.5 GHz, $\omega_H/(2\pi)$= 6.7 GHz and $\omega_M/(2\pi)$= 6.0 GHz. Notice that the spectator frequency is lower than its parking frequency would typically be (see X and Z_2 in Fig. 2.2.1b). In effect, while operating a CPHASE gate between Q_H and Q_M, the frequency of Q_S is tuned down from 6.0 to 5.5 GHz. The Josephson energy of the transmons, E_{J_i} with $i = S, H, M$, are then obtained by matching the target frequencies of the transmons, i.e. $\omega_i/(2\pi) = \sqrt{8E_{c_i}E_{J_i}}$. The Josephson energy of the high frequency qubit is tunable by means of an external flux. The capacitance matrix associated with the circuit in Fig. 4.2.1a is

$$\boldsymbol{C} = \begin{pmatrix} C_S + C_c & -C_c & 0 \\ -C_c & C_H + 2C_c & -C_c \\ 0 & -C_c & C_M + C_c \end{pmatrix}. \tag{4.3}$$

We use the parameters given in Table 4.2.1 and give the numerical values of the exact charging energy matrix:

$$\boldsymbol{E_c} = \frac{e^2}{2}\boldsymbol{C^{-1}} = \begin{pmatrix} 0.24997 & 0.00125 & 6 \times 10^{-6} \\ 0.00125 & 0.24870 & 0.00125 \\ 6 \times 10^{-6} & 0.00125 & 0.24997 \end{pmatrix}. \tag{4.4}$$

Here the coefficients are given in GHz as we assume that the Hamiltonian is in units of h. The inductance energy matrix is

$$\boldsymbol{E_L} = \begin{pmatrix} E_{J_S} & 0 & 0 \\ 0 & E_{J_H}(\Phi_H^{\text{ext}}) & 0 \\ 0 & 0 & E_{J_M} \end{pmatrix}. \tag{4.5}$$

Up to now, the energy matrices are exact. However, in the simulations we used an approximate charging energy matrix

$$\boldsymbol{E}_{\mathbf{sim}} = \begin{pmatrix} E_{c_S} & \frac{E_I}{2} & 0 \\ \frac{E_I}{2} & E_{c_H} & \frac{E_I}{2} \\ 0 & \frac{E_I}{2} & E_{c_M} \end{pmatrix} = \begin{pmatrix} 0.25 & 0.00125 & 0 \\ 0.00125 & 0.25 & 0.00125 \\ 0 & 0.00125 & 0.25 \end{pmatrix}, \tag{4.6}$$

whose entries are at most $\epsilon = 1.3$ MHz away from the ones of the exact charging energy matrix $\boldsymbol{E_c}$ in Eq. (4.4). In fact, we apply no approximation on the off-diagonal terms but only on the diagonal elements. The approximation done on the diagonal elements is equivalent to assuming that the three transmons are uncoupled. We think that it is a reasonable assumption as the coupling between the transmons is weak, i.e. $C_c = 0.39$ fF $\ll C_i = 77.1$ fF, with $i = S, H, M$.

E_I [MHz]	E_{c_i} [GHz]	$\omega_S/(2\pi)$ [GHz]	$\omega_M/(2\pi)$ [GHz]	$\omega_H/(2\pi)$ [GHz]
2.5	0.25	5.5	6.0	6.7

Table 4.2.1: Parameters of the simulations. Here $\omega_i/(2\pi)$ are the target frequencies of the transmons. Note that E_{J_i} with $i = S, H, M$ are set such that $\omega_i/(2\pi) = \sqrt{8E_{c_i}E_{J_i}}$.

We now present the protocol we use in order to characterize the effect of the crosstalk from the spectator qubit. The following steps are taken in order to compute the fidelities. First Q_S is set in state $|0_S\rangle$. The four computational states, $\{\, |0_S0_H0_M\rangle\,, |0_S0_H1_M\rangle, |0_S1_H0_M\rangle\,, |0_S1_H1_M\rangle\,\}$, are initialized and let evolve in order to build the matrix U_{2Q} using Eq. (2.84). The parameters of the pulse are optimized in order to maximize the fidelity defined in Eq. (2.83) and the arrow in Fig. 4.2.1 indicates the CPHASE gate operating point at which the pulse is optimized. With the parameters we use, the pulse is diabatic. In a second step, Q_S is set in state $|1_S\rangle$. We let the four computational states, which are now in the set $\{\, |1_S0_H0_M\rangle\,, |1_S0_H1_M\rangle\,, |1_S1_H0_M\rangle\,, |1_S1_H1_M\rangle\,\}$, evolve under a pulse with the same parameters in order to obtain U_{2Q} and the fidelity $\mathcal{F}$. We emphasize that again simulations are carried out using $\hat{H}^{(6)}$ obtained for the given problem. The optimized parameters of the pulse are found to be $\varphi_{AC}^{\mathrm{ext}}/(2\pi) = 0.159$ rad, τ_r=1 ns and $\tau_I = 24.7$ ns leading to $T = 24.7 + 2 = 26.7$ ns. Additionally, the number of Fock states per qubit is 9.

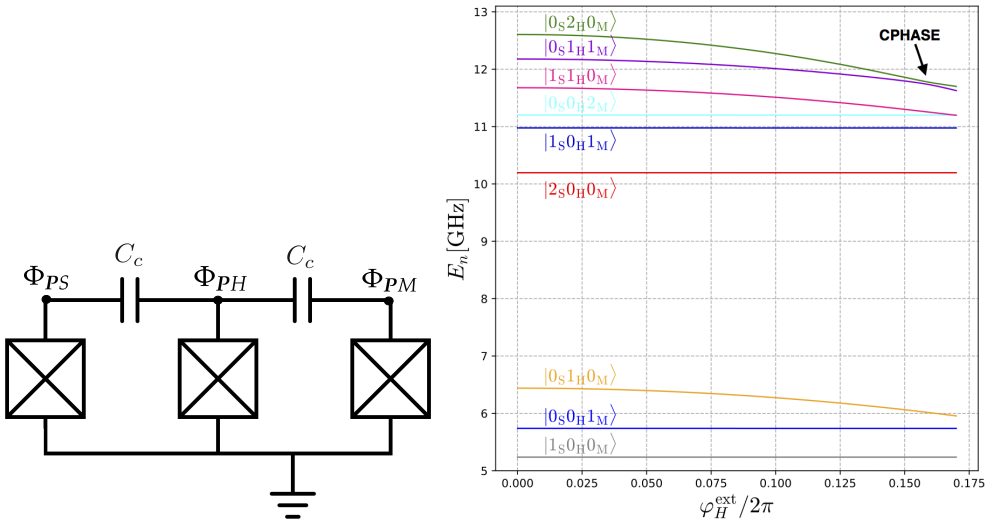

(a) **(b)**

Figure 4.2.1: a) Three transmons capacitively coupled with an equal capacitance C_c. In Fig. **b)** the arrow indicates the CPHASE operating point when the spectator is in $|0_S\rangle$, at which the parameters of the pulse are optimized. However, when Q_S is in $|1_S\rangle$, the energy levels involved in the avoided crossing are $E_{1_S1_H1_M}$ and $E_{1_S2_H0_M}$.

	χ_{HM} [MHz]	χ_{SH} [MHz]	χ_{SM} [MHz]
$\varphi_H^{\text{ext}}/(2\pi) = 0$	-0.584	-0.164	-6.7$\times10^{-4}$
$\varphi_{AC}^{\text{ext}}/(2\pi)$= 0.159	-19.592	-0.394	-9.6$\times10^{-4}$

Table 4.2.2: Cross-Kerr coefficients between each pair of modes at the parking frequency and at the avoided crossing between $|0_S1_H1_M\rangle$ and $|0_S2_H0_M\rangle$ obtained using the 6th order approximation, $\hat{H}^{(6)}$.

We now analyze the cross-Kerr coefficients as they characterize the strength of the crosstalk. The energy levels showed in Fig. 4.2.1b are obtained by diagonalizing the Hamiltonian $\hat{H}^{(6)}$ as a function of the external flux applied on Q_H, i.e. $\Phi_H^{\text{ext}} = \varphi_H^{\text{ext}}\Phi_0/(2\pi)$. We set the lowest energy level to zero, i.e. $E_{0_S0_H0_M}(\Phi_H^{\text{ext}}) = 0$. Then, the cross-Kerr coefficients between the pairs (Q_H, Q_M), (Q_S, Q_H) and (Q_S, Q_M) are respectively given

by:

$$\chi_{HM}(\Phi_H^{\text{ext}}) = E_{0_S 1_H 1_M} - E_{0_S 1_H 0_M} - E_{0_S 0_H 1_M}, \tag{4.7}$$

$$\chi_{SH}(\Phi_H^{\text{ext}}) = E_{1_S 1_H 0_M} - E_{1_S 0_H 0_M} - E_{0_S 1_H 0_M}, \tag{4.8}$$

$$\chi_{SM}(\Phi_H^{\text{ext}}) = E_{1_S 0_H 1_M} - E_{1_S 0_H 0_M} - E_{0_S 0_H 1_M}. \tag{4.9}$$

$$\tag{4.10}$$

The values of the cross-Kerr coefficients at the parking frequency and at the avoided crossing between $|0_S 1_H 1_M\rangle$ and $|0_S 2_H 0_M\rangle$ are given in Table 4.2.2. We see that the cross-Kerr coefficient between Q_M and Q_H increases by a factor of 33 when the external flux moves from the parking frequency to the avoided crossing point. This allows the CPHASE gate to take place. At the avoided crossing, it holds that χ_{HM}^{AC}=-19.59 MHz. It can be compared to χ_{HM}^{AC}=-19.42 MHz which corresponds to the circuits consisting of two transmons capacitively coupled (see Table 3.1.1). We also observe in Table 4.2.2 that, at the avoided, the cross-Kerr coefficient between Q_S and Q_H is 400 times higher than the cross-Kerr coefficient crossing between Q_S and Q_M. They are worth -0.394 MHz and -9.6×10^{-4} MHz, respectively. The latter is clearly negligible. That is because, as can be seen on the circuit in Fig. 4.2.1a, Q_S is a direct neigbor of Q_H and a next-nearest neighbor of Q_M. This tells us that in our circuit, crosstalk induced by neighbouring qubit is not negligible while crosstalk induced by next-nearest neighboor is not a major concern. Importantly, we note that χ_{SH} and χ_{SM} get multiplied by a factor of 2.4 and 1.4, respectively, when the external flux moves from the parking frequency to the avoided crossing point. Thus, crosstalk from the spectator qubit on Q_H and Q_M cannot be considered as independent of the external flux applied on Q_H.

	Fidelity $\mathcal{F}$	ϕ_{2Q} [rad]
Spectator in $\|0_S\rangle$	0.991	2.99
Spectator in $\|1_S\rangle$	0.973	3.12

Table 4.2.3: The impact of the state of the spectator is a 1.9% drop of the CPHASE fidelity. The same parameters of the pulse are used and they are the ones optimized for the case in which Q_S is in $|0_S\rangle$.

$p_{\text{leak}}(t=T)$	$\|00\rangle_0$	$\|10\rangle_0$	$\|01\rangle_0$	$\|11\rangle_0$
$\|0_S\rangle$	0.001	0.004	0.010	0.009
$\|1_S\rangle$	0.012	0.015	0.015	0.022

Table 4.2.4: Comparison of the final leakage probability at the end of the gate of a state initialized sequentially in the four computational states, $|ij\rangle_0\,(t=0)$, when the spectator is in $|0_S\rangle$ or in $|1_S\rangle$.

As indicated in Table 4.2.3, crosstalk from Q_S induces a fidelity drop of 1.9%. Indeed the fidelities are $\mathcal{F}$= 0.991 and 0.973, respectively. This proves that crosstalk induced by neighbouring qubits has a non-negligible effect on the CPHASE gate. As discussed in the following analysis, the reduction in fidelity when the spectator is in $|1_S\rangle$ is dominated by the leakage out of the computational basis. The conditional phase ϕ_{2Q} is 4% higher when the spectator is in $|1_S\rangle$ and is closer to π. The evolution of the computational states are plotted in Figs. 4.2.2 and Figs. 4.2.3, when the spectator is in $|0_S\rangle$ and in $|1_S\rangle$, respectively. Notice the small oscillations in Fig. 4.2.3 around the mean probabilities. The Rabi oscillation performed by $|11\rangle_0$ is more complete when the spectator is in $|0_S\rangle$ than in $|1_S\rangle$ as the probability to be found in the state $|02\rangle_0$ at $t = T_{2Q}/2$ are given by $p_{02}(T_{2Q}/2)$ = 0.967 when the spectator is in $|0_S\rangle$ and $p_{02}(T_{2Q}/2)$ =0.958 when the spectator is in $|1_S\rangle$. It is interesting to compare these values with the total probability of leakage out of the computational basis at $t = T_{2Q}/2$ of a state initialized in $|11\rangle_0$. When Q_S is in $|0_S\rangle$ it is worth 0.994 and is 0.998 when Q_S is in $|1_S\rangle$. Thus, when the spectator is in $|1_S\rangle$, a state initialized in $|11\rangle_0$ leaks overall more out of the computational basis but less on $|02\rangle_0$. In Table 4.2.4, it can be observed that the final leakage probabilities at the end of the gate, i.e. $T = T_{2Q} + T_{1Q}$, of a state initialized sequentially in the four computational states, $|ij\rangle_0\,(t=0)$, are higher when the spectator is in $|1_S\rangle$ than in $|0_S\rangle$. This is caused by the fact that higher excited states interact more with other higher levels, thus causing more leakage. For example, when the spectator is in $|1_S\rangle$ the computational state $|1_S1_H0_M\rangle$, which has two excitations, can potentially leaks into other states having two excitations like $|2_S0_H0_M\rangle$, $|0_S0_H2_M\rangle$ and $|0_S2_H0_M\rangle$. These interactions also explain why we see the oscillations in Figs. 4.2.3a, 4.2.3b and 4.2.3c which are not observed in Figs. 4.2.2a, 4.2.3b and 4.2.3c. Additionally, it should be kept in mind that $\varphi_{AC}^{\text{ext}}$ is the value corresponding to the avoided crossing between the states $|0_S1_H1_M\rangle$ and $|0_S2_H0_M\rangle$ which might not coincide with the avoided crossing between the states $|1_S1_H1_M\rangle$ and $|1_S2_H0_M\rangle$. This also contributes to a higher fidelity when the

spectator is in $|0_S\rangle$.

As a conclusion, this analysis has demonstrated that crosstalk induced by neighbouring qubits has a non-negligible effect on the CPHASE fidelity. In our simulations, a spectator qubit, which is a direct neighbor of the high frequency qubit in the CPHASE gate, induces a drop of fidelity of 1.9%.

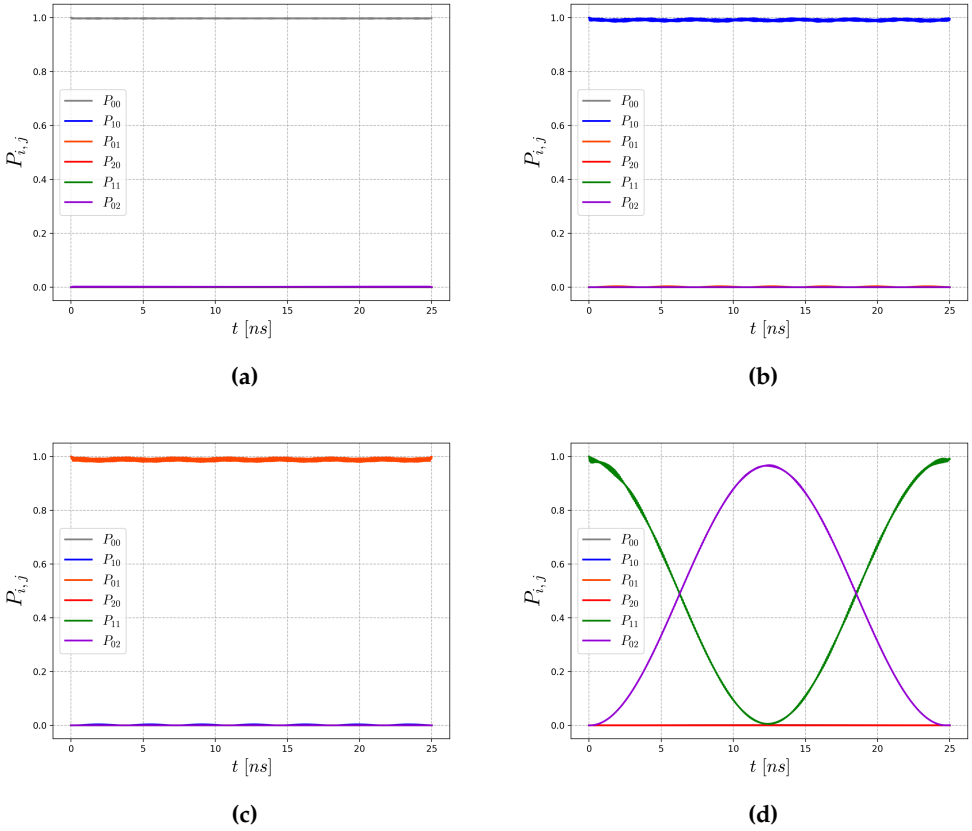

Figure 4.2.2: Evolution of states initialized sequentially in $|0_S 0_H 0_M\rangle$, $|0_S 0_H 1_M\rangle$, $|0_S 1_H 0_M\rangle$ and $|0_S 1_H 1_M\rangle$ respectively. $P_{i,j}(t)$ are the probabilities to be found in the state $|ij\rangle_0$ at time t, defined in Eq. (2.85).

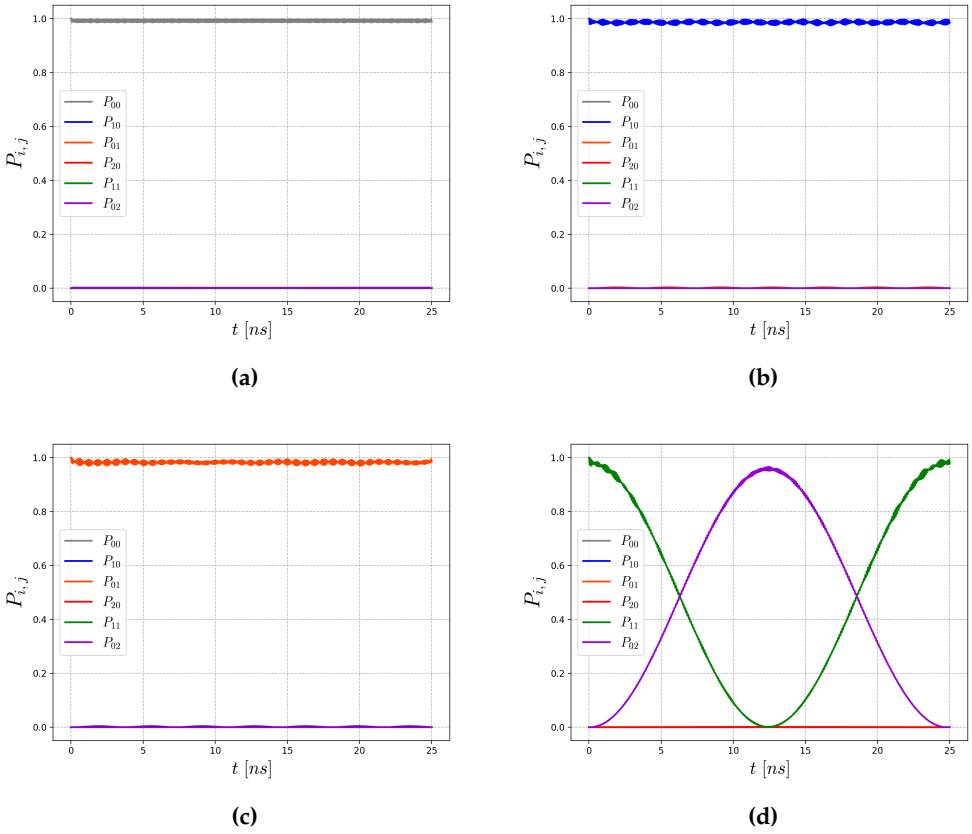

Figure 4.2.3: Evolution of states initialized sequentially in $|1_S 0_H 0_M\rangle$, $|1_S 0_H 1_M\rangle$, $|1_S 1_H 0_M\rangle$ and $|1_S 1_H 1_M\rangle$ respectively. $P_{i,j}(t)$ are the probabilities to be found in the state $|ij\rangle_0$ at time t, defined in Eq. (2.85).

Chapter 5

Conclusion and Outlook

In this thesis, we have used the eigenmode approach, whose purpose is to study circuits consisting of capacitances, inductances and Josephson junctions, which are the building blocks for transmon qubits. The eigenmode approach identifies the normal modes of the linear part of the circuit as the qubit modes and treats the non-linearity of the Josephson junctions as a coupling, to which approximations can be applied. We have verified that the eigenmode approach can be used to accurately model the CPHASE gate and that the coupling, which drives the CPHASE gate in the eigenmode approach, is captured by the RWA approximations applied to the normal modes $\hat{a}_k(\Phi_H^{\text{ext}}(t))$. The approximations, however, predict different external flux points, Φ_{AC}^{ext}, where they expect the avoided crossing to occur. Secondly, due to the fact that the so-called full rotating-wave approximation at 4th order estimates the cross-Kerr coefficients between detuned qubits within 10% error, this approximation could be used to describe crosstalk effects from neighbors on the two qubits involved in the CPHASE gate. The advantage of including crosstalk in CPHASE simulations with $\hat{H}^{(4)}_{\text{fullRWA}}$ is that this approximation gives analytical expression for the cross-Kerr coefficients. Then, we confirmed that in CPHASE simulations between two transmons coupled via a resonator we can get rid of the resonator normal mode in the eigenmode approach. The tests carried out suggest that, more generally, after applying the classical eigenmode approach on a full system, one can get rid of the resonator mode even before performing canonical quantization, and still recover the same behaviour.

CPHASE simulations without crosstalk are implemented using the two capacitively coupled transmons and the eigenmode approximation $\hat{H}^{(6)}$. We have focused on diabatic pulse. The highest fidelity is worth 0.994 in the problem we studied. Moreover

we compared the fidelity obtained with $\hat{H}^{(6)}$ with the fidelity obtained with the Hamiltonian of the two capacitively coupled transmons expressed in the Cooper-pair basis given in Eq. (3.12). The fidelities agree up to 0.3%. Finally, CPHASE simulations in presence of crosstalk from a spectator transmon, using a system of three capacitively coupled transmons, reveal that ***the impact of crosstalk from the spectator on the CPHASE gate is a drop of fidelity of of 1.9%***. We optimize the fidelity for the case in which the spectator qubit is in state $|0_S\rangle$ and then apply the same pulse to the case in which the spectator is state $|1_S\rangle$. The final probabilities of leakage out of the computational basis are higher when the spectator qubit is in state $|1_S\rangle$. As a conclusion, this analysis has demonstrated that crosstalk induced by neighbouring qubits has a non-negligible effect on the CPHASE fidelity. The fabrication of a quantum processor layout with specific parameters (charging and Josephson energy essentially : E_c and E_J) is a tough task to realize. We would like to emphasize that the derivations made in Sec. 2.2 provide *predictive values useful for layout design*. In particular, the eigenmode approach describes how single transmon parameters are modified when they are interconnected on the layout. It is useful, for example, to be able to predict the cross-Kerr coefficients (which give rise to residual crosstalk) resulting from a specific choice of parameters of transmons for a layout. Different targeted designs can be tested and compared with the eigenmode method before the fabrication. However, we must bear in mind that the targeted parameters are shifted due to fabrication processes and that these effects cannot be theoretically predicted. A limitation of this thesis is that the circuits we considered contained a small amount of transmons while crosstalk comes to light when the number of qubits is scaled up. Indeed, scalability is not tackled in this thesis. Moreover, we decided not to focus on the optimization of the pulse and we limited ourselves to diabatic pulses. In order to suppress qubit crosstalk, while still achieving fast two-qubits gates, a promising option is to use the symmetry of superconducting architecture chips, similarly to what is done in [37]. Indeed, the suppression of ZZ crosstalk in a two-qubit, two-coupler superconducting circuit is reported when two necessary criteria are met. In essence, the frequency of a tunable coupler is adjusted such that the cross-Kerr interaction from each coupler (from each path) destructively interfere. Another approach is discussed in [38] where they combined transmon qubits, which have negative anharmonicity, with a capacitively shunted flux qubit, which on the opposite have positive anharmonicity, in order to cancel the ZZ crosstalk interaction at specific detunings between the qubits. As a closing message, we point out that the approach developed in this thesis is also suitable for studying these alternative solutions.

Bibliography

[1] I. M. Georgescu, S. Ashhab, and F. Nori, "Quantum simulation," *Reviews of Modern Physics*, vol. 86, no. 1, p. 153, 2014.

[2] M. A. Nielsen and I. Chuang, "Quantum computation and quantum information," 2002.

[3] D. P. DiVincenzo, "The physical implementation of quantum computation," *Fortschritte der Physik: Progress of Physics*, vol. 48, no. 9-11, pp. 771–783, 2000.

[4] A. Blais, R.-S. Huang, A. Wallraff, S. M. Girvin, and R. J. Schoelkopf, "Cavity quantum electrodynamics for superconducting electrical circuits: An architecture for quantum computation," *Physical Review A*, vol. 69, no. 6, p. 062320, 2004.

[5] R. Versluis, S. Poletto, N. Khammassi, B. Tarasinski, N. Haider, D. J. Michalak, A. Bruno, K. Bertels, and L. DiCarlo, "Scalable quantum circuit and control for a superconducting surface code," *Physical Review Applied*, vol. 8, no. 3, p. 034021, 2017.

[6] J. Koch, M. Y. Terri, J. Gambetta, A. A. Houck, D. Schuster, J. Majer, A. Blais, M. H. Devoret, S. M. Girvin, and R. J. Schoelkopf, "Charge-insensitive qubit design derived from the Cooper-pair box," *Physical Review A*, vol. 76, no. 4, p. 042319, 2007.

[7] A. G. Fowler, M. Mariantoni, J. M. Martinis, and A. N. Cleland, "Surface codes: Towards practical large-scale quantum computation," *Physical Review A*, vol. 86, no. 3, p. 032324, 2012.

[8] S. B. Bravyi and A. Y. Kitaev, "Quantum codes on a lattice with boundary," *arXiv preprint quant-ph/9811052*, 1998.

[9] E. Dennis, A. Kitaev, A. Landahl, and J. Preskill, "Topological quantum memory," *Journal of Mathematical Physics*, vol. 43, no. 9, pp. 4452–4505, 2002.

[10] J. C. Garcia-Escartin and P. Chamorro-Posada, "Equivalent quantum circuits," *arXiv preprint arXiv:1110.2998*, 2011.

[11] L. DiCarlo, J. M. Chow, J. M. Gambetta, L. S. Bishop, B. R. Johnson, D. Schuster, J. Majer, A. Blais, L. Frunzio, S. Girvin, *et al.*, "Demonstration of two-qubit algorithms with a superconducting quantum processor," *Nature*, vol. 460, no. 7252, pp. 240–244, 2009.

[12] P. Mundada, G. Zhang, T. Hazard, and A. Houck, "Suppression of qubit crosstalk in a tunable coupling superconducting circuit," *Physical Review Applied*, vol. 12, no. 5, p. 054023, 2019.

[13] S. Krinner, S. Lazar, A. Remm, C. Andersen, N. Lacroix, G. Norris, C. Hellings, M. Gabureac, C. Eichler, and A. Wallraff, "Benchmarking coherent errors in controlled-phase gates due to spectator qubits," *arXiv*, pp. arXiv–2005, 2020.

[14] S. E. Nigg, H. Paik, B. Vlastakis, G. Kirchmair, S. Shankar, L. Frunzio, M. Devoret, R. Schoelkopf, and S. Girvin, "Black-box superconducting circuit quantization," *Physical Review Letters*, vol. 108, no. 24, p. 240502, 2012.

[15] M. Gely and G. Steele, "Qucat: superconducting quantum circuit analyzer tool in python," *Bulletin of the American Physical Society*, 2020.

[16] U. Vool and M. Devoret, "Introduction to quantum electromagnetic circuits," *International Journal of Circuit Theory and Applications*, vol. 45, no. 7, pp. 897–934, 2017.

[17] G. Wendin, "Quantum information processing with superconducting circuits: a review," *Reports on Progress in Physics*, vol. 80, no. 10, p. 106001, 2017.

[18] P. Krantz, M. Kjaergaard, F. Yan, T. P. Orlando, S. Gustavsson, and W. D. Oliver, "A quantum engineer's guide to superconducting qubits," *Applied Physics Reviews*, vol. 6, no. 2, p. 021318, 2019.

[19] L. S. Bishop, "Circuit quantum electrodynamics," *PhDT*, 2010.

[20] W. Smith, A. Kou, X. Xiao, U. Vool, and M. Devoret, "Superconducting circuit protected by two-Cooper-pair tunneling," *npj Quantum Information*, vol. 6, no. 1, pp. 1–9, 2020.

[21] M. D. Reed, *Entanglement and Quantum Error Correction with Superconducting Qubits*. PhD thesis, Yale University, 2014.

[22] I. Pietikäinen, J. Tuorila, D. Golubev, and G. Paraoanu, "Photon blockade and the quantum-to-classical transition in the driven-dissipative josephson pendulum coupled to a resonator," *Physical Review A*, vol. 99, no. 6, p. 063828, 2019.

[23] J. Gambetta, A. A. Houck, and A. Blais, "Superconducting qubit with purcell protection and tunable coupling," *Physical review letters*, vol. 106, no. 3, p. 030502, 2011.

[24] S. M. Girvin, "Superconducting qubits and circuits: Artificial atoms coupled to microwave photons," *Lectures delivered at Ecole d'Eté Les Houches*, 2011.

[25] D. M. Pozar, *Microwave Engineering 3e*. Wiley, 2006.

[26] J. Gnanadhas, "Microwave circuit analysis of multi transmon qubit system," *Msc thesis, Delft University*, 2018.

[27] A. Ciani, private communication.

[28] A. E. Ruehli, "Inductance calculations in a complex integrated circuit environment," *IBM Journal of Research and Development*, vol. 16, no. 5, pp. 470–481, 1972.

[29] F. Solgun, D. P. DiVincenzo, and J. M. Gambetta, "Simple impedance response formulas for the dispersive interaction rates in the effective Hamiltonians of low anharmonicity superconducting qubits," *IEEE Transactions on Microwave Theory and Techniques*, vol. 67, no. 3, pp. 928–948, 2019.

[30] F. W. Strauch, P. R. Johnson, A. J. Dragt, C. Lobb, J. Anderson, and F. Wellstood, "Quantum logic gates for coupled superconducting phase qubits," *Physical review letters*, vol. 91, no. 16, p. 167005, 2003.

[31] M. A. Rol, F. Battistel, F. K. Malinowski, C. C. Bultink, B. M. Tarasinski, R. Vollmer, N. Haider, N. Muthusubramanian, A. Bruno, B. M. Terhal, and L. DiCarlo, "Fast, high-fidelity conditional-phase gate exploiting leakage interference in weakly anharmonic superconducting qubits," *Phys. Rev. Lett.*, vol. 123, p. 120502, Sep 2019.

[32] D. P. DiVincenzo, *Quantum Information Processing: Lecture Notes of the 44th IFF Spring School 2013*. Forschungszentrum, 2013.

[33] J. M. Martinis and M. R. Geller, "Fast adiabatic qubit gates using only σ_z control," *Physical Review A*, vol. 90, no. 2, p. 022307, 2014.

[34] D. Comparat, "General conditions for quantum adiabatic evolution," *Physical Review A*, vol. 80, no. 1, p. 012106, 2009.

[35] D. J. Egger and F. K. Wilhelm, "Optimized controlled-z gates for two superconducting qubits coupled through a resonator," *Superconductor Science and Technology*, vol. 27, no. 1, p. 014001, 2013.

[36] M. Abdelhafez, B. Baker, A. Gyenis, P. Mundada, A. A. Houck, D. Schuster, and J. Koch, "Universal gates for protected superconducting qubits using optimal control," *Physical Review A*, vol. 101, no. 2, p. 022321, 2020.

[37] P. Mundada, G. Zhang, and A. Houck, "Suppression of qubit crosstalk in a tunable coupling superconducting circuit device," *APS*, vol. 2018, pp. P33–008, 2018.

[38] J. Ku, X. Xu, M. Brink, D. C. McKay, J. B. Hertzberg, M. H. Ansari, and B. Plourde, "Suppression of unwanted *zz* interactions in a hybrid two-qubit system," *arXiv preprint arXiv:2003.02775*, 2020.

[39] R. A. Horn and C. R. Johnson, *Matrix analysis*. Cambridge university press, 2012.

[40] J. A. Russer and P. Russer, "Lagrangian and Hamiltonian formulations for classical and quantum circuits," *IFAC Proceedings Volumes*, vol. 45, no. 2, pp. 439–444, 2012.

[41] K. C. Smith, K. Smith, and R. Alley, *Electrical circuits: an introduction*. Cambridge University Press, 1992.

Appendices

Appendix A

The simulations are done in the eigenmode basis at zero flux, i.e. $\{\,|ij\rangle_0\}$. We simulate the circuit of the two transmons capacitively coupled presented in Subsec. 3.1. The Hamiltonian implemented is derived with the eigenmode approach keeping the non-linearity up to 6th order, $\hat{H}^{(6)}$, without applying the RWA approximation, see Sec. 2.2.2. We work in the Schrödinger picture with a time-dependant Hamiltonian. We denote the Hamiltonian at zero flux with

$$\hat{H}_0 = \omega_1(\Phi_H^{\text{ext}}=0)\hat{a}_1^\dagger(\Phi_H^{\text{ext}}=0)\hat{a}_1(\Phi_H^{\text{ext}}=0) + \omega_2(\Phi_H^{\text{ext}}=0)\hat{a}_2^\dagger(\Phi_H^{\text{ext}}=0)\hat{a}_2(\Phi_H^{\text{ext}}=0), \\ -E_{J1}\left[\frac{1}{4!}\hat{\varphi}_{P1}^4 - \frac{1}{6!}\hat{\varphi}_{P1}^6\right] - E_{J2}(\Phi_H^{\text{ext}}=0)\left[\frac{1}{4!}\hat{\varphi}_{P2}^4 - \frac{1}{6!}\hat{\varphi}_{P2}^6\right]. \tag{A.1}$$

Here $\omega_i(\Phi_H^{\text{ext}}=0)/(2\pi)$ and $\hat{a}_i(\Phi_H^{\text{ext}}=0)$ with $i=1,2$ are, respectively, the frequencies and the annihilation operators of the normal modes at $\Phi_H^{\text{ext}}=0$. We express the phases at the ports, in terms of the normal modes at zero external flux as follows:

$$\hat{\varphi}_{P1} = (\boldsymbol{P^{-1}})_{11}(\Phi_H^{\text{ext}}=0)\hat{\varphi}_1(\Phi_H^{\text{ext}}=0) + (\boldsymbol{P^{-1}})_{12}(\Phi_H^{\text{ext}}=0)\hat{\varphi}_2(\Phi_H^{\text{ext}}=0) \tag{A.2}$$

and

$$\hat{\varphi}_{P2} = (\boldsymbol{P^{-1}})_{21}(\Phi_H^{\text{ext}}=0)\hat{\varphi}_1(\Phi_H^{\text{ext}}=0) + (\boldsymbol{P^{-1}})_{22}(\Phi_H^{\text{ext}}=0)\hat{\varphi}_2(\Phi_H^{\text{ext}}=0). \tag{A.3}$$

When $\Phi_H^{\text{ext}}(t)$ is tuned, the normal modes of the linear part of the Hamiltonian are modified. We can add the 'perturbative' Hamiltonian due to the tuning of the flux on top of $\hat{H}_0$, at time t, as follows:

$$\hat{H}(\Phi_H^{\text{ext}}(t)) = \hat{H}_0 + \hat{H}_{\text{pert}}(\Phi_H^{\text{ext}}(t)). \tag{A.4}$$

Here

$$\hat{H}_{\text{pert}}(\Phi_H^{\text{ext}}(t)) = \Big(E_{J2}(\Phi_H^{\text{ext}}(t)) - E_{J2}(\Phi_H^{\text{ext}}=0)\Big)\left[\frac{1}{2}\hat{\varphi}_{P2}^2 - \frac{1}{4!}\hat{\varphi}_{P2}^4 + \frac{1}{6!}\hat{\varphi}_{P2}^6)\right]. \tag{A.5}$$

Note that the phase at port 2, $\hat{\varphi}_{P2}(\Phi_H^{\text{ext}}=0)$, is still expressed in terms of the normal modes at zero external flux as in Eq. (A.2). A particular attention should be paid to the linear term, $\hat{\varphi}_{P2}^2$, in Eq. (A.5). In the basis $\{\,|ij\rangle_0\}$, it causes the additional linear coupling:

$$J_2^{\text{lin}}(\Phi_H^{\text{ext}}(t))\Big(\hat{a}_1(\Phi_H^{\text{ext}}=0) + \hat{a}_1^\dagger(\Phi_H^{\text{ext}}=0)\Big)\Big(\hat{a}_2(\Phi_H^{\text{ext}}=0) + \hat{a}_2^\dagger(\Phi_H^{\text{ext}}=0)\Big). \tag{A.6}$$

In the following expression, we omit the dependency of $\boldsymbol{P^{-1}}$ on the external flux and evaluate the matrix at $\Phi_H^{\text{ext}} = 0$. Then, the coupling coefficient is given by:

$$J_2^{\text{lin}}(\Phi_H^{\text{ext}}(t)) = \left(E_{J2}(\Phi_H^{\text{ext}}(t)) - E_{J2}(0) \right) \left[(\boldsymbol{P^{-1}})_{21} (\boldsymbol{P^{-1}})_{22} \varphi_{ZPF1}(0) \varphi_{ZPF2}(0) \right]. \quad \text{(A.7)}$$

Moreover, the linear term in Eq. (A.5) modifies the frequencies, $\omega_i(\Phi_H^{\text{ext}}(t))$ in Eq. (A.1). The basic principle of the CPHASE gate can be understood with a two-level model with the states $|11\rangle_0$ and $|02\rangle_0$ between which the avoided crossing of interest takes place [33]. Therefore we evaluate the Hamiltonian and look at the coefficient:

$$\langle 02|_0 \, \hat{H}(\Phi_H^{\text{ext}}(t)) \, |11\rangle_0 \, . \quad \text{(A.8)}$$

This off-diagonal coefficient involves the exchange of one excitation from mode 1 to mode 2, i.e. the operation $\hat{a}_1(\Phi_H^{\text{ext}} = 0)\hat{a}_2^\dagger(\Phi_H^{\text{ext}} = 0)$ which can be combined with an equal number of creation as annihilation operators for each mode. Clearly the linear coupling in Eq. (A.6) contributes to $\langle 02|_0 \, \hat{H}(\Phi_H^{\text{ext}}(t)) \, |11\rangle_0$. In addition there is the contribution from the non-linearity, whose strength is modified by the prefactor $E_{J2}(\Phi_H^{\text{ext}}(t))$ in Eq. (A.5). We inspect now what are the terms brought by the non-linearity at different order:

- The non-linearity at 4th order involves off-diagonal contribution. For example:

$$\langle 02|_0 \, \hat{a}_1^\dagger(0)\hat{a}_1(0)\hat{a}_1(0)\hat{a}_2^\dagger(0) \, |11\rangle_0 \neq 0. \quad \text{(A.9)}$$

- The non-linearity at 6th order involves additional off-diagonal contribution. For example:

$$\langle 02|_0 \, \hat{a}_1^\dagger(0)\hat{a}_1(0)\hat{a}_2^\dagger(0)\hat{a}_2(0)\hat{a}_1(0)\hat{a}_2^\dagger(0) \, |11\rangle_0 \neq 0. \quad \text{(A.10)}$$

These terms are responsible for the size of the energy gap at the avoided crossing, ΔE_{AC}. As a conclusion, the coupling which allows a CPHASE gate to take place by inducing an avoided crossing between the states $|11\rangle_0$ and $|02\rangle_0$, comes both from the linear coupling in Eq. (A.6) and from the increase of the strength of the non-linearity in Eq. (A.5). This claim holds in the eigenmode at zero flux.

We would like to add two final remarks. Firstly, it is important to notice that we can, alternatively, apply the eigenmode approach at each value of $\Phi_H^{\text{ext}}(t)$ and look at the coupling from the perspective of the changing normal modes associated with the

operators $\hat{a}_k(\Phi_H^{\text{ext}}(t))$. Then, there is no linear coupling between the changing modes $\hat{a}_k(\Phi_H^{\text{ext}}(t))$ as in Eq. (A.6). The coupling is purely non-linear.

The second remark is about a conclusion we did in Subsec. 3.1.3. We claimed that we should keep the RWA terms in order to accurately reproduce the size of the avoided crossing, ΔE_{AC}, and thus the cross-Kerr at the avoided crossing, χ_{AC}. Importantly, there, the RWA approximations are applied to the modes associated with the operators $\hat{a}_k(\Phi_H^{\text{ext}}(t))$ and not to the normal at zero flux, $\hat{a}_k(\Phi_H^{\text{ext}} = 0)$. Otherwise the RWA approximations applied to the linear term $\hat{\varphi}_{P2}^2$ in Eq. (A.5) might neglect some terms which plays a crucial role in driving the CPHASE gate.

Appendix B

In this appendix we show that the matrix $\boldsymbol{C^{-1}L^{-1}}$ is diagonalizable and has positive and real eigenvalues. Moreover, we prove that the effective capacitance matrix $\boldsymbol{C}_{\text{eff}}$, defined in Eq. (2.39), is always diagonal with real and positive eigenvalues. In what follows, we apply the definitions and theorems provided in [39] at pages 485 and 486 on the specific problem presented in Subsec. 2.2.1.

Definition 1. *A square matrix that is not invertible is called singular. A square matrix is singular if and only if its determinant is zero.*

Definition 2. *The set of all square matrices which are $n \times n$ array of real numbers is denoted by $\mathcal{M}_n(\mathcal{R})$.*

Definition 3. *Let $\boldsymbol{A} \in \mathcal{M}_n(\mathcal{R})$ be a symmetric matrix. The inertia of $\boldsymbol{A}$ is the ordered triple $(i_+(\boldsymbol{A}), i_-(\boldsymbol{A}), i_0(\boldsymbol{A}))$ where $i_+(\boldsymbol{A})$, $i_-(\boldsymbol{A})$ and $i_0(\boldsymbol{A})$ are the number of positive, negative and zero eigenvalues, respectively. Then, the inertia matrix of $\boldsymbol{A}$ is the diagonal matrix*

$$\boldsymbol{I(A)} = i_+(\boldsymbol{A}) \oplus i_-(\boldsymbol{A}) \oplus i_0(\boldsymbol{A}). \tag{B.1}$$

Definition 4. *Let $\boldsymbol{A}$ and $\boldsymbol{B} \in \mathcal{M}_n(\mathcal{R})$. If there $\exists$ a nonsingular matrix $\boldsymbol{S}$ such that $\boldsymbol{B} = \boldsymbol{SAS^T}$. Then $\boldsymbol{B}$ is said to be T-congruent to $\boldsymbol{A}$.*

Lemma 1. *If $\boldsymbol{A}$ is symmetric, then $\boldsymbol{SAS^T}$ is also symmetric, even if $\boldsymbol{S}$ is singular.*

Theorem 1. *Each symmetric matrix is T-congruent to its inertia matrix.*

Theorem 2. *Symmetric matrices $\boldsymbol{A}$ and $\boldsymbol{B} \in \mathcal{M}_n(\mathcal{R})$ are T-congruent if and only if they have the same inertia.*

Theorem 3. *Let $\boldsymbol{C^{-1}}$ and $\boldsymbol{L^{-1}} \in \mathcal{M}_n(\mathcal{R})$ be symmetric and positive definite matrices. Then there exists a nonsingular matrix $\boldsymbol{P} \in \mathcal{M}_n(\mathcal{R})$ such that*

$$\boldsymbol{L^{-1}} = \boldsymbol{P^T I P} \tag{B.2}$$

and

$$\boldsymbol{C^{-1}} = \boldsymbol{P^{-1}} \boldsymbol{C_{\text{eff}}^{-1}} (\boldsymbol{P^{-1}})^T. \tag{B.3}$$

And the matrix $\boldsymbol{C_{\text{eff}}^{-1}}$ is diagonal with real and positive eigenvalues.

Proof. By assumption $\boldsymbol{L^{-1}}$ is positive definite, i.e. $i_+(\boldsymbol{L^{-1}}) = n$. The identity matrix of the same size, i.e. $\boldsymbol{I} \in \mathcal{M}_n(\mathcal{R})$, has the same inertia. Thus, Theorem 2 ensures that $\boldsymbol{I}$ and $\boldsymbol{L^{-1}}$ are T-congruent. The Definition 4 tells us that there exists a nonsingular matrix $\boldsymbol{T} \in \mathcal{M}_n(\mathcal{R})$ such that $\boldsymbol{I} = \boldsymbol{T^{-1}} \boldsymbol{L^{-1}} (\boldsymbol{T^{-1}})^T$. Lemma 1 guarantees that $\boldsymbol{T^T C^{-1} T}$ is also symmetric and thus diagonalisable by the orthogonal matrix $\boldsymbol{O}$.

Let $\boldsymbol{P^T} = \boldsymbol{TO}$. Then

$$\begin{aligned} (\boldsymbol{P^T})^{-1} \boldsymbol{L^{-1}} \boldsymbol{P^{-1}} &= (\boldsymbol{TO})^{-1} \boldsymbol{L^{-1}} (\boldsymbol{O^T T^T})^{-1} \\ &= \boldsymbol{O^{-1}} \boldsymbol{T^{-1}} \boldsymbol{L^{-1}} (\boldsymbol{T^T})^{-1} (\boldsymbol{O^T})^{-1} \\ &= \boldsymbol{O^{-1}} \boldsymbol{T^{-1}} \boldsymbol{L^{-1}} (\boldsymbol{T^T})^{-1} (\boldsymbol{O^T})^{-1} \\ &= \boldsymbol{O^{-1}} \boldsymbol{I} (\boldsymbol{O^T})^{-1} \\ &= \boldsymbol{I} \end{aligned} \tag{B.4}$$

We recover Eq. (B.2). The matrix $\boldsymbol{O^T} (\boldsymbol{T^T C^{-1} T}) \boldsymbol{O} = \boldsymbol{P C^{-1} P^T} = \boldsymbol{C_{\text{eff}}^{-1}}$ is diagonal. We recover Eq. (B.3). Additionally, Theorem 4 tells us that $\boldsymbol{C^{-1}}$ is T-congruent to $\boldsymbol{C_{\text{eff}}^{-1}}$. We know from Theorem 2 that it implies that they have the same inertia. As $\boldsymbol{C^{-1}}$ is positive definite, so is $\boldsymbol{C_{\text{eff}}^{-1}}$. We conclude that $\boldsymbol{C_{\text{eff}}^{-1}}$ is diagonal positive definite. □

Corollary 3.1. *Let $\boldsymbol{C^{-1}}$ and $\boldsymbol{L^{-1}} \in \mathcal{M}_n(\mathcal{R})$ be symmetric and positive definite matrices. Then $\boldsymbol{C^{-1} L^{-1}}$ is diagonalizable and has real positive eigenvalues.*

Proof. Use Theorem 3 in order to write $\boldsymbol{C^{-1}} = \boldsymbol{P^{-1}} \boldsymbol{C_{\text{eff}}^{-1}} (\boldsymbol{P^{-1}})^T$ and $\boldsymbol{L^{-1}} = \boldsymbol{P^T I P}$. Then

$$\boldsymbol{C^{-1} L^{-1}} = \boldsymbol{P^{-1}} \boldsymbol{C_{\text{eff}}^{-1}} (\boldsymbol{P^{-1}})^T \boldsymbol{P^T P} = \boldsymbol{P^{-1}} \boldsymbol{C_{\text{eff}}^{-1}} \boldsymbol{P}. \tag{B.5}$$

We can conclude as $\boldsymbol{C_{\text{eff}}^{-1}}$ is a diagonal matrix with real and positive eigenvalues. □

We now confirm that $\boldsymbol{C_{\text{eff}}^{-1}} = \boldsymbol{\omega^2}$. We take the definition of the the matrix $\boldsymbol{\omega^2}$ in Eq. (2.32) and insert Eq. (B.5). This gives:

$$\begin{aligned} \boldsymbol{\omega^2} = \boldsymbol{P C^{-1} L^{-1} P^{-1}} &= \boldsymbol{P} (\boldsymbol{P^{-1}} \boldsymbol{C_{\text{eff}}^{-1}} (\boldsymbol{P^{-1}})^T) (\boldsymbol{P^T P}) \boldsymbol{P^{-1}} \\ &= \boldsymbol{C_{\text{eff}}^{-1}} (\boldsymbol{P^{-1}})^T \boldsymbol{P^T} = \boldsymbol{C_{\text{eff}}^{-1}}. \end{aligned} \tag{B.6}$$

We notice that with the specific choice of $\boldsymbol{P}$ such that $(\boldsymbol{P}^T)^{-1}\boldsymbol{L}^{-1}\boldsymbol{P}^{-1} = \boldsymbol{I}$, the inductances of the normal modes all worth one. We could have chosen any diagonal and positive definite matrix $Ł_{\text{eff}}^{-1}$, instead of $\boldsymbol{I}$, as such a matrix is T-congruent to $\boldsymbol{L}^{-1}$. The demonstrations above would still hold. In this way, we can impose the effective inductances of the normal modes, i.e. the eigenvalues of $Ł_{\text{eff}}$.

Appendix C

This appendix draws a connection between a N-port network and its equivalent Foster circuit. It summarizes my understanding of existing literature ([25], [40] and [41]) and are based on a derivation by Ciani [27].

N-port network

We consider a generic microwave network with N ports connected to the outside world as depicted in Fig C.1. Arbitrary systems can be attached at the ports, for example a Josephson junction (taking only the non-linear part), a voltage drive or any type of transmission line [25]. In Laplace domain, the impedance matrix of the microwave network, $\boldsymbol{Z}(s)$, relates voltages and currents at the ports as

$$\boldsymbol{V}(s) = \boldsymbol{Z}(s)\boldsymbol{I}(s), \tag{C.1}$$

Here s is a complex variable. A linear network is fully characterized by its impedance matrix $\boldsymbol{Z}(s)$ [25]. Therefore, a microwave structure can be regarded as a 'black-box' which absorbs all the details of the structure and which is fully characterized by $\boldsymbol{Z}(s)$. The coefficients $Z_{ij}(s)$ can be obtained by driving port j with the current I_j while open-circuiting all other ports, i.e. $I_k = 0$ for $k \neq j$, and measuring the open-circuit voltage at port i. As defined in [25], $Z_{ij}(s)$ is the input impedance seen looking into port i when all other ports are open-circuited as well as the transfer impedance between ports i and j when all other ports are open-circuited.

$$Z_{ij}(s) = \left.\frac{V_i(s)}{I_j(s)}\right|_{I_k=0 \text{ for k}\neq\text{j}} \tag{C.2}$$

The elements of $\boldsymbol{Z}(s)$ are in general complex. We now introduce the following network properties :

- A network is *linear* if given an input $\boldsymbol{x}(t) = c_1\boldsymbol{x_1}(t) + c_2\boldsymbol{x_2}(t)$ where t generally denotes time, with $c_{1,2} \in \mathbb{R}$ the output is $\boldsymbol{w}(t) = c_1\boldsymbol{w_1}(t) + c_2\boldsymbol{w_2}(t)$ where $\boldsymbol{w_{1,2}}(t)$

is the output associated with $\boldsymbol{x_{1,2}}(t)$. The same holds in Laplace domain. Circuits elements like capacitances, inductances and resistances are characterized by a voltage-current linear relation and thus a network composed of these elements is linear.

- A network is *reciprocal* if its impedance (scattering) matrix is symmetric [25].
- A network is *lossless* if it does not contain any elements which dissipate energy. Dissipative elements are characterized by a non-zero real part of their impedance, $\mathrm{Re}(Z) \neq 0$, like resistances for example.

In the case of a lossless network, $Z_{ij}(s)$ are purely imaginary [25]. We point out that the impedance matrix of a lossless and non-reciprocal network is symmetric and purely imaginary and that a network including capacitances and inductances but no resistances, is linear, reciprocal and lossless.

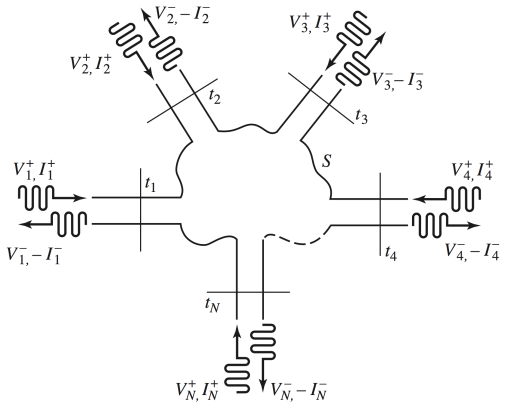

Figure C.1: An arbitrary N-port microwave network. Here t_n is the terminal plane at port n. (V_n^+, I_n^+) and (V_n^-, I_n^-) denote the equivalent voltages and currents at port n for the incident and reflected waves, respectively. (The figure is taken from [25], page 174.).

Equivalent Foster circuit

It has been demonstrated by Cauer and Belevitch that a linear, reciprocal, lossless N-port network can be represented by an equivalent circuit called the Foster circuit [40]. These networks are equivalent in the sense that they have the same impedance matrix up to a scaling factor. Therefore the equivalent Foster circuit is not unique [41]. In our context, we are interested in drawing the connection between a linear, reciprocal

and lossless N-port network and the corresponding Foster impedance representation, in which the circuit is represented with series of parallel LC oscillators. We show an example in Fig. C.2 for the one-port case. Drawing this connection is useful because the Foster circuit provides an expression for $\boldsymbol{Z}(s)$ that we derive in Sec. 5.

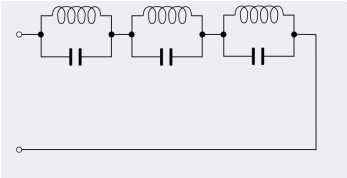

Figure C.2: Foster circuit. This network has one port shown on the left and can be represented with three LC oscillators. Picture courtesy of Spinningspark at Wikipedia.

We now explain what the Foster circuit of a N-port network is. A Foster circuit connects the currents and voltages at the ports, I_{Pn} and V_{Pn}, with those of the network eigenmodes (drawn as LC-oscillators), $I_{LC,k}$ and $V_{LC,k}$ via ideal transformer relations. Fig. C.3a shows a Foster circuit with the N port fluxes, $\boldsymbol{\Phi_{Pn}}$, on the left and the $M = N + N_I$ eigenmodes fluxes, $\boldsymbol{\Phi_{LC,k}}$ on the right, where N_I denotes the internal degrees of freedom of the linear network. We introduce the voltage drop across the transformer k of port n as V_{Pn}^k. An ideal transformer with current flow convention is represented in Fig. C.3b. It follows that :

$$V_{Pn} = \sum_{k=1}^{M} V_{Pn}^k \tag{C.3}$$

We introduce further I_{Pn} as the current at port n, flowing through the ideal transformers. Since an ideal transformer preserves the instantaneous power, i.e., $V_{Pn}^k(t) I_{Pn}(t) = V_{LC,k}(t) I_{LC,k}(t)$, if the turns ratio of the transformer is t_{nk}, then $V_{Pn}^k(t) = t_{nk} V_{LC,k}(t) \implies I_{Pn}(t) = t_{nk} I_{LC,k}(t)$. And the same holds in Laplace domain. We have :

$$\frac{I_{LC,k}}{I_{Pn}} = \frac{V_{Pn}^k}{V_{LC,k}} = t_{nk} \tag{C.4}$$

We can use Eq. (C.4), the flux definition in Eq. (2.26) and integrate Eq. (C.3). This leads to the following expression: :

$$\Phi_{Pn} = \sum_{k=1}^{M} t_{nk} \Phi_{LC,k} \tag{C.5}$$

Connection with the eigenmode approach

The circuits analyzed in section 2.2 are subdivided into a linear network, made out of capacitances and inductances, and N non-linear inductive elements, i.e. the Josephson junctions spiders, attached at the ports. Therefore the N-port network is linear, reciprocal and lossless and an equivalent Foster representation can be derived for it. We now draw the connection between the eigenmode approach presented in Sec. 2.2 and the first Foster representation. On one side, in the eigenmode approach, the port fluxes defined across the Josephson junctions are expressed as a linear combination of the eigenmodes, see Eq. (2.50). While on the other side, Eq. (C.5) gives the relation between the port and the normal modes (LC-oscillators) fluxes originating from the Foster representation. Comparing Eqs. (2.50) with (C.5), we identify the turn ratio as the coefficient matrix $(\mathbf{P}^{-1})_{nk}$ multiplied by a scaling factor :

$$t_{nk} = (\mathbf{P}^{-1})_{nk}\sqrt{\frac{C}{C_{k,\text{eff}}}}, \quad n = 1, \ldots, N, \quad k = 1, \ldots, M. \tag{C.6}$$

making clear the connection between the eigenmode approach and the Foster representation.

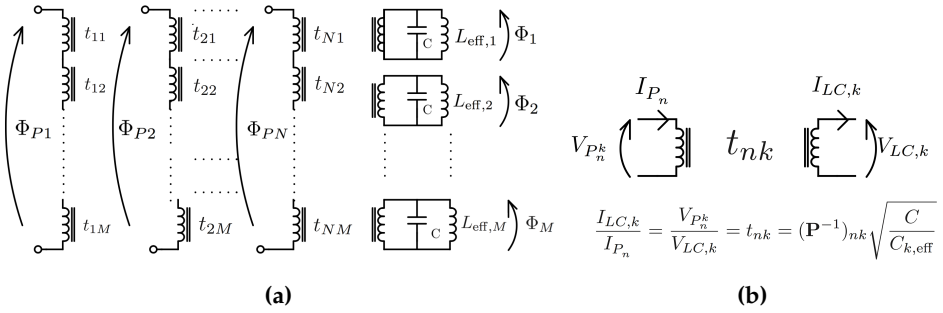

Figure C.3: a) Equivalent Foster circuit of an arbitrary lossless, reciprocal linear network. Foster circuits relate the port and the oscillators (eigenmode) voltages and currents, in an intuitive manner via ideal transformer relations given on Fig. **b)**. The turn ratio t_{nk} are to be identified with $(\mathbf{P}^{-1})_{nk}\sqrt{\frac{C}{C_{k,\text{eff}}}}$.

Electrical impedances

In this subsection a brief introduction to passive lumped element impedance in the Laplace domain is carried out as these expressions are needed later in Sec. 5. The impedances in the Laplace domain for the lumped passive elements can be obtained by

applying the Laplace transform on the characteristic equation relating the voltage to the current across the element. In effect, the impedance of a capacitor, characterized by C, is obtained by applying the Laplace equation on $C\frac{dV(t)}{dt} = i(t)$. As $L(\frac{dV(t)}{dt}) = sL(V(t))$, the relation becomes $CsV(s) = I(s)$ in the Laplace domain. Thus, the impedance of a capacitor is

$$Z_c(s) = \frac{1}{Cs} \tag{C.7}$$

Proceeding similarly for an inductance element characterized by L, for which it holds that $L\frac{di(t)}{dt} = V(t)$, we obtain its impedance as

$$Z_L(s) = Ls \tag{C.8}$$

The impedance of a parallel LC-oscillator is immediately obtained via the rule of adding impedance in parallel:

$$Z_{LC} = \frac{1}{\frac{1}{Z_c} + \frac{1}{Z_L}} \tag{C.9}$$

which gives

$$Z_{LC}(s) = \frac{1}{Cs}\frac{s^2}{s^2 + \omega_{LC}^2} \tag{C.10}$$

where $\omega_{LC} = 1/\sqrt{LC}$.

Derivation of the partial fraction expansion of the impedance matrix

We will now show that this implies that the impedance matrix of a N-port network in Laplace domain can always be expanded as a sum of LC-oscillators [40]

$$\boldsymbol{Z}(s) = \sum_{k=1}^{M} \frac{1}{Cs}\frac{s^2}{s^2 + \omega_k^2}\boldsymbol{A}_k, \tag{C.11}$$

where $\boldsymbol{A}_k$ are $N \times N$ rank-1 matrices connected to the turns ratios in Fig. C.3a by the relation

$$\boldsymbol{A}_k = \boldsymbol{t}_k\boldsymbol{t}_k^T, \tag{C.12}$$

with

$$\boldsymbol{t}_k = \begin{pmatrix} t_{1k} & t_{2k} & \dots & t_{Nk} \end{pmatrix}^T. \tag{C.13}$$

Note that the Foster impedance representation described in Subsec. 5 provides the expression in Eq. (C.11), see Eq. (9) in [40]. Now the idea is to start from Eq. (C.1) and to find a way to inject the definition of the impedance of the LC oscillators in parallel

given in Eq. (C.10). First, let us suppose to impose a generic vector of currents to the ports

$$\boldsymbol{I}(s) = \begin{bmatrix} I_1(s) & I_2(s) & \dots & I_N(s) \end{bmatrix}^T. \tag{C.14}$$

Considering the circuit in Fig. C.3a and using the ideal transformer relation in C.4, then the total current passing through the k-th oscillator is given by

$$I_{LC,k}(s) = \sum_{m=1}^{N} t_{m,k} I_m(s) = \boldsymbol{t}_k^T \boldsymbol{I}(s). \tag{C.15}$$

As a consequence we get the following voltage across the k-th oscillator

$$V_{LC,k}(s) = Z_{LC,k}(s) I_{LC,k}(s) = \frac{1}{Cs} \frac{s^2}{s^2 + \omega_k^2} \boldsymbol{t}_k^T \boldsymbol{I}(s). \tag{C.16}$$

The voltage drop across the n-th port can now immediately be expressed as :

$$V_n(s) = \sum_{k=1}^{M} t_{nk} V_{LC,k}(s) = \sum_{k=1}^{M} \frac{1}{Cs} \frac{s^2}{s^2 + \omega_k^2} t_{nk} \boldsymbol{t}_k^T \boldsymbol{I}(s), \tag{C.17}$$

and so write the vector of port voltages as

$$\boldsymbol{V}(s) = \underbrace{\left(\sum_{k=1}^{M} \frac{1}{Cs} \frac{s^2}{s^2 + \omega_k^2} \boldsymbol{t}_k \boldsymbol{t}_k^T \right)}_{\boldsymbol{Z}(s)} \boldsymbol{I}(s), \tag{C.18}$$

thus from Eq. (C.1) and using the definition Eq. (C.12) we finally obtain the expansion of $\boldsymbol{Z}(s)$ in Eq. (C.11).

Applying the method in practice

We can envision in general two situations in which we would like to use the previous results. First of all, the easiest case is the one in which we have already a lumped element representation of the circuit. In this case, following the derivation in Sec. 2.2, we can just find the normal modes and then express the fluxes across the ports as a linear combination of them via Eq. (2.50). However, we can also consider the situation in which we do not have explicitly a representation of the network, but we have its impedance matrix. How do we get the circuit representation shown in Fig. with C.3a? Suppose that we found the poles of the impedance matrix ω_k. In order to be able to find the parameters of the circuit in Fig. C.3a, we need C and $\boldsymbol{A}_k$. However, as it is clear from the impedance expansion Eq. (C.11) what matters is only the ratio $\boldsymbol{A}_k/C$ which is

the reason why we can take C to be arbitrary. We notice that the matrices $\boldsymbol{A}_k/C$ have the interpretation of residue matrices. In fact, assuming non-degenerate modes,

$$\text{Res}(\boldsymbol{Z}(s); i\omega_k) = \lim_{s\to\omega_k}(s - i\omega_k)\boldsymbol{Z}(s) = \lim_{s\to\omega_k}\frac{(s - i\omega_k)}{Cs}\frac{s^2}{s^2+\omega_k^2}\boldsymbol{A}_k = \frac{\boldsymbol{A}_k}{2C}. \tag{C.19}$$

Fixing C arbitrarily thus gives us $\boldsymbol{A}_k$ from which one can obtain the vector of turns ratios $\boldsymbol{t}_k$ such that $\boldsymbol{A}_k = \boldsymbol{t}_k\boldsymbol{t}_k^T$. In this way, we can obtain the parameters of the Foster representation in Fig. C.3a.